Potential Vorticity Inversion Diagnosis of

the Development of Polar Lows

by

Longtao Wu

A dissertation submitted in partial fulfillment of

the requirements for the degree of

Doctor of Philosophy

(Atmospheric and Oceanic Sciences)

at the

UNIVERSITY OF WISCONSIN – MADISON

2010

UMI Number: 3424083

A dissertation entitled

Potential Vorticity Inversion Diagnosis of the Development of
Polar Lows

submitted to the Graduate School of the
University of Wisconsin-Madison
in partial fulfillment of the requirements for the
degree of Doctor of Philosophy
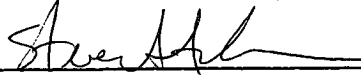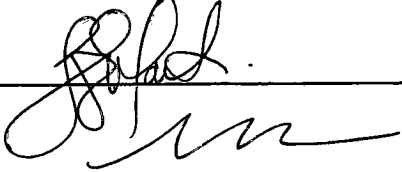
by

Longtao Wu

Date of Final Oral Examination: 12/22/2009

Month & Year Degree to be awarded: **December**   **May** 2010   **August**

****

Approval Signatures of Dissertation Committee

Signature, Dean of Graduate School

Abstract

The objectives of this dissertation are to: 1) identify the bulk microphysics scheme (BMS) that is likely to be most suitable for model-based investigations of the role of moist processes in the dynamics of polar low development; 2) examine the relative influences of upper-tropospheric, lower-tropospheric, and diabatic potential vorticity (PV) anomalies in the development of polar lows.

Four polar lows, two over the Sea of Japan and two over the Nordic Sea, were simulated with the Weather Research and Forecasting (WRF) model. Five mixed-phase BMSs were evaluated in numerical simulations of polar lows. The simulations were validated against the satellite observed cloud top temperatures and precipitation and against gauge-calibrated surface radar precipitation estimates around Japan. Although definitive validation is not possible with the available data, results from the WRF Single-Moment 6-class (WSM6) scheme appeared to reproduce cloud and precipitation processes most realistically. The model produced precipitation intensities comparable to validation products over the Sea of Japan. However, in the Nordic Sea cases, all five schemes produced significantly more precipitation than the satellite microwave estimates, even though the latter estimates are known to average slightly high in the same region when validated against monthly totals measured at Jan Mayen Island.

The piecewise PV inversion method developed by Davis and Emanuel (1991) is used to diagnose the development processes of two polar lows, one over the Sea of

Japan in December 2003 and the other over the Nordic Sea in January 2003. It was shown that the main synoptic development of polar lows was successfully captured using the inversion method. Both of the polar lows were initiated when the positive PV anomaly near the tropopause approached the surface positive temperature anomaly. Further intensification of polar lows was contributed by the latent heat release in association with cloud and precipitation processes. For the case over the Sea of Japan, the rapid height falls at lower troposphere were primarily contributed by the upper tropospheric PV anomaly. However, the development of the polar low over the Nordic Sea was mainly a result of the boundary temperature anomaly contributed by the strong air-sea interaction over the warm sea surface.

Comparing between the two polar low cases, it was suggested that the upper-tropospheric PV anomaly is a necessary condition to support the further development of polar lows. The shorter lifecycle of the case over the Nordic Sea may be an artifact of the upper-tropospheric PV anomalies inability to support its further development. Furthermore, the intense air-sea interaction which led to the boundary temperature anomaly was more important for the polar low case over the Nordic Sea while its effect was smaller in the case over the Sea of Japan.

Acknowledgements

My deepest gratitude is to my advisor Prof. Grant W. Petty for the opportunity to work with him on this study. It's been my greatest fortune to have an advisor like him, who gave me so much support, help, guidance and freedom. I am deeply grateful to my committee Dr. Jonathan E. Martin for his invaluable guidance, for many enlightening discussions and for help on preparing the manuscript. His time and patience are greatly appreciated. I am grateful to the remainder of my committee members: Dr. Steven A. Ackerman, Dr. Ralf Bennartz, Dr. Kam-Wah Tsui and Dr. John A. Young. I cannot thank them enough for their time, kindness and advices. Thanks to Mr. Pete Pokrandt, Mr. Yunfei Zhang and the WRF support staff for their assistance with setting up the WRF simulations. I would like to thank to Dr. Gunnar Noer and Dr. Wataru Yanase for sharing their compilation of polar low cases. I also thank Dr. Derek Posselt and Mr. Jason Otkin for assistance with the PV inversion programs. Additional thanks to Dr. Petty's group, including Dr. Wei Huang, Dr. Benjamin Johnson, Dierk Polzin and Sarah Davis for their help and support. I want to thank Connie Linehan, Maria Vasys, Don Moskowitz, and Angel Skram for their support during the past years.

Special thanks to Dr. Yinghui Liu and Dr. Zhenglong Li. They both provided tremendous help, support and encouragement to me since I arrived here. I want to thank my Chinese fellows in AOS building for the happy memories, including Dr. Xuanji Wang, Dr. Yafang Zhong, Wei Zhou, Chian-Yi Liu, Dr. Li Bi, Fang Wang,

Chunhua Yao, Dr. Jun Li, Dr. Jinlong Li, Dr. Guangshang Chen, Dr. Jun Huang, Dr. Xin Jin, Hong Zhang, Agnes Huei Ni, Feng He, Wei Liu, Yun Liu, Dr. Na Wen, Jun Cheng, Dr. Shu Wu, and Fuyao Wang.

I would like to especially acknowledge my wife, Xiuying Chen, for her selfless supports, sacrifice and endless love. Her encouragement and supports always give me confidence. Finally, I would like to express my sincere gratitude to my parents for their patience and understanding during the periods of my absence.

Table of Contents

List of Figures

List of Tables

Chapter 1   Background and Motivation

1.1   Introduction

A polar low is characterized as an intense mesoscale cyclone which often develops over high latitude oceans (generally during the cold season) in the cold air streams of the polar air mass. Rasmussen and Turner (2003) define a polar low as a *"small, but fairly intense maritime cyclone that forms poleward of the main baroclinic zone (the polar front or other major baroclinic zone). The horizontal scale of the polar low is approximately between 200 and 1000 kilometers and surface winds near or above gale for*ce". The entire lifecycles of polar lows may vary from several hours to several days. These storms are most often manifest in comma and spiraliform cloud patterns shown on satellite imagery. A warm core is often formed in the center of a polar low, and sometimes a clear eye similar to that associated with tropical cyclones can be observed. As polar lows are often accompanied by strong wind and heavy snowfall, they represent a significant potential hazard to marine traffic and operations. Because of their short lifecycles, small sizes, and the fact that they occur primarily over open ocean, they have also been notoriously difficult to study in detail using conventional surface data.

As part of the Arctic Cyclone Expedition, a polar low was first observed by aircraft on 27 February, 1984 (Shapiro et al., 1987). A very complete description of the polar low with respect to its momentum, thermal, moisture and precipitation

characteristics was obtained. Several other polar lows were investigated by aircraft in the following years (Douglas et al., 1991; Bond and Shapiro, 1991; Douglas et al., 1995). However, such observations are still relatively rare.

1.1.1 Satellite observations

Since the first meteorological satellite was launched in 1960, satellite data have become one of the most important tools for the research and monitoring of polar lows. High resolution infrared and visible imagery from polar-orbiting satellites can provide a great deal of information about cloud structure and locations of these storms. Cloud height, cloud top temperature and wind direction can also be inferred. Microwave (MW) sounding data, such as those available using the Microwave Sounding Unit (MSU) and the Advanced Microwave Sounding Unit (AMSU), can provide vertical profiles of temperature and moisture. Indeed, such data have been used to identify the warm cores of polar lows (Forsythe et al., 1996; Moore and Vonder Haar, 2003). A problem arises, however in that the spatial resolutions of MW sounders are relatively coarse when compared to the scales of polar lows.

Scatterometers, such as SeaWind onboard QuikSCAT, can provide both surface wind speed and wind direction. The distinct surface circulation signature can be identified with scatterometer winds. Passive MW radiometers, such as the Special Sensor Microwave/Imager (SSM/I) and the Advanced Microwave Scanning Radiometer - Earth Observing System (AMSR-E), allow estimation of integrated

cloud water vapor content (WV) across the system, liquid water content in the cloudy regions and instantaneous precipitation rate. Because ice particles demonstrate strong scattering at 85 GHz, precipitation sized ice-scattering signal (S) helps to determine whether polar lows are convective or not (Claud et al., 1993; Carlton and Song, 2000). With the unprecedented availability of high-resolution satellite infrared and passive microwave observations of surface wind, precipitation, and other variables over the past decade, it is now feasible to directly observe the evolution and structure of polar lows and to assess the realism of model simulations of these storms.

1.1.2 Numerical studies

While most of the early research into polar lows consisted of observational studies, attempts were made after the 1980s to represent these lows in numerical models. For a long time, the resolution of the numerical models was too coarse to describe polar lows. There was a breakthrough during the polar low project organized by the Norwegian Meteorological Institute (DNMI) in 1983-85. As part of the project, the Norwegian Limited Area Model (NORLAM) was developed, which gave the first realistic simulations of polar lows (Grønås, 1987; Nordeng, 1987; Nordeng, 1990; Nordeng and Rasmussen, 1992).

With the further development of operational numerical weather prediction (NWP) systems, a number of polar lows over different regions were simulated with different NWP models, such as the High Resolution Limited Area Model (HIRLAM),

the PSU/NCAR mesoscale model (known as MM5), as well as the Regional Atmospheric Modeling System (RAMS) (Bresch et al., 1997; Nielsen, 1997; Martin and Moore, 2005; Guo et al., 2007). The development and maintenance mechanism of polar lows were studied. It has been shown that polar lows are triggered by an upper-level potential vorticity (PV) anomaly approaching a low-level baroclinic zone. The polar lows develop under a combination of baroclinic and convective processes. Latent heat release (LHR) in the convective process is a crucial element in case of strong development. A number of sensitivity studies using numerical models have shown that high resolution, accurate sea surface temperature (SST) and ice margin analyses, as well as appropriate convective and PBL parameterization schemes are important in the forecasting of polar lows (Bresch et al., 1997; Nielsen, 1997; Yanase et al., 2002; Martin and Moore, 2005).

Over the past two decades, a number of polar lows over different regions have been simulated with different numerical models. Sensitivity studies have shown that LHR in the convection process is crucial to promoting sufficient strong development of polar lows (Bresch et al., 1997; Nielsen, 1997; Yanase et al., 2002; Martin and Moore, 2005; Guo et al., 2007). Thus, a realistic treatment of cloud and precipitation processes is important for numerical simulation of polar lows.

1.2   Bulk microphysics schemes

A number of bulk microphysics schemes (BMS) have been developed to

explicitly resolve water vapor, cloud and precipitation processes in numerical simulations (Kessler, 1969; Lin et al., 1983; Rutledge and Hobbes, 1983; Ziegler, 1985; Meyers et al., 1997; Reisner et al., 1998). The BMS can be classified by two different methods; one is a single-moment approach and the other a multiple-moments approach. The single-moment BMS predicts only the mixing ratios of the hydrometeors by representing the hydrometeor size for each class with a distribution function, such as an exponential or a gamma type function (Kessler, 1969; Lin et al., 1983; Rutledge and Hobbes, 1983; Ziegler, 1985). Meanwhile, the double-moment BMS predicts not only the mixing ratio of the hydrometeors but also their number concentrations (Meyers et al., 1997; Reisner et al., 1998).

To evaluate the results of different BMSs, some studies have been done on the simulations of different weather systems (Morrison and Pinto, 2006; Gallus and Pfeifer, 2008; Bromwich et al., 2009). For springtime Arctic mixed-phase stratiform clouds, a complex scheme was found to be better at reproducing the observed persistence and horizontal extent of the mixed-phase stratus deck (Morrison and Pinto, 2006). In a German squall line simulation, Gallus and Pfeifer (2008) evaluated the performance of the Purdue (Chen and Sun, 2002), Older Thompson (Thompson et al., 2004), New Thompson et al. (2008), WRF Single-Moment 6-class (WSM6; Hong and Lim, 2006) and WRF Single-Moment 5-class (WSM5; Hong et al., 2004) provided with the Weather Research and Forecasting (WRF) model Version 2.1.2. It was found that all the five BMSs overestimate radar reflectivity in the domain, particularly in the stratiform region of the convective system. Too much graupel was produced in the

schemes that included graupel as a hydrometeor. During the development of the polar-WRF (based on the WRF Version 2.2) at Byrd Polar Research Center, it was shown that the sensitivity of the WSM5, Older Thompson and Morrison 2-moment schemes (Morrison et al., 2005) was small over the western Arctic domain (Bromwich et al., 2009). However, the performance of various BMSs in representing polar low development has never been evaluated probably due to lack of validation data. One of the primary objectives of this dissertation is therefore to undertake such a comparison with available observational data.

1.3 Development mechanism of polar lows

In the early days of polar low research, considerable debate existed concerning whether polar lows were purely baroclinic systems (Harrold and Browning, 1969; Mansfield, 1974) or were dominated by deep convection (Rasmussen, 1979; Emanuel and Rotunno, 1989). Harrold and Browning (1969) proposed that polar lows formed as a result of baroclinicity instability, which is related to the horizontal temperature gradient and the thermal wind. Potential energy associated with the mean horizontal temperature gradient was converted into kinetic energy by the ascent of warm air and the descent of cold air during the development of a baroclinic system. Rasmussen (1979) suggested that LHR in the convective process was important for the polar low development through the mechanism known as conditional instability of the second kind (CISK). In the CISK mechanism, an initial disturbance initiates the low-level

convergence that forces the cumulus convection. LHR associated with the cumulus convection in turn provides energy to force further low-level convergence. The low-level convergence supplies continuous moisture for further LHR and thus a positive feedback is working in the system (Espy, 1841).

The model results of Sardie and Warner (1983, 1985) showed that both moist baroclinic instability and CISK were responsible for the development of polar lows. However, the relative importance of these two processes varied with different synoptic conditions. Moist baroclinic instability was thought to mainly account for the formation of polar lows in the Pacific while such storms enjoyed a much smaller contribution from CISK. However, the development of polar lows in the North Atlantic was thought to be dominated by CISK.

An alternative convective theory, the wind-induced surface heat exchange (WISHE) theory, has also been invoked to explain the intensification of convective polar lows (Emanuel and Rotunno, 1989). Strong surfaces winds near the center of the cyclones increases surface sensible and latent heat fluxes which lead to the low-level inflow towards the center of an incipient polar low. Turbulent heat transfer and convection transfer surface sensible and latent heat upward.

Now it is widely accepted that baroclinic conversion and deep convection are the two primary energetic mechanisms driving polar low formation (Rasmussen and Turner 2003). Since the 1990s, observational case studies and numerical simulations of polar lows (Rasmussen et al., 1992; Nordeng and Rasmussen, 1992; Grønås and Kvamstø, 1995; Guo et al., 2007) suggest that the development of polar lows, though

usually initiated by upper-level potential vorticity (PV) anomalies interacting with strong surface baroclinicity, is greatly enhanced by the presence of deep moist convection and strong fluxes of latent and sensible heat from the ocean (Grønås and Kvamstø, 1995; Bresch et, 1997; Yanase et al., 2004; Guo et al., 2007). Montgomery and Farrell (1992) proposed a two stage development model. In the first stage, the combined effect of an upper-level PV anomaly and a low-level baroclinic zone induces a self-development process in which rapid low-level spinup and generation of low- and midlevel PV anomalies augment the baroclinic interaction between these systems. In the second stage, the latent heating associated with the development of clouds and precipitation intensifies the polar low development by enhancing the upward motion. This model suggests that polar low development is broadly similar to mid-latitude cyclonic development, with moist processes playing a more substantial role in the intensification of polar lows.

Recent work has suggested that the relative importance of different forcing mechanisms can change significantly during the lifecycles of polar lows. A 'spectrum' of polar lows including both pure baroclinic and pure 'convective' systems may, in fact, exist (Rasmussen and Turner, 2003).

Despite the progress made, there are still many uncertainties associated with the development mechanisms of polar lows due to their complexity and the difficulty involved in observing them. The second major objective of this dissertation is to apply PV analysis to numerical simulations of polar lows. The purpose is to investigate the effect of discrete PV anomalies on the development of polar lows.

1.4 Potential vorticity inversion

In the real atmosphere, the relative importance of the various developmental processes varies from case to case and changes during the lifecycle. In order to develop a complete understanding of the dynamics of a polar low, the relative importance of each process must be discerned. Sensitivity studies, in which certain physical processes are switched on or off in a suite of numerical model simulations, have commonly been used to investigate the importance of various processes on polar low development (e.g. Bresch et al., 1997; Yanase et al., 2004; Guo et al., 2007). Since the effect of one physical process is often coupled to the others, artificial removal of one can affect the model atmosphere in unanticipated ways. This non-linearity of physical interactions imposes an inherent limitation on the insights gained by such sensitivity studies.

An alternative method by which to investigate the relative importance of various physical processes on the development of polar lows involves piecewise PV inversion. Two properties of PV, *conservation* and *invertibility*, make it a useful diagnostic quantity for the study of nearly balanced atmospheric flows. In adiabatic, inviscid flow, PV is conserved under the full primitive equations for the complete atmospheric system. The invertibility principle states that given a distribution of PV, a balance condition relating the mass and momentum fields, and boundary conditions on the analysis domain, there is only one set of balanced wind and temperature fields

associated with a particular PV distribution. Additional insights into cyclone dynamics can be obtained by considering the *nonconservation* of PV (Stoelinga, 1996) which states that their PV distribution can be changed as a result of diabatic heating and friction.

The nonlinear piecewise PV inversion method developed by Davis and Emanuel (1991, hereafter DE) allows recovery of the subset of the wind and temperature fields attributable to a discrete PV anomaly. Thus, the effect of a discrete PV anomaly during the development of a weather system can be clearly revealed from the piecewise PV inversion results. Accordingly, the relative importance of discrete PV anomalies on the development of a given weather system can also be deduced. The DE method has been primarily used to understand the nature of extratropical cyclones and the role of LHR in cyclone evolution (e.g. Davis and Emanuel, 1991; Davis et al., 1993; Stoelinga, 1996; Korner and Martin, 2000; Martin and Marsili, 2002; Martin and Otkin, 2004; Posselt and Martin, 2004).

Although some fraction of the total circulation associated with a polar low is likely unbalanced flow, Rasmussen and Turner (2003) suggested that considerable insight into the dynamical nature of these storms can be obtained by considering their 'balanced dynamics'. Bracegirdle and Gray (2009) implemented the piecewise PV inversion method to assess the relative importance of different PV anomalies and their interaction during a polar low over Norwegian Sea on October 13 1993. It was shown that the polar low was initiated by a positive upper-level PV anomaly. After that, the intensification of the polar low was dominated by the lower-troposphere PV anomaly

associated with LHR. Their analysis revealed that a third stage of development, dominated by WISHE, might be a reasonable addition to the two stage development of polar lows proposed by Montgomery and Farrell (1992).

1.5   Research objective

Lack of data has always been the major problem for polar low studies in the high latitude regions. The new high resolution numerical models with good parameterizations of physical processes have proved to be very effective for simulating the structure and development of mesoscale systems, such as polar lows in data sparse regions. With the unprecedented availability over the past decade of high-resolution satellite infrared and passive microwave observations of surface wind, precipitation, and other variables, it is now feasible to directly observe the evolution and structure of polar lows and to assess the realism of model simulations of these storms. New insights into polar low development can be obtained from such a combined observational/modeling approach. The objective of this research is to investigate the development of polar lows with a combination of in-situ, radar, satellite and model data.

Studies have shown that cloud and precipitation processes are important for the development of polar lows. Thus, BMS are an important part of numerical models in order to successfully predict the development and structure of polar lows. Although a number of BMSs have been developed to explicitly resolve water vapor, cloud and

precipitation processes in numerical simulations, how well they represent the development of polar lows has not yet been evaluated. In this study, the performance of five mixed-phase BMSs provided with the WRF model is evaluated based on the observational datasets. The purpose was to identify the BMS that is likely to be most suitable for subsequent model-based investigations of the role of moist processes in the dynamics of polar low development.

After the performance of different BMSs on the simulations of polar lows is evaluated, the model outputs are used to investigate the development process of polar lows. For a complete understanding of the dynamics of a polar low, the relative importance of various forcing processes during the development of the polar low should be discerned. The piecewise PV inversion method developed by Davis and Emanuel (1991) has proven quite valuable in developing understanding of the nature of extratropical cyclones. In this study, the outputs from the numerical simulations are used to perform a piecewise PV inversion in order to examine the relative influences of upper-tropospheric, lower-tropospheric, and diabatic PV anomalies in the development of polar lows.

Chapter 2 Datasets

Four polar lows, two over the Sea of Japan and two over the Nordic Sea, are simulated in this study. All selected polar lows are spiraliform in shape. One representative Moderate Resolution Imaging Spectroradiometer (MODIS; Baum and Platnick, 2006) image for each case is shown in Fig. 1. A summary of other key properties is listed in Table 1. All the four cases are used in the intercomparsion section to evaluate the performance of different BMSs. The development processes of two cases, one case over the Sea of Japan in December 2003 and one case over the Nordic Sea in January 2003, are investigated with the PV inversion method. Since all these cases have quite similar results in the intercomparison of BMSs, only the synoptic conditions of the two cases used in the PV inversion section are discussed in next chapter in detail.

Table 1 The observation times and locations of the polar low cases. JP represents the cases over the Sea of Japan. ND represents the cases over the Nordic Sea. T1 means the first observation time. T2 is the second observation time. All the times are UTC.

Case	T1	Location	T2	Location
JP1	19 Dec 2003 1645	$41.0\,^{\circ}$N, $139.0\,^{\circ}$E	20 Dec 2003 0350	$39.0\,^{\circ}$N, $140.0\,^{\circ}$E
JP2	04 Dec 2005 1710	$39.5\,^{\circ}$N, $137.0\,^{\circ}$E	05 Dec 2005 0415	$38.5\,^{\circ}$N, $136.5\,^{\circ}$E
ND1	17 Jan 2003 0145	$70.0\,^{\circ}$N, $6.0\,^{\circ}$E	17 Jan 2003 0325	$70.0\,^{\circ}$N, $6.0\,^{\circ}$E
ND2	05 Dec 2005 0940	$73.0\,^{\circ}$N, $14.0\,^{\circ}$E	05 Dec. 2003 1120	$72.5\,^{\circ}$N, $14.0\,^{\circ}$E
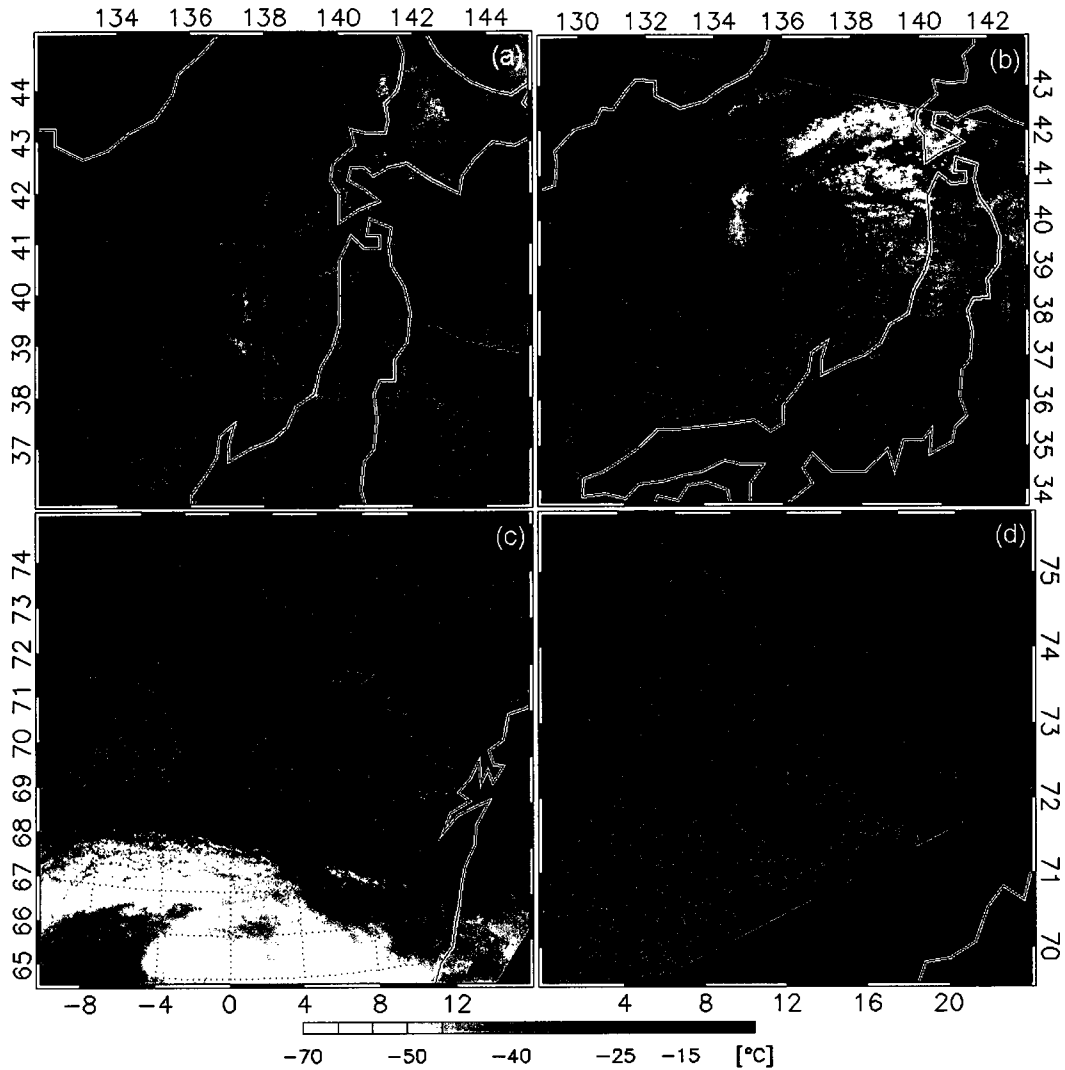
FIG. 1 MODIS cloud-top temperature (CTT; channel 32) observed for the four polar low cases considered in this study. See Table 1 for case abbreviations. (a) JP1, 20 Dec 2003 0350 UTC. (b) JP2, 04 Dec 2005 1710 UTC. (c) ND1, 17 Jan 2003 0325 UTC. (d) ND2, 05 Dec 2003 1120 UTC.

2.1   AMSR-E data

The Advanced Microwave Scanning Radiometer for EOS (AMSR-E) is a multi-frequency, dual-polarized microwave radiometer on board the polar-orbiting Aqua satellite launched in May, 2002. AMSR-E is designed to retrieve column water vapor, column cloud water, surface precipitation rate, surface wind speed, sea ice

extent, SST, and other variables (Wentz and Meissner, 2007).

At middle and high latitudes, the AMSR-E typically overpasses a given feature twice in a 24-hr period. We therefore have two AMSR-E overpasses for each of the four polar low cases, and the times of these overpasses are the primary reference times for comparison with the model simulations. Overpass times are given in Table 1.

1.1.3 Precipitation retrievals

The University of Wisconsin Precipitation Algorithm (UWPA) for AMSR-E is a physical inversion algorithm for retrieving precipitation rate over the ocean (Petty, 1994). Physical information concerning surface precipitation rate is supplied not by the raw brightness temperatures but rather normalized polarizations for 18.7, 36.5, and 89.0 GHz (P19, P37 and P89), plus an 89.0 GHz polarization-corrected scattering index (S89) which is sensitive to scattering by ice.

The UWPA primarily relies on depolarization of ocean surface emission at lower frequencies for surface precipitation information. However, when depolarization due to liquid water is either too strong or too weak to be usable, the algorithm falls back on the empirically calibrated first guess rain rate based on S89. In this way, the dynamic range of the algorithm is extended to include both deep convection in the tropics and shallow frozen precipitation at high latitudes.

Retrieval of high-latitude ocean precipitation has historically been a major weak point of passive microwave methods (Petty, 1997). Owing to the shallowness

and typically light intensities characteristic of high latitude precipitating cloud systems, precipitation is often underestimated or overlooked completely by most published microwave algorithms. This is especially true in the absence of a rainfall at or near the surface. Although quantitative validation at high latitudes has also been difficult due to a lack of suitable data sources, preliminary comparisons of the UWPA estimates with monthly gauge totals at Jan Mayen Island (70.93 ° N, 8.67 ° W) suggest that the UWPA, unlike all other algorithms we have tested, is able to retrieve reasonably unbiased monthly precipitation amounts at high latitudes, even during the cold season (Fig. 2). The same algorithm also exhibited the best overall global correlation with ship-derived climatological precipitation frequencies, as documented during the Third Precipitation Intercomparison Project (PIP-3; Adler et al., 2001). Notwithstanding the apparently good *average* performance of the UWPA for cold air mass precipitation, we cannot rule out significant over- or underestimates in specific cases. Hence, agreement or disagreement of the UWPA retrievals with the model-simulated precipitation fields can be regarded only as circumstantial evidence concerning the comparative performance of the BMSs to be taken together with other objective and subjective criteria.
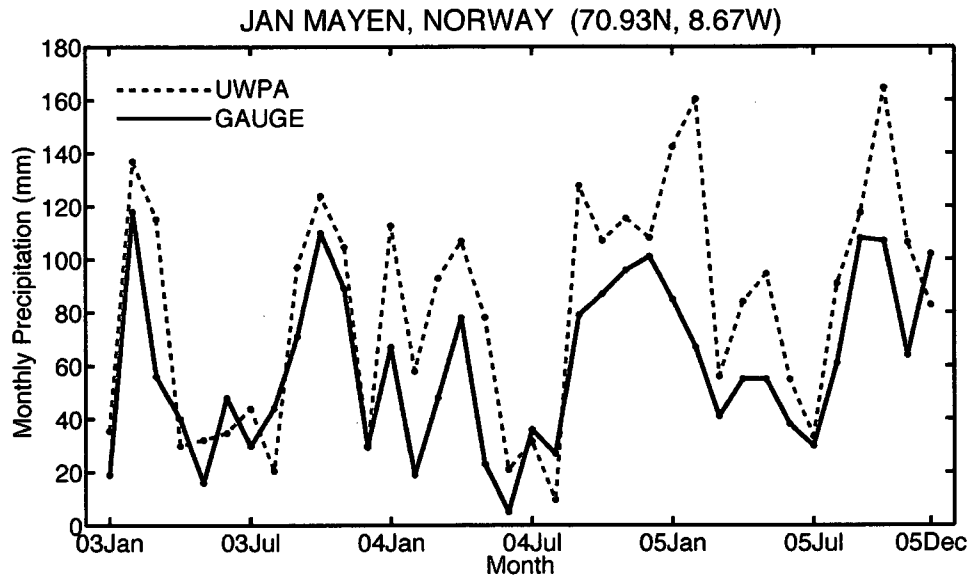
FIG 2 UWPA estimates of monthly over-ocean precipitation (dashed line) in the vicinity of Jan Mayen Island compared with gauge totals at the Jan Mayen meteorological station (70.93 °N, 8.67 °W) for 2003 through 2005. The mean ratio (UWPA to station) is 1.38; the correlation coefficient is 0.81.

1.1.4 Wind retrievals

The AMSR-E is also capable of retrieving sea surface wind speed (extrapolated to the standard 10-m reporting height) based on the influence of wind-induced roughening on the sea surface emissivity. Here we utilize the wind speed estimates included in the standard AMSR-E ocean products as described by Wentz and Meissner (2007).

2.2 AMeDAS data

The Automatic Meteorological Data Acquisition System (AMeDAS) gridded

precipitation data is a radar-based precipitation dataset covering Japan and the neighboring ocean areas. It is created from a composite of Japan Meteorological Agency (JMA) operational precipitation radars calibrated by the high density rain gauge network over Japan (Makihara et al., 1996). It is generated by the Japan Aerospace Exploration Agency (JAXA) and is a primary tool for satellite-derived precipitation validation. We utilize a subset matched to AMSR-E overpasses of Japan and surrounding regions in 2003. The dataset covers the region between $23°$ and $45°$N from $120°$ to $145°$E with a spatial resolution of approximately 6 km.

For the case over the Japan Sea in December 2003, the simulation results are compared with both the AMeDAS and UWPA products. Since there are no AMeDAS or similar data available for the other three cases, only the UWPA products are available in those cases.

2.3 MODIS cloud-top temperature

MODIS flies on the Aqua satellite together with the AMSR-E and provides high resolution multichannel infrared imagery at the same times as the AMSR-E overpasses. In this study, we utilize only the cloud-top temperature (CTT) derived from the 12 μm channel in 1 km resolution for qualitative comparison with the WRF-simulated CTT.

2.4 FNL analyses

The National Center for Environmental Prediction final (NCEP FNL) Operational Model Global Tropospheric Analyses are used to provide the initial fields and boundary conditions for the model simulations. The FNL analyses are output from the Global Forecast system (GFS) on $1^{\circ} \times 1^{\circ}$ resolution at every six hours. The atmospheric variables include surface pressure, sea level pressure, geopotential height, temperature, SST, soil values, ice cover, relative humidity, u- and v- component winds, vertical motion, vorticity and ozone. This dataset is available from http://dss.ucar.edu/datasets/ds083.2/.

Chapter 3 Synoptic Overviews

3.1 One case over the Sea of Japan

At 18 UTC 18 December 2003, an extratropical cyclone of modest intensity (labeled A in Fig. 3a) was located over the northwestern Pacific (Fig. 3a). A second, weaker low pressure system (labeled B in Fig. 3a) was located west of Hokkaido at the peak of a weak ridge in the 1000-500 hPa thickness. At the 500 hPa level, a cold low with a temperature minima of 229 K was located over the Eurasian continent, to the west of the weak surface low (Fig. 3b). At 350 hPa, which is near the tropopause, two significant positive PV features were evident (Fig. 3c). The eastern one was associated with extratropical cyclone A. The western one was associated with two PV maxima; one whose center was over the Eurasian continent, the other over the Sea of Japan. The former feature would lead to the initiation of the polar low investigated in this study.

FIG. 3 NCEP FNL analyses data at 18 UTC 18 December 2003. (a) SLP (solid lines, contoured at 4 hPa intervals) and 1000-500-hPa thickness (dashed lines, unit: 10m, contoured at 60 m intervals). (b) The 500-hPa geopotential height (solid lines, contoured at 60 m intervals), temperature (dash lines, contoured at 4 K intervals) and absolute vorticity (shaded). (c) The 350-hPa PV; PV is labeled in PVU (1 PVU = 10^{-6} m^2 K kg^{-1} s^{-1}) and contoured by every 1 PVU beginning at 1 PVU.

During the subsequent 12-h period, cyclone A moved east-northeastward, effectively leaving the analysis domain (Fig. 4a). Meanwhile, cyclone B moved southeastward and was located just east of Japan over the open ocean by this time, having deepened by 10 hPa to 992 hPa. A surface trough, which later developed into polar low P, was seen just west of Hokkaido, again in proximity to a local ridge in the 1000-500 hPa thickness (Fig. 4a). The confluent flow associated with this trough advected warm, moist marine air toward cold, dry continental air to the northwest. At 500 hPa level, the center of the cold low had moved southeastward toward the Sea of

Japan and deepened slightly (Fig. 4b). Two vorticity maxima, one (labeled S in Fig. 4b) associated with cyclone B, and the other (labeled N in Fig. 4b) with the surface trough, were evident at this time. The vorticity maximum N (S) was just upshear of the development region of the polar low P (cyclone B), consistent with the relationship of cyclonic vorticity advection by the thermal wind to upward vertical motion as described by Sutcliffe (1947) and Trenberth (1978). The 350-hPa PV feature associated with cyclone A had moved out of the region of interest by this time (Fig. 4c). The western PV feature retained a dipole structure as it moved over the Sea of Japan. The eastern maximum was associated with cyclone B while the western maximum, which had intensified in the intervening 12 hours, was centered over the Sea of Japan (Fig. 4c).
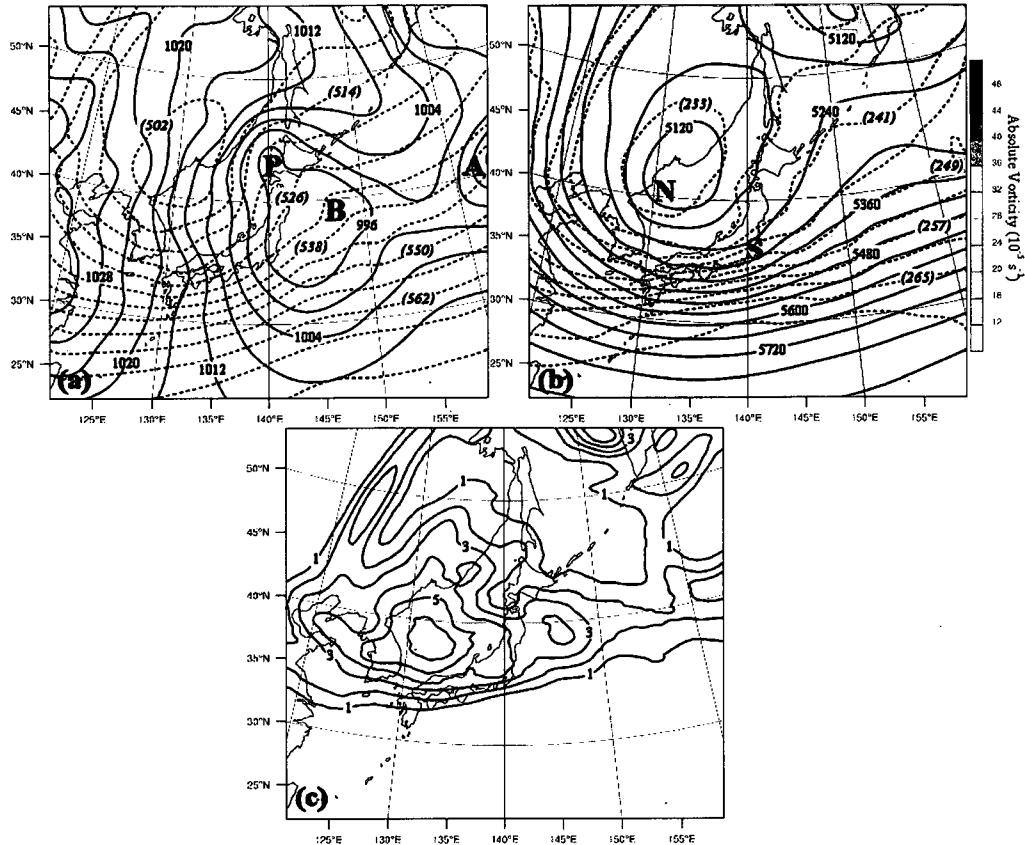
FIG. 4 NCEP FNL analyses data at 06 UTC 19 December 2003. (a) As for Fig. 3a. (b) As for Fig. 3b. (c) As for Fig. 3c.

By 18 UTC 19 December, cyclone B had deepened rapidly to a minimum SLP of 980 hPa (Fig. 5a). The surface trough originally west of Hokkaido had moved slightly southward, intensified somewhat, and was characterized by a strong pressure gradient to its northwest by this time (Fig. 5a). The development of this feature in the SLP field was accompanied by an intensification of its associated 1000-500 hPa thickness ridge as well. The polar low (labeled P in Fig. 5a) was the emerging feature in this developing trough. The cold low at 500 hPa had weakened somewhat and another low center was shown to the northeast of the cold low center. The vorticity maximum S moved eastward and covered a larger region (Fig. 5b). The vorticity maximum N, meanwhile, moved southeastward and had intensified by this time. The

350-hPa PV feature moved southeastward while deepening slightly and becoming zonally elongated (Fig. 5c).
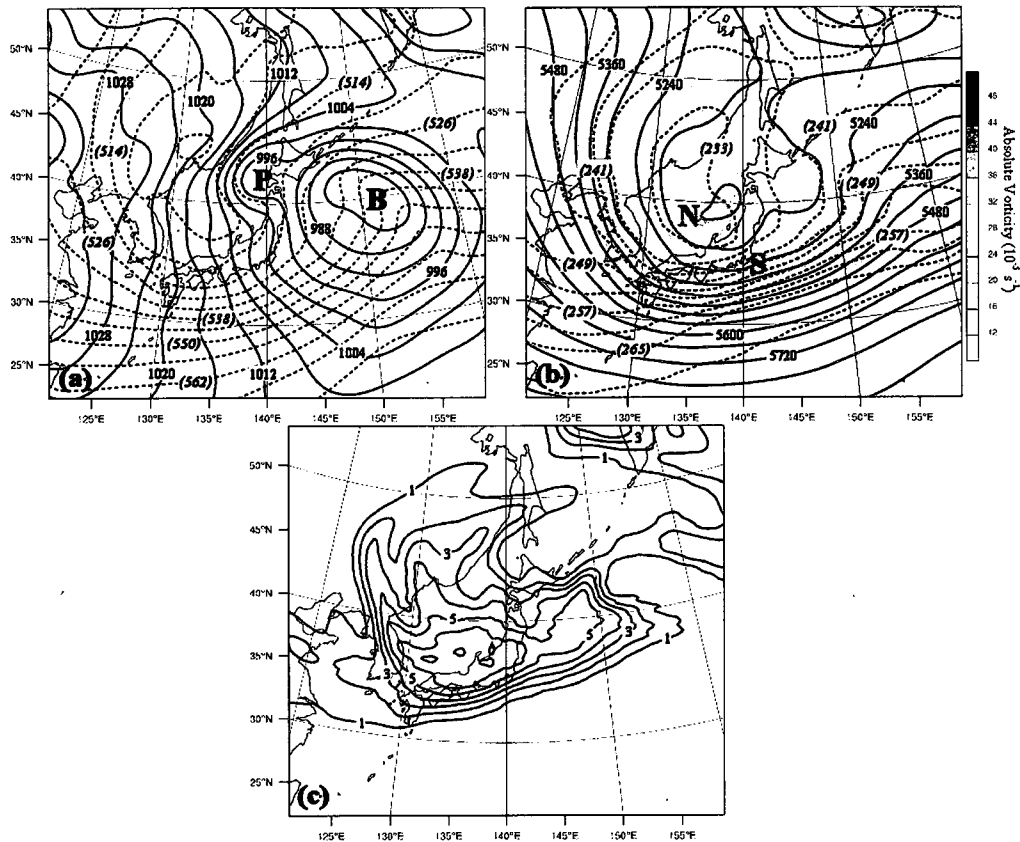
FIG. 5 NCEP FNL analyses data at 18 UTC 19 December 2003. (a) As for Fig. 3a. (b) As for Fig. 3b. (c) As for Fig. 3c.

Over the next 6 hours, cyclone B continued developing (Fig. 6a). A rapid development of the polar low also occurred during this time period. By 00 UTC 20 December, a closed low with a minimum SLP of 993 hPa had developed in association with the polar low (Fig. 6a) as it continued its southeastward movement. The cold low at 500 hPa continued to weaken meanwhile south of the cold low center, the vorticity maximum N started to merge with the vorticity maximum S (Fig. 6b). The PV feature at 350 hPa continued its southeastward movement, intensified by about 1 PVU (1 PVU = 10^{-6} m^2 K kg^{-1} s^{-1}) and continued to be stretched in the zonal

direction (Fig. 6c). The GOES-9 infrared (IR) image illustrates that a spiraliform polar low was fully developed with a clear eye at the center by 00 UTC 20 December (Fig. 7).
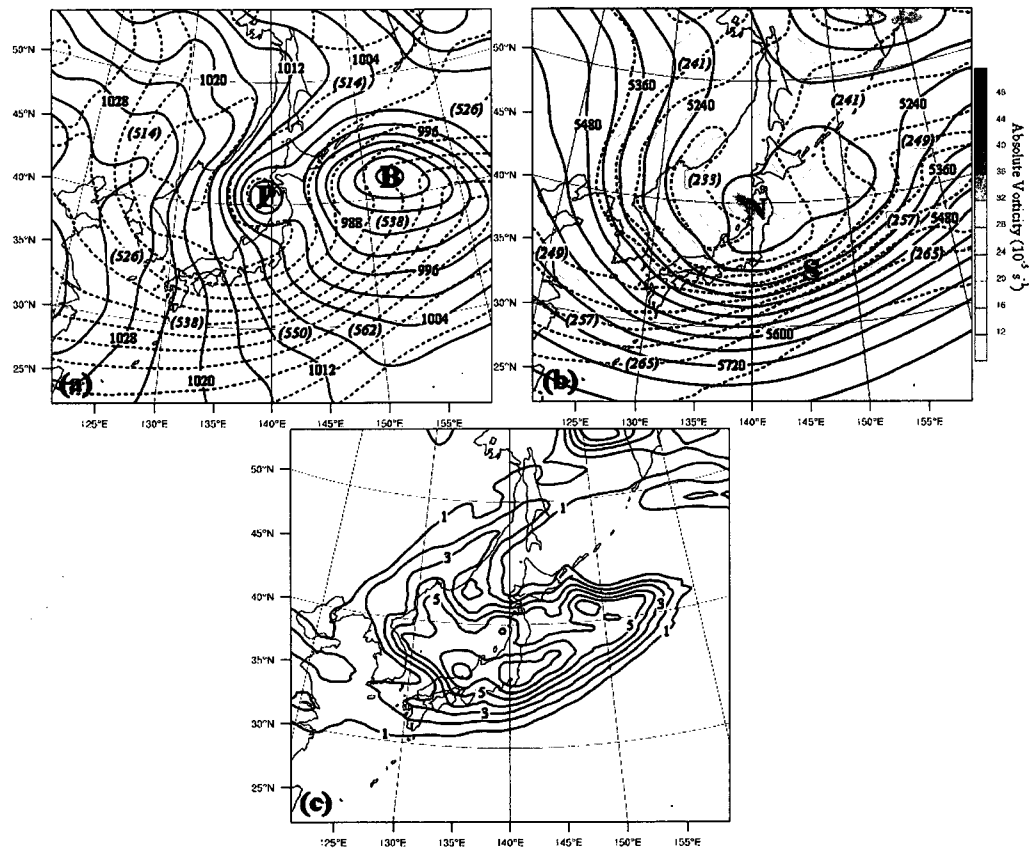
FIG. 6 NCEP FNL analyses data at 00 UTC 20 December 2003. (a) As for Fig. 3a. (b) As for Fig. 3b. (c) As for Fig. 3c.
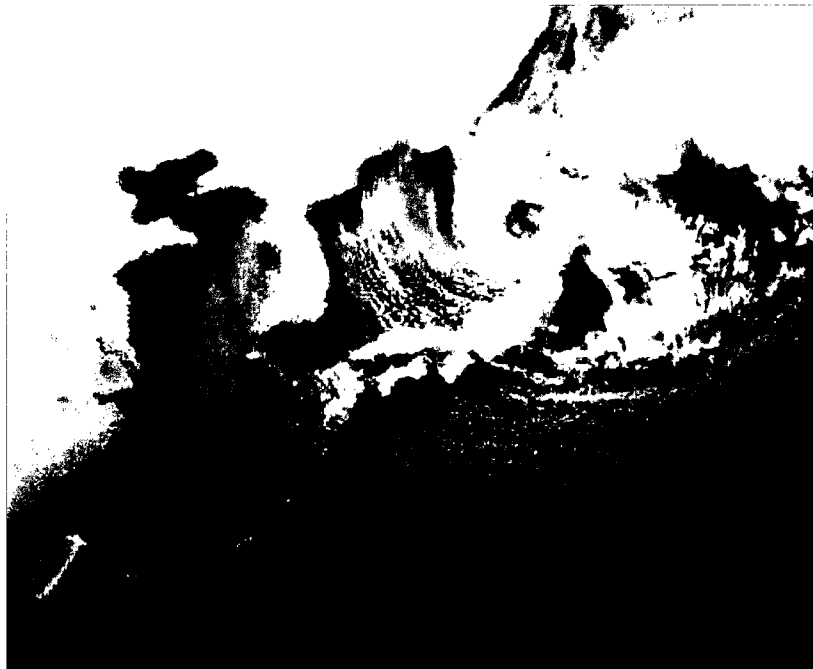
FIG. 7 GOES-9 IR imagery at 00 UTC 20 December 2003 shows a spiraliform polar low over Japan, with clear eye in the center. (http://weather.is.kochi-u.ac.jp/sat/gms.fareast/)

By 06 UTC 20 December, the polar low had moved over land and quickly dissipated (Fig. 8a). The cold low at 500 hPa had moved northeastward and had continued to weaken into a zonally elongated trough in which the two vorticity maxima in Fig. 8b had merged by this time (Fig. 8b). The 350-hPa PV was also characterized by weakening as well as further thinning and elongation by this time (Fig. 8c).
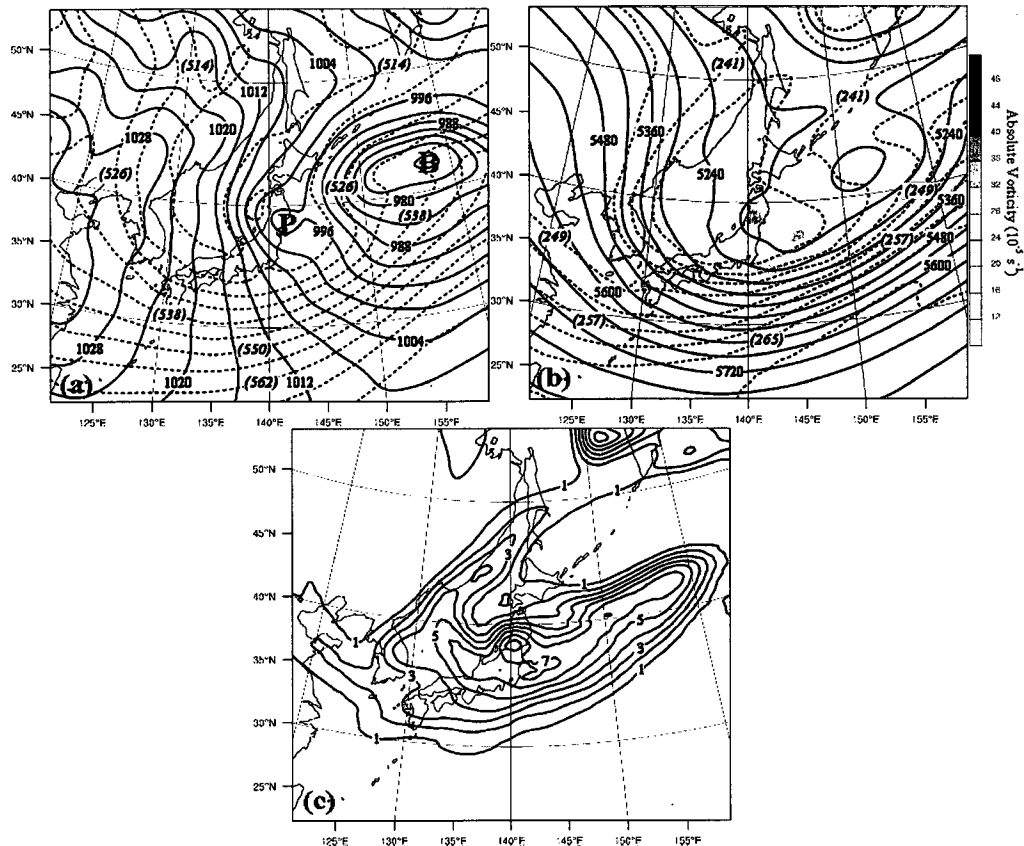
FIG. 8 NCEP FNL analyses data at 06 UTC 19 December 2003. (a) As for Fig. 3a. (b) As for Fig. 3b. (c) As for Fig. 3c.

Figure 1a depicts MODIS CTT at 0350 UTC 20 December. A spiraliform polar low is fully developed with a clear eye in the vortex center. Part of the polar low has moved over land. High clouds are shown west and northwest of the vortex center. To the north and northeast, a mid-level frontal cloud band separates the warm airmass from the cold airmass. Two more high cloud bands are shown over Japan, one over northern Japan and one just south of the vortex center. The extensive low-level cloud streets over the Sea of Japan reveal strong air-sea interaction there.

Figure 9 shows the AMSR-E-derived 10 m wind speed at the same time as the MODIS imagery in Fig. 1a, revealing that high speed winds nominally in excess 35 m s^{-1} exists on the southwestern flank of the polar low. It should be noted that the

calibration of the microwave-derived wind speeds is uncertain at such high wind

speeds.
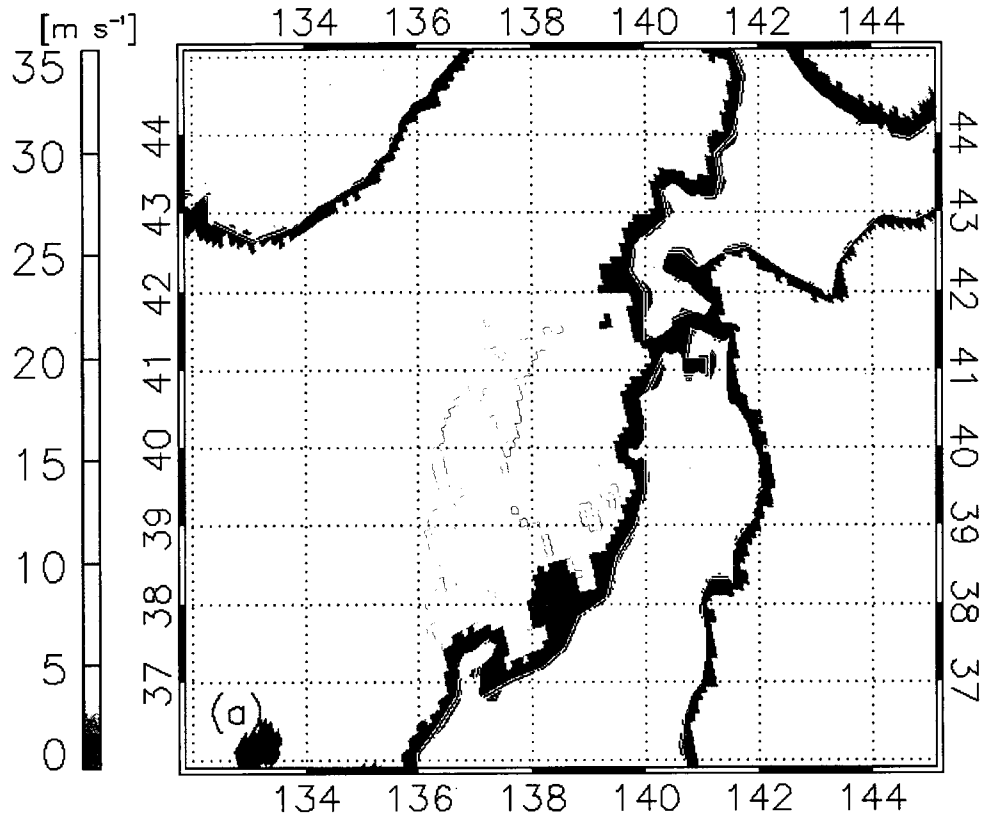
FIG. 9 AMSR-E derived wind at overpass time of 0350 UTC on 20 Dec. 2003.

The observational precipitation products are shown in Fig. 10a and 10b. The

observation time for both the AMeDAS and AMSR-E products is the same as that in

Fig. 1a. The AMeDAS product shows that strong precipitation larger than 4 mm hr^{-1} is

associated with high clouds on the southwestern flank of the polar low. Some

moderate precipitation is shown in the tail of the low. Also some light and moderate

precipitation is associated with the extensive cloud streets (Fig. 10a). The UWPA

product captures the main precipitation bands associated with the polar low over

ocean, including one band to the west of the Honshu island and two bands at the tail

of the polar low which located between 40 °N and 42 °N. The coverage by

precipitation is smaller while the rate is larger than that in the AMeDAS product (Fig.

10b). In the latter, almost no precipitation is detected in the range of $40°N$ to $41°N$

and $136°$ to $140°E$. Some light-to-moderate precipitation was estimated by the

UWPA algorithm there. It can be also noted that the UWPA product missed the

precipitation band near the low center and some small precipitation bands close to the

coast of the island. Most precipitation less than 1 mm hr^{-1} is overlooked by the UWPA

product. Although these significant differences exist in the details of the AMeDAS

and UWPA products, it is shown latter that their domain-averaged precipitation rates

are comparable.
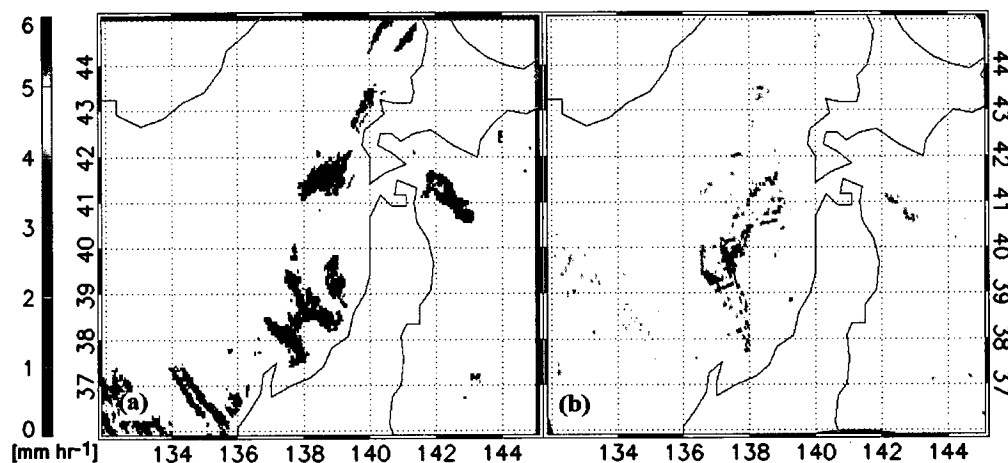
FIG. 10 The precipitation rate valid at 0350 UTC 20 December 2003: (a) The AMeDAS precipitation rate; (b) The UWPA precipitation rate. Gray areas where no observations are possible either for the AMeDAS or UWPA products. Precipitation rates less than 0.2 mm hr^{-1} are set to white.

3.2 One case over the Nordic Sea

At 12 UTC 16 January 2003, an extratropical cyclone (labeled A1) was

centered over northeastern Scandinavia (Fig. 11a). To the west of the cyclone center

over ocean, northerly and northeasterly winds advected cold air from over sea ice to

over the warm ocean. A ridge in the 1000-500 thickness was seen to the west of the Norwegian coast near 72°N 12°E where a polar low developed in the following hours. To the southwest, another extratropical cyclone (labeled B1) was seen over the North Atlantic. A warm tongue of SST, which favors the development of polar lows because of the thermal contrast between the cold air from over ice and the warm ocean, was seen along the Norwegian coast (Fig. 11d). Two vorticity maxima (labeled P2 and G2) along with two cold centers were shown at 500 hPa (Fig. 11b). As seen from the satellite imagery shown in later, two polar lows were developing in the following hours. Each of the vorticity maxima was associated with a polar low, respectively. However, the polar low associated with the vorticity maximum G2 was so small that it was not explicitly resolved in the FNL analyses. The WRF simulation also did not capture the development of this polar low. So we will not discuss the polar low associated with the vorticity maximum G2 here. At 350 hPa, three distinct PV maxima (labeled B3, P3 and G3) were seen at this time (Fig. 11c).
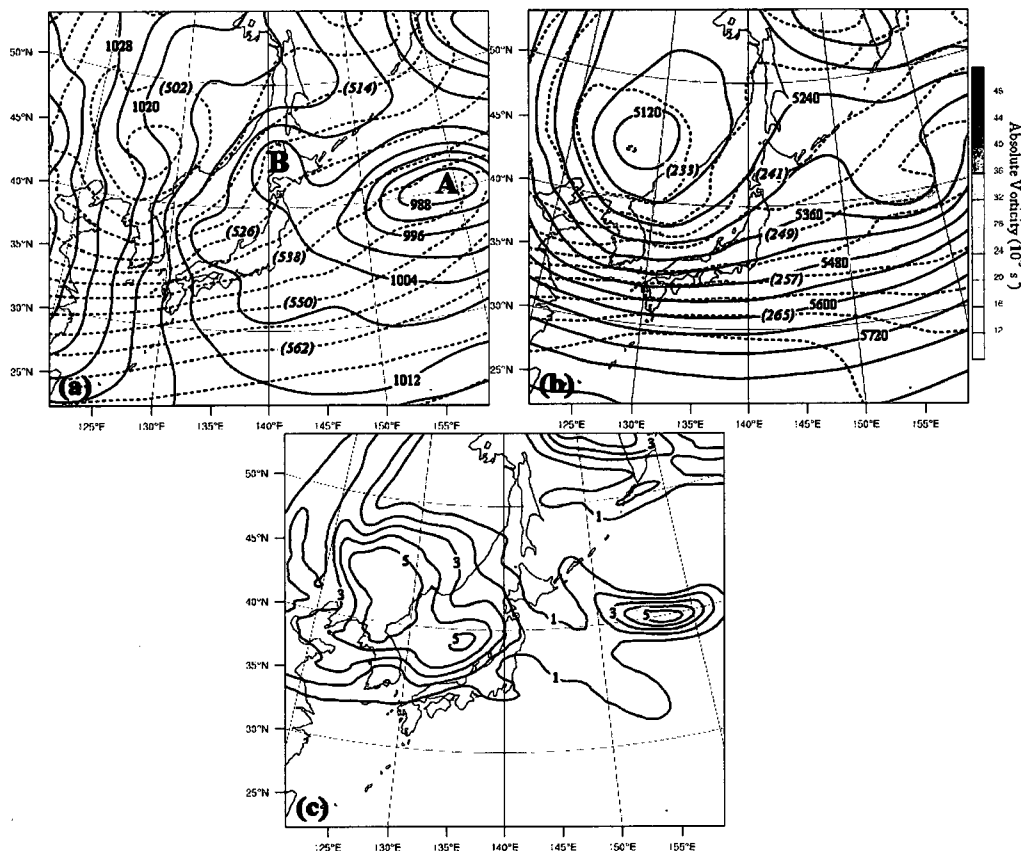
FIG. 11 NCEP FNL analyses data at 12 UTC 16 January 2003. (a) SLP (solid lines, contoured at 4 hPa intervals) and 1000-500-hPa thickness (dashed lines, unit: 10m, contoured at 60 m intervals). (b) The 500-hPa geopotential height (solid lines, contoured at 60 m intervals), temperature (dash lines, contoured at 4 K intervals) and absolute vorticity (shaded). (c) The 350-hPa PV; PV is labeled in PVU (1 PVU = 10^{-6} m^2 K kg^{-1} s^{-1}) and contoured by every 1 PVU beginning at 1 PVU. (d) The surface skin temperature (i.e., SST over ocean) contoured from 265 K to 289 K at 1 K intervals.

In the next 6 hours, both cyclone A1 and cyclone B1 moved northeastward while the first signs of an incipient polar low (labeled P1) quickly developed. By 18 UTC 16 January, polar low P1 had developed to the east of the Norwegian coast near 71°N 13°E with a closed low shown in the center (Fig. 12a). The ridge of 1000-500 hPa thickness has weakened by this time. At 500 hPa (Fig. 12b), the vorticity maximum P2 had moved slightly southeastward to a location just over the P1 region. The vorticity maximum B2 associated with cyclone B1 was seen over the North

Atlantic. At 350 hPa, the PV feature P3 moved southeastward and was elongated while the PV feature G3 showed more isotropy (Fig. 12c).
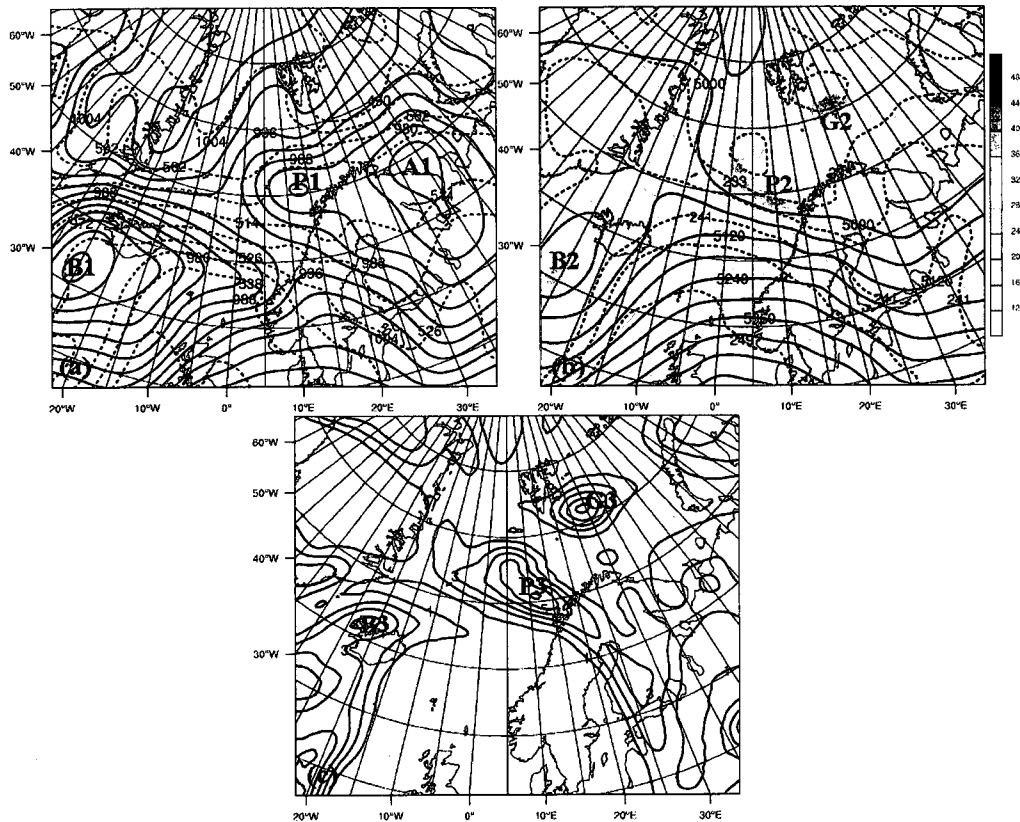
FIG. 12 NCEP FNL analyses data at 18 UTC 16 January 2003. (a) As for Fig. 11a. (b) As for Fig. 11b. (c) As for Fig. 11c.

During the subsequent 6-h period, cyclone A1 and cyclone B1 continued their northeastern movements with cyclone B1 closer to the polar low P1 (Fig. 13a). The polar low P1 had weakened along with the ridge in the 1000-500 hPa thickness. At 500 hPa, the vorticity maximum P2 continued its southeastward movement and was near the Norwegian coast with the decrease of its magnitude while the vorticity maximum G2 intensified (Fig. 12b). At 350 hPa, the center of the PV feature P3 was also near the Norwegian coast with a further elongation of the PV feature. At 0325 UTC 17 January 2003, a wave train with a series of lows (cyclone B, polar low P and

polar low G) were seen over the Nordic Sea (Fig. 14). The spiral shape of the polar

low P was clearly shown in the imagery while part of the polar low had merged with

cyclone B.
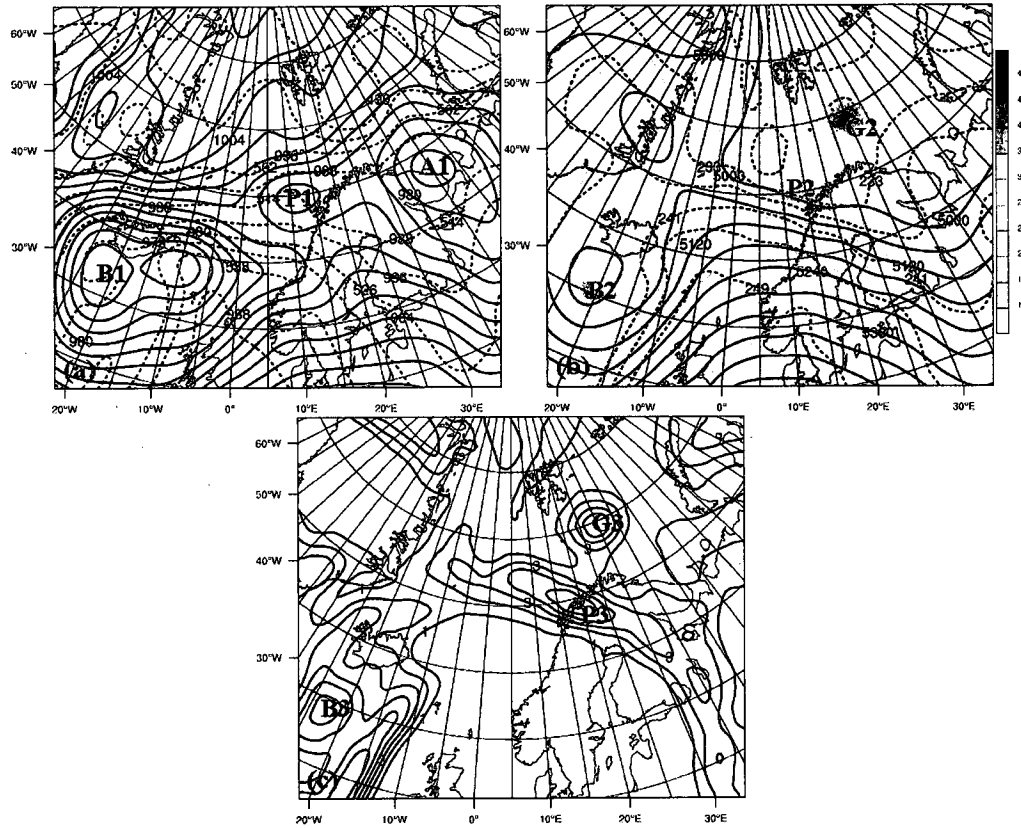
FIG. 13 NCEP FNL analyses data at 00 UTC 17 January 2003. (a) As for Fig. 11a. (b)
As for Fig. 11b. (c) As for Fig. 11c.
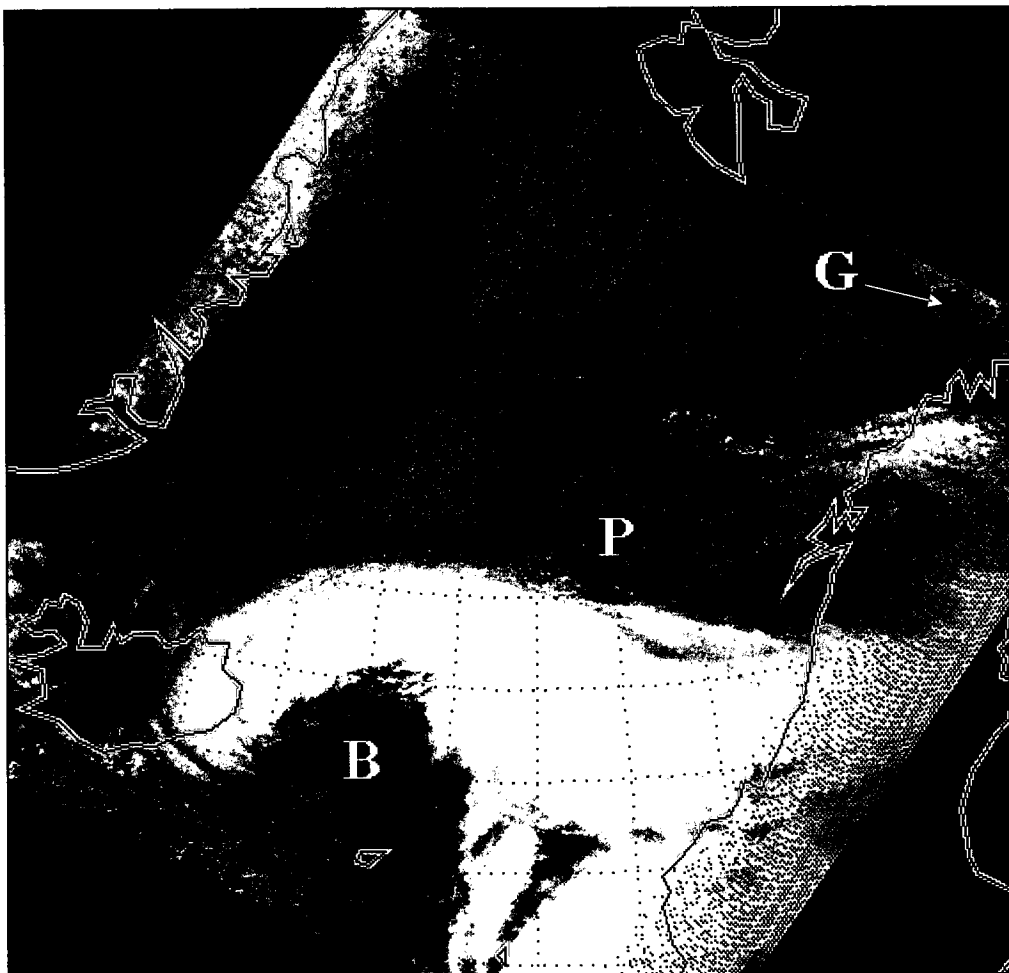
FIG. 14 MODIS IR imagery shows a train of cyclones (extratropical cyclone B, polar low P and polar low G) over the Nordic Sea. Valid at 0325 UTC 17 January 2003.

By 06 UTC 17 January, the polar low P1 merged with cyclone B1 (Fig. 15a).

The vorticity maximum P2 at 500 hPa significantly weakened while the PV feature at 350 hPa also weakened and further elongated (Fig. 15b and Fig. 15c). The development of this polar low occured in less than 1 day.
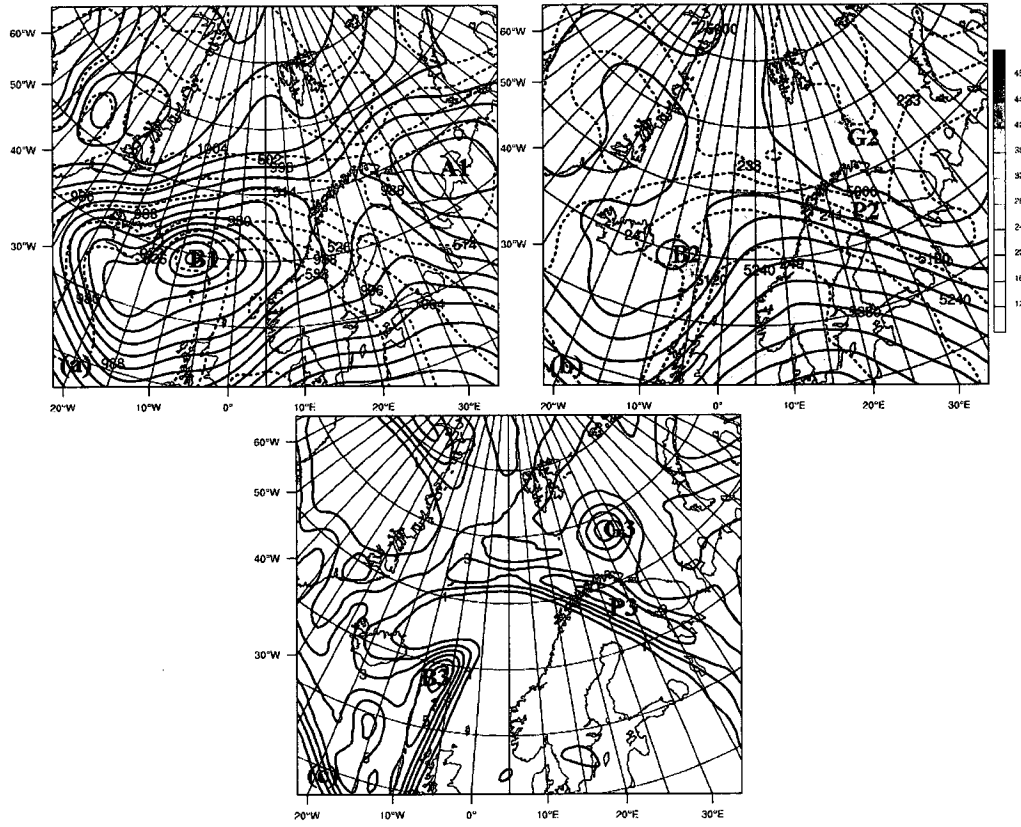
FIG. 15 NCEP FNL analyses data at 06 UTC 17 January 2003. (a) As for Fig. 11a. (b) As for Fig. 11b. (c) As for Fig. 11c.

Chapter 4   Model Description and Evaluation

4.1   Model description

WRF is a state-of-the-art mesoscale weather prediction system. It integrates the non-hydrostatic, compressible dynamic equations with an Arakawa C-grid using a terrain-following hydrostatic pressure vertical coordinate. The third version of the WRF model is used in this study. All our simulations were run with two nested domains at 25 km and 5 km horizontal resolution, respectively, and with 28 sigma levels in the vertical. A two-way nesting procedure is used to drive WRF with the initialization fields and boundary conditions obtained from the $1°x1°$ FNL datasets. In order to better examine the whole synoptic environment affecting the development of the polar low, the simulated domain in the PV inversion part is larger than that in the intercomparison part. The domains of the simulation over the Sea of Japan in January 2003 for PV inversion are shown in Fig. 16. More details of the model setup for each case are listed in Table 2 and Table 3.
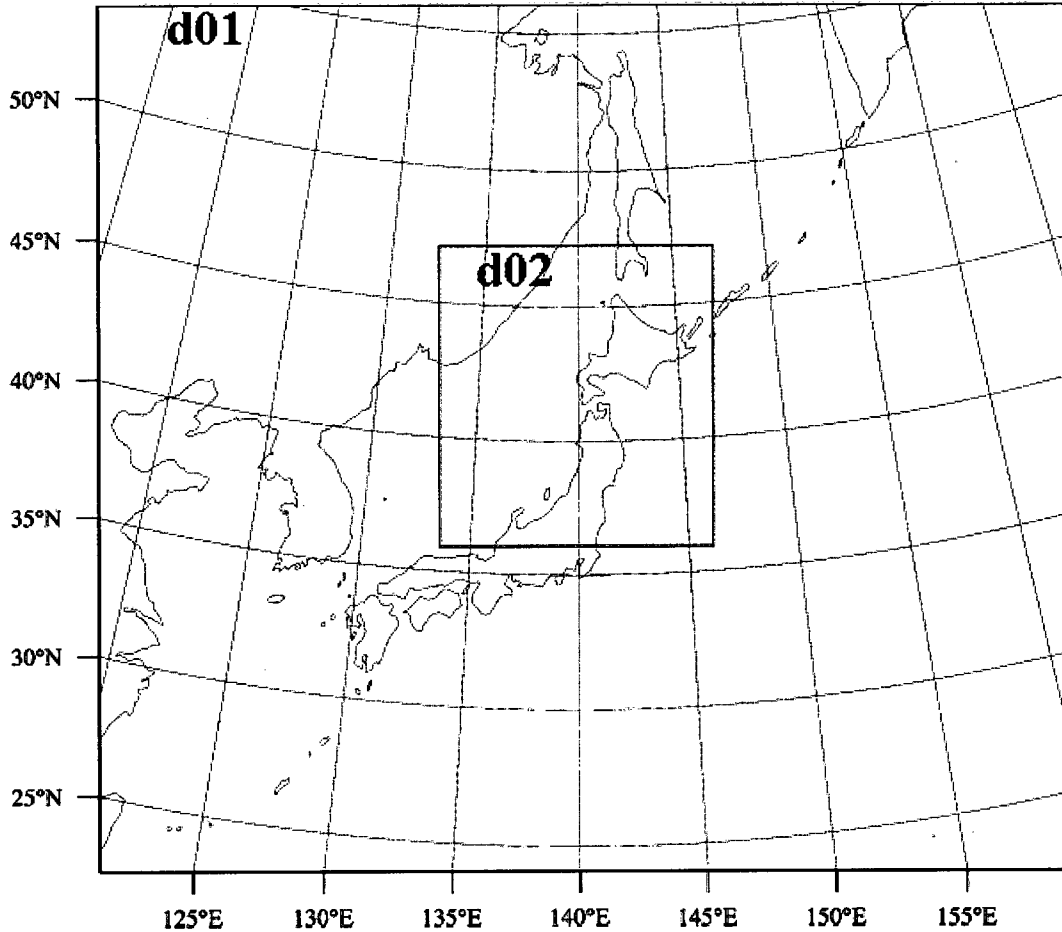
FIG. 16 Inner (d02) and outer (d01) domains of the WRF simulation used in the PV inversion study for the Sea of Japan case in December 2003.

Table 2 Details of model setup for each case used in BMS intercomparison. The grid size is represented by dimension of west-east grid by dimension of north-south grid.

	JP1	JP2	ND1	ND2
Grid size of outer domain	88x88	90x90	85x85	70x70
Center point of outer domain	38°N, 140°E	38°N, 135°E	70°N, 5°E	72°N, 18°E
Grid size of inner domain	176x196	201x201	201x266	151x151
Center point of inner domain	41.15°N, 140.29 °E	39.46°N, 135.15°E	70.78°N, 2.95°E	71.66°N, 17.64°E
Initial time	1800 UTC 18 Dec 2003	0000 UTC 04 Dec 2005	0600 UTC 16 Dec 2003	1800 UTC 04 Dec 2003
Forecast hours (h)	36	36	30	30

Table 3 Details of model setup for each case used in PV inversion. The grid size is represented by dimension of west-east grid by dimension of north-south grid.

	JP1	ND1
Grid size of outer domain	160x145	150x130
Center point of outer domain	40°N, 140°E	70°N, 5°E
Grid size of inner domain	226x251	211x251
Center point of inner domain	41.57°N, 139.70 °E	70.51°N, 9.39°E
Initial time	1800 UTC 18 Dec 2003	0600 UTC 16 Dec 2003
Forecast hours (h)	42	36

The principal physical schemes used in the simulations include the Yonsei University (YSU) planetary boundary layer (PBL) scheme (Hong et al., 2006), the Rapid Radiative Transfer Model (RRTM) longwave scheme (Mlawer et al., 1997) and the Dudhia (1989) shortwave scheme. A modified version of the Kain-Fritsch cumulus parameterization scheme (Kain and Fritsch, 1990, 1993) is used in the outer domain. Since the convective process can be marginally resolved at 5 km resolution, no cumulus scheme is used in the inner domain as suggested by the WRF technical note (Skamarock et al. 2008). The five mixed-phase BMSs employed in the intercomparison study include the Purdue Lin (Chen and Sun, 2002), the WRF Single-Moment 6-class (WSM6) (Hong and Lim, 2006; Dudhia et al., 2008), the Goddard Cumulus Ensemble (GCE) models (Tao and Simpson, 1993), New Thompson et al. (2008), and the Morrison et al. (2009) 2-Moment scheme.

All these BMSs are mixed-phase schemes and include six classes of water substances: water vapor, cloud water, rain, cloud ice, snow and graupel. The core part of the Lin scheme for representing clouds and precipitation processes is based on Lin et al. (1983) and Rutledge and Hobbes (1984). The size distribution of the rain, snow and graupel are represented as exponential functions. The interactions among these

six water substances counted in this scheme include evaporation/sublimation, deposition/condensation, aggregation, accretion, Bergeron processes, freezing, melting, and melting evaporation. Some modifications including the saturation adjustment in Tao et al. (1989) and ice sedimentation are also applied. The WSM6 scheme is similar but has the revised ice process treatment of Hong et al. (2004) and a revised terminal velocity for snow and graupel (Dudhia et al., 2008). The GCE scheme is also based on the Lin scheme, with some modifications for ice/water saturation (Tao et al., 1989, 2003).

A large number of improvements to physical parameterizations are implemented in the New Thompson scheme (Thompson et al., 2008). For example, compared to the single-moment BMSs, the New Thompson includes a 2-moment prognostic scheme for cloud ice, while other single-moment components are forced to behave more like 2-moment schemes. Also, snow aggregates are treated as fractal-like, with a bulk density that varies inversely with diameter. Their size distribution is represented as a sum of exponential and gamma distributions.

The Morrison et al. (2009) scheme is a 2-moment scheme based on Morrison et al. (2005) and Morrison and Pinto (2006). Prognostic variables including number concentrations and mixing ratios of the six water substances whose particle size distributions are represented as gamma functions. The size distribution intercept parameter of each hydrometeor is a specified as a function of the predicted number concentration and mixing ratio.

More details of these BMSs are given by Skamarock et al., (2008).

After intercomparing the performance of these BMSs, the WSM6 scheme, which is marginally superior to others in reproducing cloud and precipitation processes, is used in the simulations for PV inversion.

4.2 Evaluation of model outputs

In order to use the WRF model to evaluate the performance of BMSs in polar low simulations and investigate its development process, it is important to show that the simulations reasonably reproduce the dynamical evolution of the polar low itself. A limited verification of the simulations is presented here. Four simulations were undertaken for polar lows developing under similar synoptic conditions, and the results for all simulations were broadly similar. The following evaluation of the synoptic fields therefore mainly focuses on one representative simulation at 25 km resolution from the intercomparison study of the BMSs for the case over the Sea of Japan in December 2003. The WSM6 is used in the simulation.

Shown in Fig. 17 are the SLP and 1000-500 hPa thickness analyses from FNL datasets at 6-h intervals from 00 UTC 19 December to 06 UTC 20 December. Figure 18 shows the forecasts with 25 km resolution at 6-h intervals from 00 UTC 19 December to 06 UTC 20 December. The overall evolution of the simulated polar low is similar to the corresponding FNL analyses. But a closed low developed earlier in the simulation than in the FNL analyses and with lower minimum SLP. The trajectory of the polar low is shown in Fig. 19. The position was identified when a closed low

was seen over the SLP fields. At the initial stage, the simulated low was a little west of the polar low center in the analysis data. Over time, the simulated low moved to the northeast of the analyzed position.
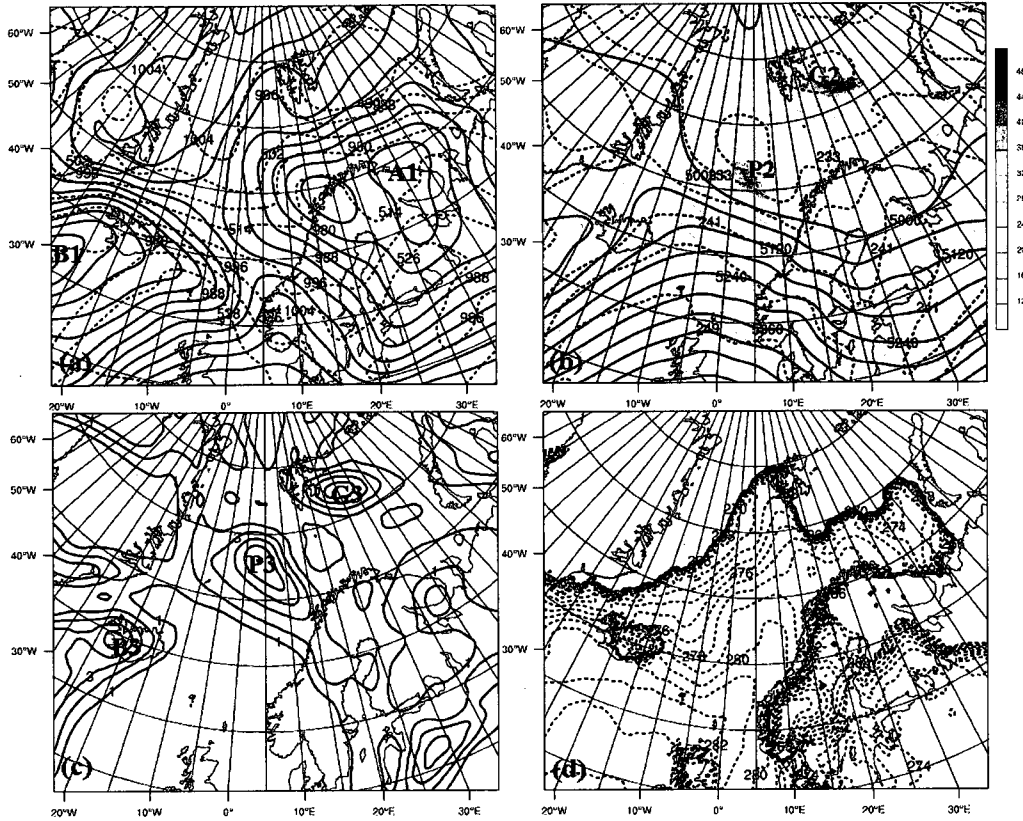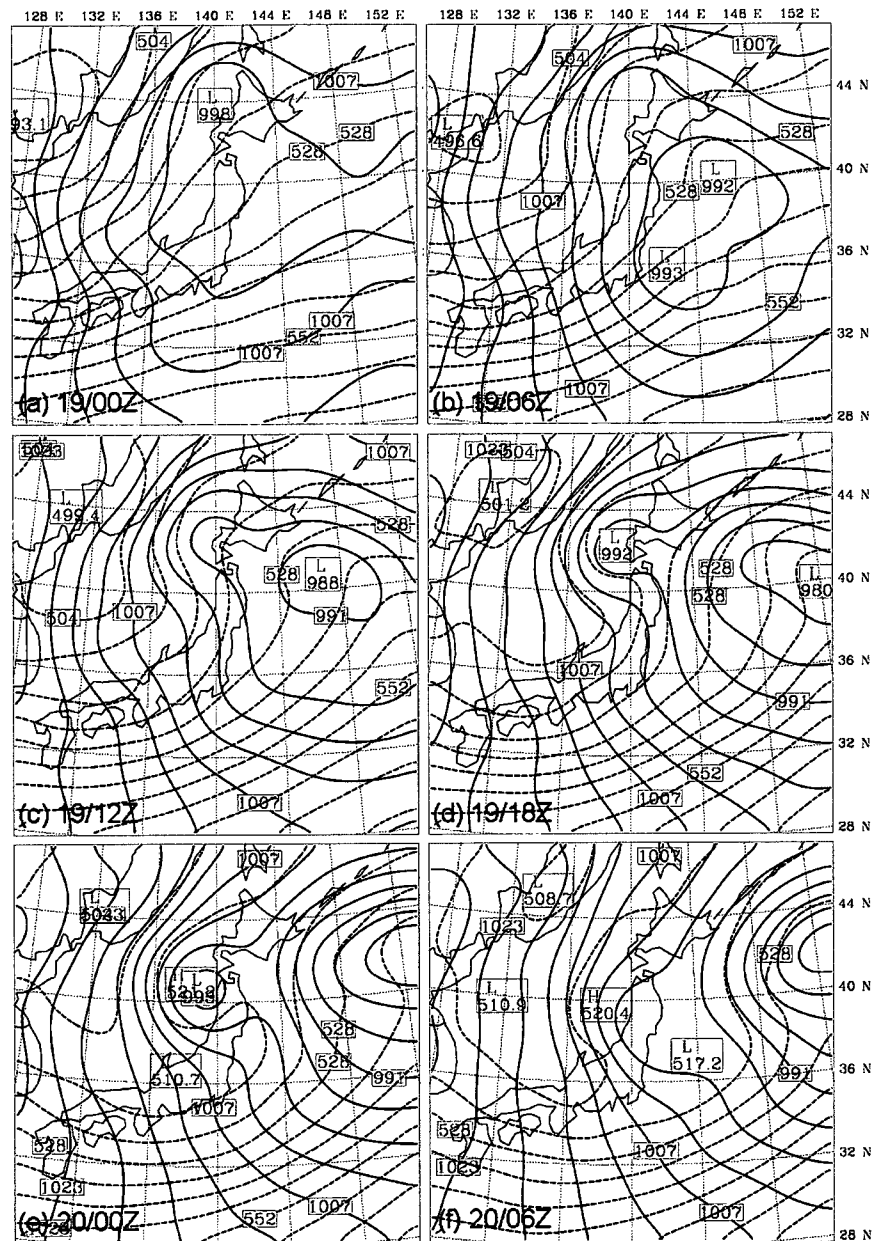

FIG. 17 NCEP FNL analyses of SLP (solid lines, contoured at 4 hPa intervals) and 1000-500-hPa thickness (dashed lines, contoured at 60m intervals) valid at (a) 00 UTC 19 Dec 2003; (b) 06 UTC 19 Dec 2003; (c) 12 UTC 19 Dec 2003; (d) 18 UTC 19 Dec 2003; (e) 00 UTC 20 Dec 2003; (f) 06 UTC 20 Dec 2003.
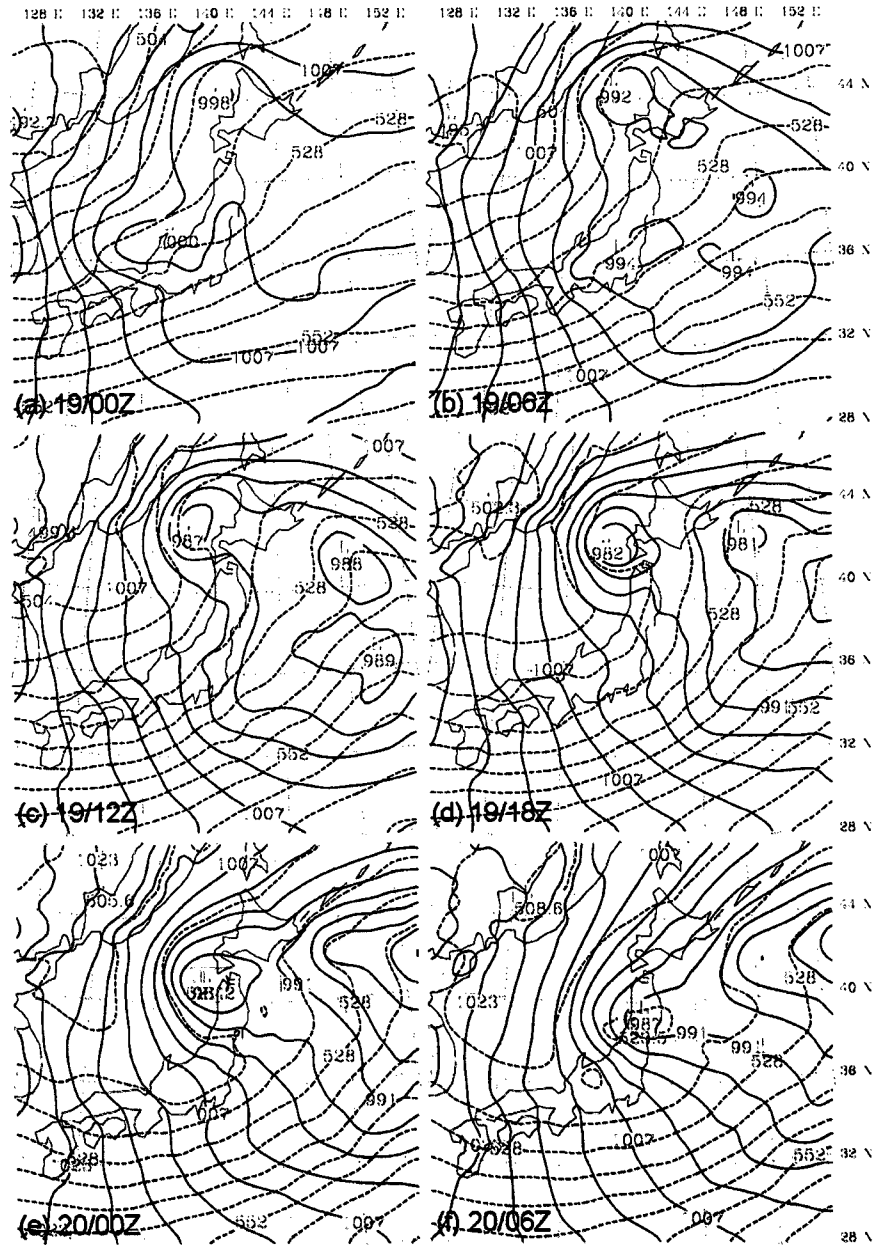
FIG. 18 WRF forecast of SLP (solid lines) and 1000-500-hPa thickness (dashed lines) (a) 6-h forecast valid at 00 UTC 19 Dec 2003; (b) 12-h forecast valid at 06 UTC 19 Dec 2003; (c) 18-h forecast valid at 12 UTC 19 Dec 2003; (d) 24-h forecast valid at 18 UTC 19 Dec 2003; (e) 30-h forecast valid at 00 UTC 20 Dec 2003; (f) 36-h forecast valid at 06 UTC 20 Dec 2003.
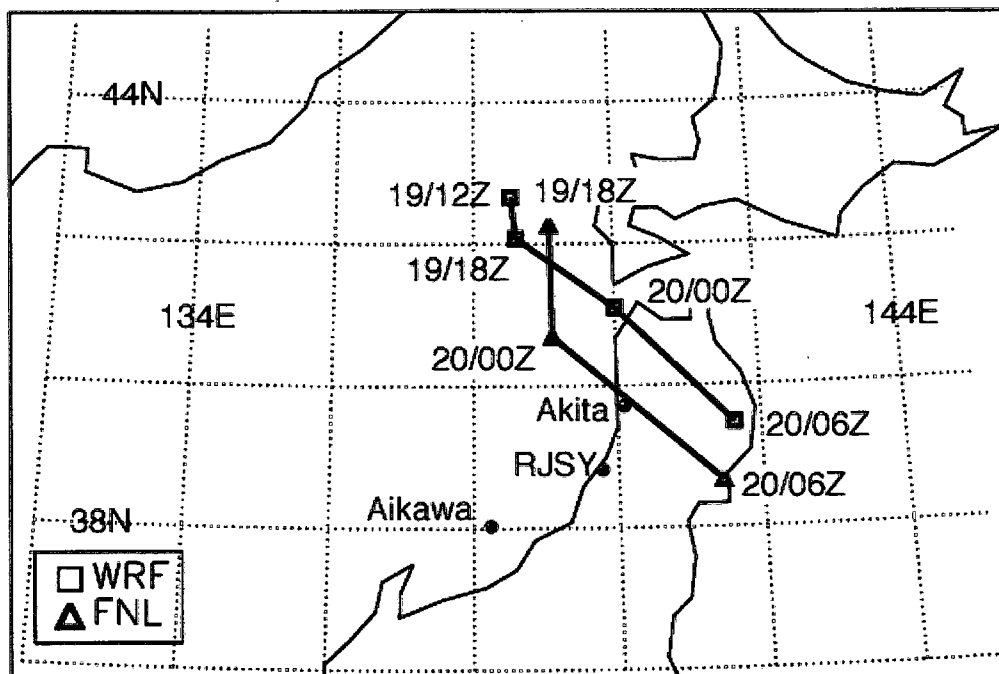
FIG. 19 The trajectory of polar low center as obtained from the WRF simulation at 25 km resolution (squares) and the FNL analyzed data (triangle) with 6-h intervals. The position was identified when a closed low was seen over the SLP fields. The FNL analyses are from 18 UTC 19 December 2003 to 06 UTC 20 December 2003. The WRF simulations are from 12 UTC 19 December 2003 to 06 UTC 20 December 2003.

At 03 UTC 20 December 2003, the center of the polar low passed the weather station Akita located at 39.72°N, 140.10°E. The location of the station is shown in Fig. 19. The station recorded a pressure drop of 7.9 hPa associated with the development of the polar low (Fig. 20a). The simulated SLP agreed very well with the observations during the first couple of forecast hours. Then a polar low started to develop earlier than the observations, and more strongly, consistent with Fig. 12. The minimum SLP passed Akita one hour later than in the simulation. The observations at Aikawa, which is a small island over the Sea of Japan, show the same trend but with smaller difference between observations and simulations (Fig. 20c).
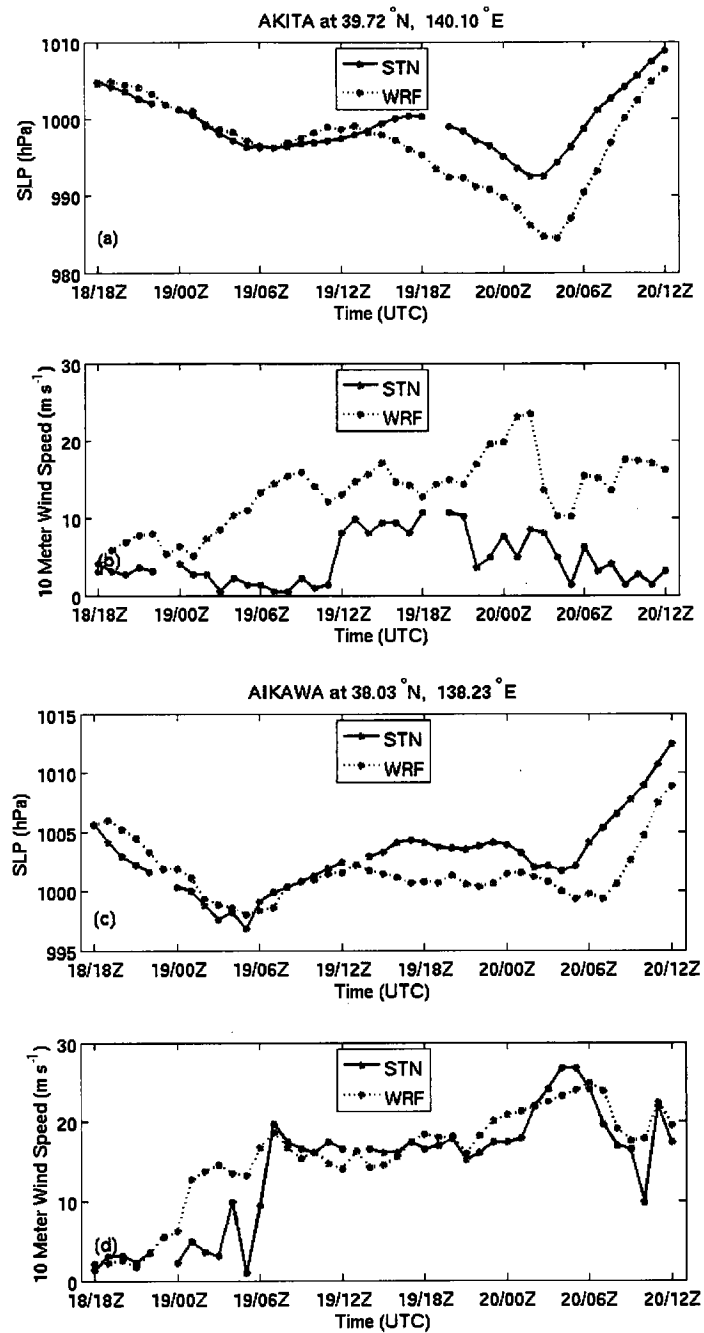
FIG. 20 Time series of modeled (dashed) and station-observed (solid line) SLP and wind speed at Akita (39.71°N, 140.10°E) and Aikawa (38.03°N, 138.23°E). (a) Akita SLP. (b) Akita wind speed. (c) Aikawa SLP. (d) Aikawa wind speed.

The 5 km-resolution simulated wind speed field at 04 UTC 20 December is presented in Fig. 21. The maximum wind speed of 28 m s^{-1} is smaller than the AMSR-E wind product in Fig. 9. The large-scale wind pattern generally agrees with the AMSR-E wind product but with more fine-scale structures produced by the simulation. At Aikawa, the highest wind speed of 29 m s^{-1} was recorded at 04 and 05 UTC 20 December. For most of the time period, the modeled wind speed matched up well with the observed one (Fig. 20d). However, a peak of high wind speed up to 24 m s^{-1} was shown the simulation while no high wind speeds were recorded at Akita (Fig. 20b). This is because the center of the simulated polar low passed about 100 km northeast of the analyzed center.
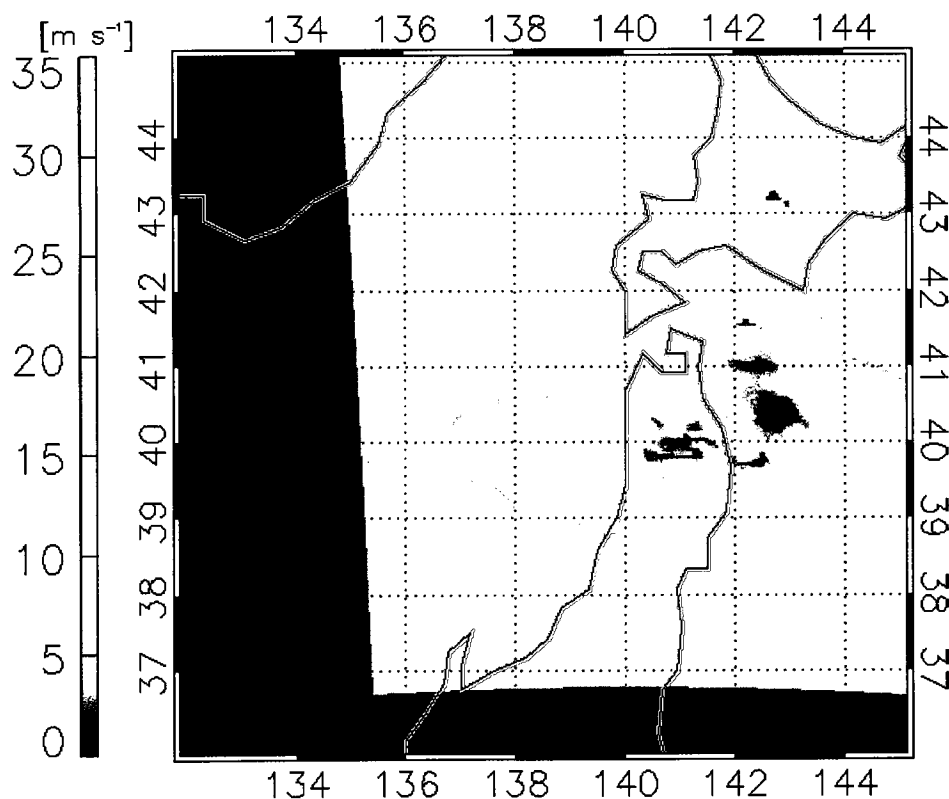
FIG. 21 The 0400 UTC model-simulated wind speed at 5 km resolution using the WSM6 scheme.

Figure 22 shows the sounding data at Akita. At 12 UTC 19 December 2003, the profiles of temperature and dew point temperature match up very well between the simulation and observation except that the dew point temperature is a little lower in the simulation (Fig. 22a). Above the 900 hPa level, the profiles still show reasonable agreement at 00 UTC 20 December (Fig. 22b). However, below that layer, the simulated temperatures are several degrees higher than the observations. The observed surface temperature was approximately $0\,^{\circ}$C while the simulated temperature is about $6\,^{\circ}$C.
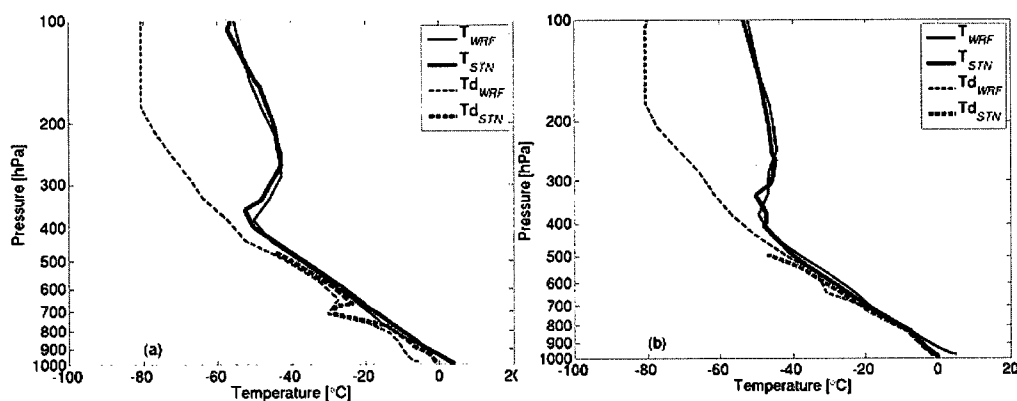
FIG. 22 Observed (thin lines) and simulated (thick lines) atmospheric temperature (solid) and dewpoint (dashed) profiles at Akita valid at (a) 12 UTC 19 Dec 2003 and (b) 00 UTC 20 Dec 2003.

Overall, the WRF model fairly accurately reproduced the synoptic-scale environment within which the polar low developed despite some differences between the FNL analyses, observations and the simulations. We therefore confidently employ output from the simulations in our investigation of the effect of different BMSs on polar low simulations and their development processes.

Chapter 5   Intercomparison of Bulk Microphysics Schemes in Simulations of Polar Lows

5.1   Cloud-top temperature

Figure 23 displays the 5 km resolution CTTs from the five BMSs valid at 04 UTC 20 December, 2003. For all these five BMSs, the location of the low center is a little further north than the observation and the orientation of the polar low shows more of counterclockwise rotation. However, the relative position of the polar low between these simulations is almost consistent. It reveals that different BMS do not significantly influence the propagation of the low system.

The BMS choice does, however, strongly affect the simulated CTT. For example, in the Lin scheme (Fig. 23b), the northern flank of the polar low is almost entirely covered by high clouds with similar CTT. The WSM6 (Fig. 23c) produced reasonable extent and structure of the cloud shield. High clouds are associated with the polar low and low clouds correspond to cloud streets. The shape of the cloud shields in the GCE scheme is similar with the WSM6. But there are fewer high clouds, and the high clouds have a looser structure (Fig. 23d). For the New Thompson scheme (Fig. 23e), almost no high clouds were produced corresponding to the polar low. The Morrison 2-moment scheme (Fig. 23f) has more high-cloud coverage. Overall, the Lin and New Thompson did poorly in producing cloud fields while the cloud fields in

other three schemes seem fairly realistic.
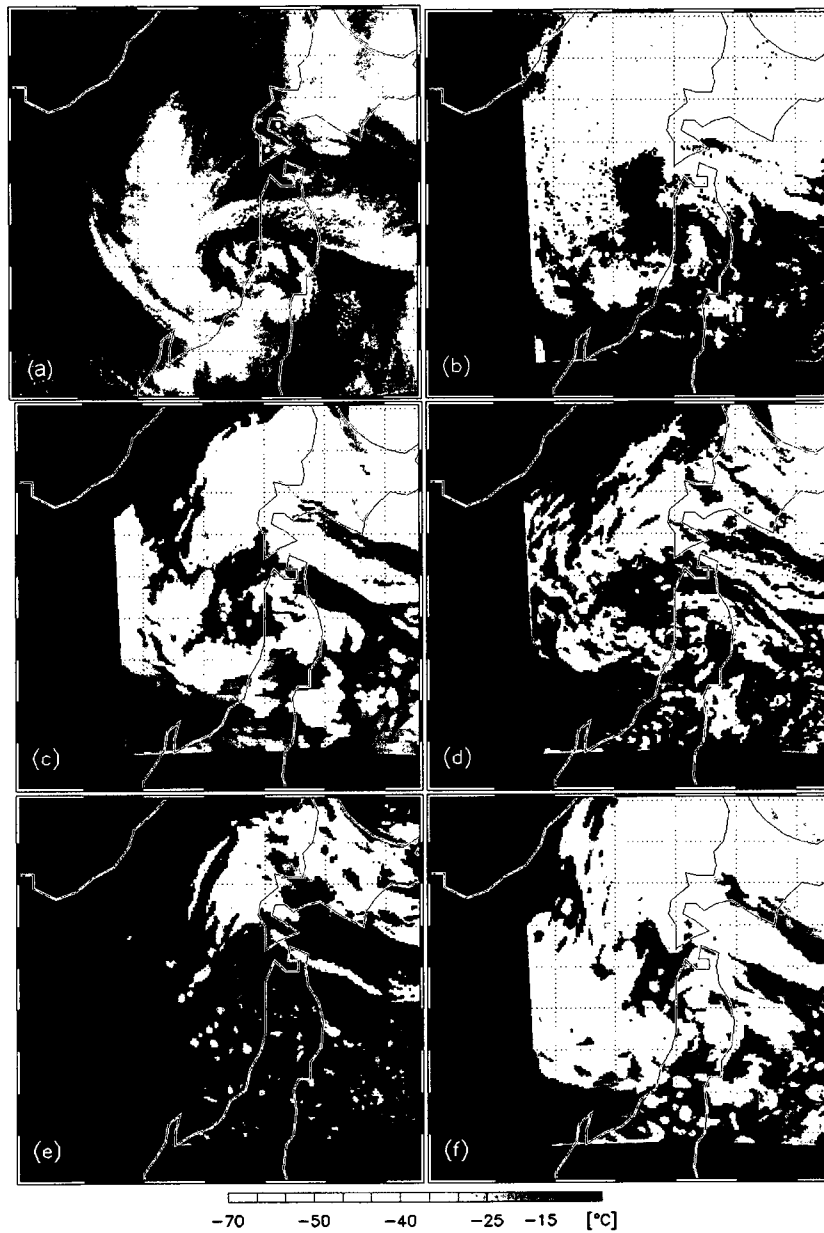
FIG. 23 Simulated CTT at 5 km resolution for (b) Lin; (c) WSM6; (d) GCE; (e) New Thompson and (f) Morrison 2-moment. Valid at 04 UTC 20 Dec 2003. The MODIS CTT is shown in (a) for comparison.

5.2 Precipitation

The simulated precipitation rates at 5 km resolution are shown in Fig. 24 as generated by the explicit microphysics scheme; no cumulus parameterization was used in the inner domain. All five experiments successfully reproduced the main pattern of the precipitation associated with the polar low. The precipitation associated with the cloud streets and the precipitation over land are also depicted in the simulations. Comparing the five simulations, both the Lin and WSM6 schemes show precipitation rates greater than 4 mm hr^{-1} while in others the maximum rate is smaller. More complex precipitation structures are depicted in the Lin scheme (Fig. 24a). The precipitation pattern is smoother in the GCE scheme (Fig. 24c).
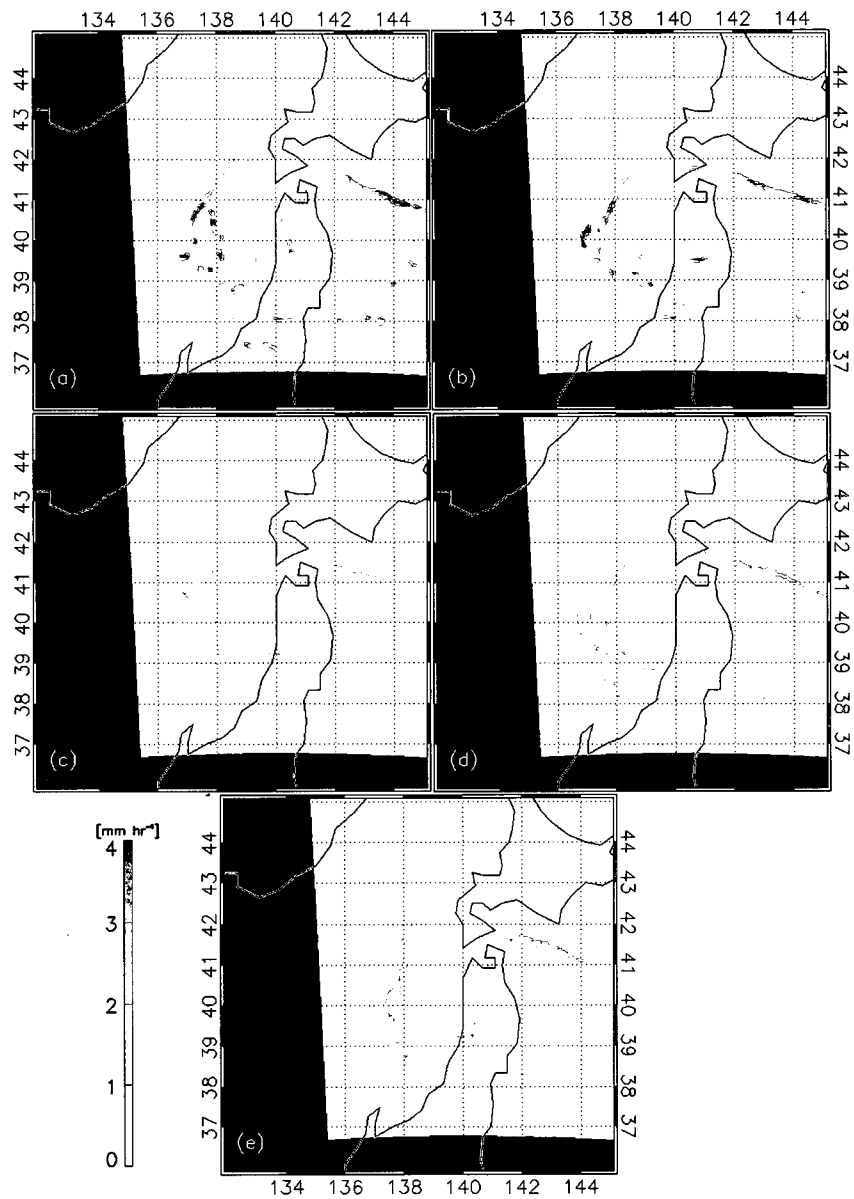
FIG. 24 The simulated precipitation rate at 5 km resolution for (a) Lin; (b) WSM6; (c) GCE; (d) New Thompson and (e) Morrison 2-moment. Valid at 04 UTC 20 Dec 2003.

In order to illustrate the three-dimensional structure of the simulated water substances, Figure 25 depicts the vertical profiles of domain-averaged water content for each hydrometeor (leftmost column) and the column-integrated water content for cloud water, cloud ice, snow and graupel (remaining columns). The domain-averaged water content is only calculated over a box that encompasses the precipitation associated with the polar low. All of these schemes show light rainfall near the surface, and column-integrated rain water is fairly similar for all five schemes (not shown), which is consistent with the station observations of showers of mixed rain and snow and with surface air temperatures only 1-3 degrees above freezing. Column-integrated water vapor (not shown) is fairly similar among all five schemes, but dissimilar from AMSR-E-observed product (Wentz and Meissner, 2007) in having considerably more fine scale structure but less area covered by low values.

For the Lin scheme (Fig. 25, row a), the primary hydrometeor type from 950 hPa to 500 hPa is graupel, in sharp contrast to all four other schemes. The maximum domain-averaged graupel content appears around 900 hPa with a value close to 0.12 g m^{-3}. It produced widespread graupel in the lowest layers, even in stratiform areas. Very little column-integrated snow is predicted. What little snow is present is mainly found at high levels in the clouds, and little or no snow is found in the lowest layer. The widespread graupel may be related to the parameterization of the terminal velocity for snow and graupel, which was subsequently modified in WSM6 with an aim to achieving more reduced conversion rates from snow to graupel (Dudhia et al., 2008).
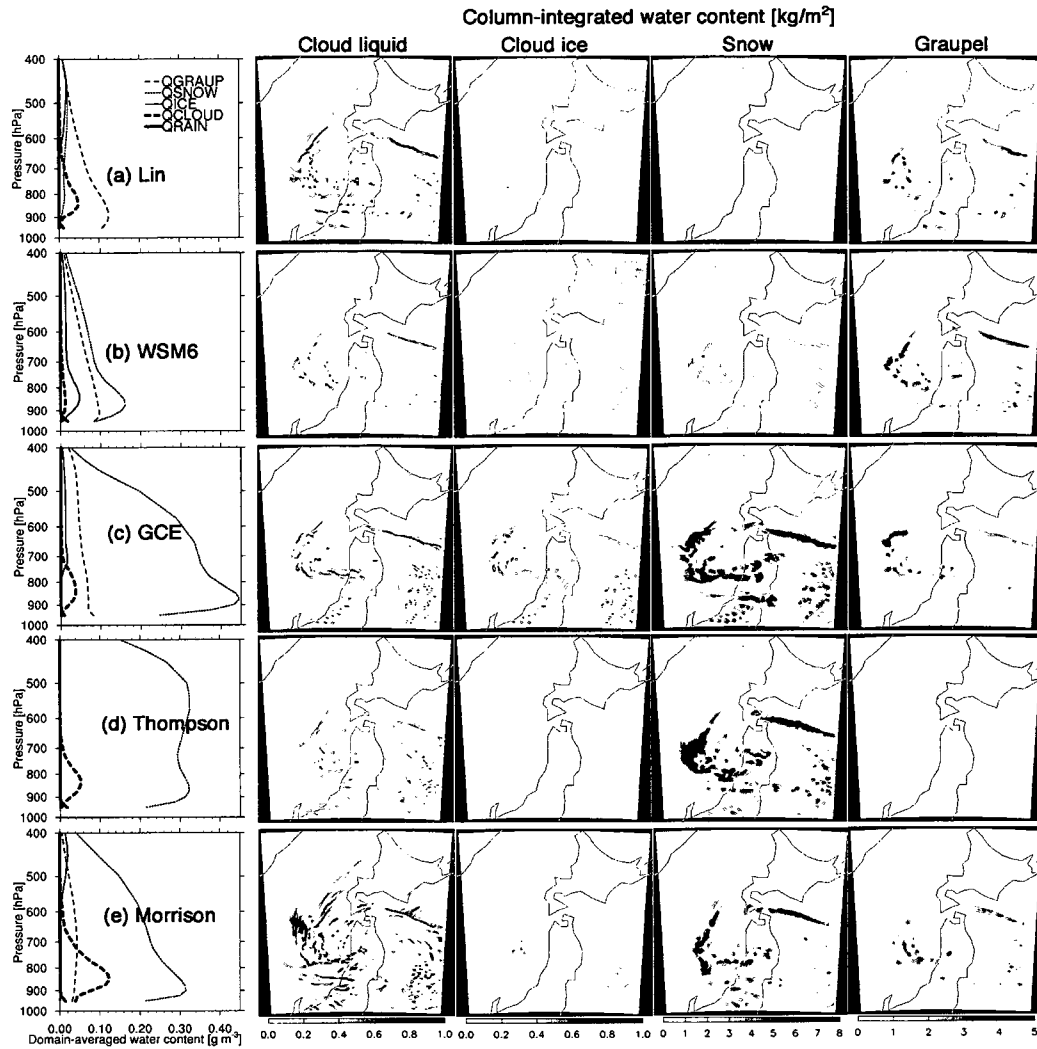
FIG. 25 The distribution of water contents at 04 UTC 20 Dec 2003 for (a) Lin, (b) WSM6, (c) GCE, (d) New Thompson, and (e) Morrison 2-moment. The first column (1) is the vertical distribution of the domain-averaged water contents for cloud water (QCLOUD), cloud ice (QICE), snow (QSNOW), rain (QRAIN) and graupel (QGRAUP). Subsequent columns are the column-integrated water content (kg/m²) for: (2) cloud liquid water, (3) cloud ice, (4) snow, and (5) graupel.

In WSM6 (Fig. 25, row b), the largest part of the hydrometeor content is snow, but the amount is less than produced by GCE, New Thompson and Morrison. Graupel appears as a close second and is confined mainly to stronger convective cells and bands, as expected. The least column-integrated cloud water is predicted by WSM6 while the same scheme produces rather heavy cloud ice down to unexpectedly low levels, suggesting that clouds glaciate very easily in this scheme. Relative to the Lin scheme, a substantially revised approach for ice microphysical processes was provided by Hong et al. (2004) with the intent of producing more realistic cloud ice (Dudhia et al., 2008; Hong and Lim, 2006; Hong et al., 2004). While these revisions may have been intended to reduce excessive cloud ice amounts, they appear in this case to have had the opposite effect. While it is difficult to disentangle cause and effect owing to numerous microphysical and dynamical feedbacks, we note that the ice nuclei number concentration is a function of temperature in this scheme, which might lead to clouds glaciating too easily in this polar air mass.

Using the GCE scheme (Fig. 25, row c), the whole domain is dominated by snow with the maximum local snow content up to 4.50 g m^{-3} at 870 hPa. Graupel mainly appears within stronger precipitation bands. Moderate cloud water and ice are also shown in the GCE scheme.

The New Thompson scheme (Fig. 25, row d) is unique in producing essentially no cloud ice or graupel whatsoever, even in convective cells and bands. Snow dominates in the whole profile with two peaks at 875 hPa and 500 hPa, respectively. The large amount of snow in the New Thompson scheme may be due to

their snow particle size distribution function. The utilize a sum of exponential and gamma functions that produces more numerous small snow particles, which in turn reduce sedimentation and increase vapor deposition (Thompson, et al. 2008).

The Morrison 2-moment scheme (Fig. 25, row e) predicted the most column-integrated cloud water and the largest domain-averaged cloud water in the lower layers. Mainly in the convective bands and cells, substantial cloud water up to 1 g m^{-3} is produced in the lowest model layer (not shown), which includes the atmospheric layer from the surface to roughly 28 m above the surface. Such high cloud water in the lowest model layer seems unphysical, especially since the synoptic environment did not favor fog formation. The association of low-level cloud water with convective bands might be related to increased evaporation of rainfall below cloud base in convective environments (Morrison et al., 2009), though it is hard to understand how this could lead to such high cloud water amounts.

At 02 UTC 20 December 2003, moderate to heavy showers of snow pellets or small hail (WMO present weather code 88) was reported by ship "RJSY" (location shown in Fig. 19), "snow pellets" being the common term for graupel reaching the surface. Also during the five-year project "Cooperative Japan Sea Snow Cloud Project" (Murakami et al., 1994, 2003), a mixture of graupel and snow was observed in the convective snow clouds over the Sea of Japan. Supercooled water and ice also existed in the developing and mature stage of the snow clouds. In the mature stage, a large amount of the supercooled water was depleted by snow and graupel (Murakami et al., 1994, 2003). Overall, the Lin and New Thompson scheme seem to have

problem in producing snow or graupel in the environment for polar low development. It may explain their poor performance in producing realistic cloud fields. The other three schemes successfully produced a mixture of supercooled water, cloud ice, snow and graupel. However, we question the tendency of WSM6 to produce widespread cloud ice in the lower layers, likewise the tendency of Morrison to produce heavy cloud liquid water at very low altitudes.

In summary, our examination of hydrometeor concentrations yields the following assessments:

- Lin: Produces almost no snow. Graupel seems too widespread, especially in stratiform clouds.

- WSM6: Produces the least cloud liquid water and probably too much cloud ice down to low elevations. This suggests that supercooled clouds may glaciate too readily. It also produces the second-lowest snow content.

- GCE: Heaviest snow concentration; other fields seem plausible.

- Thompson: No cloud ice or graupel at any level, heavy snow concentrations over deep layer.

- Morrison: Anomalously large cloud water contents, including in lowest model layer.

5.3   Statistical comparisons

5.3.1 Spatial correlations

An additional test we undertook was the evaluation of the spatial patterns of precipitation produced by the five BMSs. For the case over the Sea of Japan in December 2003, the simulation results are compared with both the AMeDAS and UWPA products. Since there are no AMeDAS or similar data available for the other three cases, only the UWPA products are used for validation in those cases. We computed spatial correlation coefficients between the observed (UWPA and/or AMeDAS) precipitation fields and the modeled fields. For these calculations, the observations were projected onto the model grid which is at 5 km resolution. Any point without data (UWPA or AMeDAS products) was set to zero in both fields being compared. Then both the observed and simulated fields were smoothed by averaging with a 4x4 window to a resolution of 20 km.

In order to account for spatial displacement between the observed and simulated polar low center, we shifted the fields relative to one another and recorded the maximum correlation achieved for any horizontal displacement, following common practice in pattern-matching algorithms (Haralick and Shapiro, 1992; Lewis, 2003).

These spatial correlations were obtained for four polar lows, two AMSR-E overpass times each, and five BMSs. In addition, correlations with AMeDAS results are available for the two overpass times associated with the first polar low case over

the Sea of Japan. Results are given in Table 4. It can be seen that most of the cases

show good agreement with the observations, with maximum correlations up to 0.68.

In more than half of the cases, the WSM6 scheme shows the best spatial similarity

with the observations. Combining all the cases together, the WSM6 scheme presents

the maximum correlation of 0.43.

Table 4 The maximum spatial correlation between WRF simulation and observations
of precipitation patterns at 20 km resolution. Boldface values are the maximum values
achieved for a particular comparison time.

Case	Time	Validation data	BMS				
			Lin	WSM6	GCE	Thompson	Morrison
JP1	T1	UWPA	0.07	0.10	0.09	0.10	**0.13**
		AMeDAS	0.23	**0.27**	0.19	0.23	0.17
	T2	UWPA	0.45	**0.68**	0.60	0.66	0.65
		AMeDAS	0.28	**0.48**	0.34	0.46	0.46
JP2	T1	UWPA	0.55	**0.63**	0.48	0.56	0.54
	T2	UWPA	0.33	**0.38**	**0.38**	0.34	0.29
ND1	T1	UWPA	0.54	0.46	0.49	**0.57**	0.48
	T2	UWPA	0.10	**0.25**	0.19	0.22	0.08
ND2	T1	UWPA	0.54	0.51	**0.62**	0.61	0.59
	T2	UWPA	**0.54**	0.44	0.34	0.48	0.43
Combined			0.37	**0.43**	0.37	0.40	0.38

5.3.2 Domain-averaged precipitation

The domain-averaged precipitation rate over the region with the maximum

correlation is also calculated and compared with the observations (Table 5). As noted

in Section 3, the UWPA product estimates stronger precipitation rates in the strong

precipitation band and overlooks the lightest precipitation. However, the

domain-averaged precipitation rates are comparable. At 1645 UTC 19 December,

2003 in the first case over the Sea of Japan, UWPA has a mean value 0.29 mm hr^{-1}

while AMeDAS is 0.16 mm hr^{-1}. At the second observation time, UWPA has a mean value 0.32 mm hr^{-1} while AMeDAS is 0.17 mm hr^{-1}. Although the averaged precipitation rate is still higher in UPWA, a factor of 1.9 is acceptable in view of the inherent uncertainties associated with passive microwave precipitation retrievals in cold environments.

Table 5 Ratios of domain-averaged precipitation rates derived from the WRF simulations to the indicated validation data source (right-most column).

Case	Time	Validation data	Ratio of BMS results to Observation					Observation [mm hr^{-1}]
			Lin	WSM 6	GCE	Thompson	Morrison	
JP1	T1	UWPA	0.60	0.46	0.44	0.45	0.45	0.29
		AMeDAS	1.10	0.85	0.76	0.80	0.80	0.16
	T2	UWPA	0.88	0.72	0.65	0.62	0.65	0.32
		AMeDAS	1.41	1.06	0.84	0.95	0.98	0.17
JP2	T1	UWPA	0.73	0.58	0.58	0.56	0.55	0.38
	T2	UWPA	0.76	0.56	0.53	0.51	0.53	0.32
ND1	T1	UWPA	6.82	4.12	3.93	4.00	3.97	0.02
	T2	UWPA	2.45	2.06	2.08	2.06	1.95	0.03
ND2	T1	UWPA	2.63	2.43	1.58	1.96	2.13	0.04
	T2	UWPA	7.76	7.07	5.29	7.10	6.98	0.01

Over the Sea of Japan, the domain-averaged precipitation rates in the observations are of the order of 0.1 mm hr^{-1} (Table 5). The ratio of simulation to observation ranges from 0.4 to 1.5. The simulations are thus not inconsistent with the observations when one allows for about a factor of two uncertainty in the latter.

However, over the Nordic Sea, the observed domain-averaged precipitation rates are of the order of 0.01 mm hr^{-1}, which is considerably below that produced by the simulations. Especially for the second Nordic Sea case at 1120 UTC 05 December 2003, the ratio of all the simulations to the UWPA is greater than five. In all these

cases, the Lin scheme predicted the largest averaged precipitation rate. In most cases, the WSM6 gives the second-largest amount. The other three schemes had similar but slightly lower values in most of the cases. Note that both polar low cases occurred within about one degree latitude of Jan Mayen Island, where our three-year comparison of UWPA estimates with gauge amounts (Fig. 2) revealed a modest overestimate of monthly totals by the satellite product. It therefore cannot simply be assumed that the UWPA was biased low by a factor of five in these particular cases, though it also cannot be ruled out.

5.4 Summary and discussion

In this chapter, we investigated the influence of five mixed-phase BMSs on simulations of four spiraliform polar lows. The purpose was to identify the BMS that is likely to be most suitable for subsequent model-based investigations of the role of moist processes in the dynamics of polar low development.

It was found that the choice of BMS did not have much effect on the location of the polar low development. However, the simulated CTT and precipitation fields were quite different. It is our assessment that the Lin and New Thompson schemes did not yield cloud fields that were qualitatively consistent with the observed CTT.

The primary hydrometeor in the Lin scheme is graupel while snow is the predominant component in the other BMSs. Consistent with a local ship weather report as well as in situ field observations of convective snow clouds over the Sea of

Japan (Murakami et al., 1994, 2003), mixed snow and graupel with small amount of super cooled water were predicted in the WSM6, GCE and Morrison 2-moment schemes. Based on the maximum correlation between the modeled and observed precipitation rates, all simulations were deemed to produce fairly reasonable spatial patterns of precipitation, though the details clearly differed from one scheme to the next. Overall, the WSM6 scheme yielded the best overall spatial/temporal correlation with the observed precipitation fields.

The domain-averaged precipitation rates were computed around the regions of polar lows. It was shown that the Lin scheme consistently has the largest average precipitation rate. The WSM6 scheme is the second-largest in most of the cases while other BMSs produced lighter precipitation. The observed precipitation over the Sea of Japan is an order of magnitude higher than those over the Nordic Sea. Over the Sea of Japan, the WRF model produced precipitation intensities comparable to the observations. However, over the Nordic Sea, much higher precipitation rates were modeled than were estimated via satellite, especially at the time that only very light precipitation was observed. While it is known that microwave retrievals can have difficulty detecting high latitude precipitation, the UWPA product is notable for slightly overestimating monthly surface gauge totals at the same latitude throughout most of the three-year period 2003-2005 (Fig. 2).

The difference in apparent model performance between the Sea of Japan and Nordic Sea could be due to three reasons. First, the UWPA product is likely to overlook the lightest precipitation. Over the Nordic Sea, it is colder and less moist

than over the Sea of Japan. Also the two cases over Nordic Sea are shallower than the cases over Sea of Japan. Most of the precipitation intensity is smaller than 2 mm hr^{-1} which may be below the detection threshold of the UWPA algorithm when precipitation reaches the surface as snow. If very little precipitation occurred at higher rates, then the UWPA would not detect the majority of the total precipitation that fell. Second, the initialization data over the Nordic Sea may be less reliable on account of the sparseness of surface data. The third reason may be that the BMSs simply do not simulate this kind of cold shallow precipitation well at high latitudes.

Table 6 summarizes our comparison results. The WSM6 scheme showed reasonable results for CTT, maximum precipitation and spatial correlation. It also produced plausible combinations of cloud water, cloud ice, snow and graupel. But there might be some question concerning its production of widespread cloud ice in the lower layers. Notwithstanding the unavoidable ambiguities, our assessment based on both subjective and objective criteria is that the WSM6 scheme is marginally superior to the others in reproducing cloud and precipitation processes overall. High quality surface and in situ aircraft cloud physical measurements would be required in order to give greater confidence to this finding. Unfortunately, such data are not readily available over the regions where most polar lows form.

Table 6 Summary of assessments. A check mark ($\sqrt{}$) indicates 'satisfactory' performance, with caveats noted where applicable.

	CTT	Maximum precipitation rate	Best precipitation spatial correlation	Hydrometeor fields
Lin		$\sqrt{}$		
WSM6	$\sqrt{}$	$\sqrt{}$	$\sqrt{}$	$\sqrt{}$ - too much cloud ice?
GCE	$\sqrt{}$			$\sqrt{}$
Thompson				
Morrison	$\sqrt{}$			$\sqrt{}$ – too much cloud liquid water?

Chapter 6 Potential Vorticity Inversion Diagnosis of the Development of Polar Lows

6.1 Definition and inversion procedure

The Ertel potential vorticity (EPV; Rossby, 1940; Ertel, 1942) is defined as

$$q = \frac{1}{\rho} \eta \cdot \nabla \theta \tag{1}$$

where ρ is the density, η is the absolute vorticity vector, and θ is the potential temperature. The conservation of EPV is not depended on any scaling assumption. In fact, a high-order balance approximation can be used for the inversion of EPV even in situations where the Rossby number is not small (Davis and Emanuel, 1991). The Davis and Emanuel (1991) (DE) method is used in this study to investigate the development process of polar lows. The Charney (1955) balance condition, which retains accuracy in highly curved flows, is used in the DE method. Assuming 1) hydrostatic balance and 2) that the magnitude of the irrotational component of the wind is much smaller than the magnitude of the nondivergent component (ie., $|\mathbf{V}_x| \ll |\mathbf{V}_\psi|$), the divergence equation and (1) can be rewritten as:

$$\nabla^2 \Phi = \nabla \cdot (f \nabla \psi) + \frac{2}{a^4 \cos^2 \phi} \frac{\partial \left(\frac{\partial \psi}{\partial \lambda}, \frac{\partial \psi}{\partial \phi} \right)}{\partial (\lambda, \phi)} \tag{2}$$

$$q = \frac{g \kappa \pi}{P} \left[(f + \nabla^2 \psi) \frac{\partial^2 \Phi}{\partial \pi^2} - \frac{1}{a^2 \cos^2 \phi} \frac{\partial^2 \psi}{\partial \lambda \partial \pi} \frac{\partial^2 \Phi}{\partial \lambda \partial \pi} - \frac{1}{a^2} \frac{\partial^2 \psi}{\partial \phi \partial \pi} \frac{\partial^2 \Phi}{\partial \phi \partial \pi} \right] \tag{3}$$

where Φ is the geopotential, ψ is the nondivergent streamfunction, λ is

the longitude, ϕ is the latitude, a is the radius of the earth, $\kappa = R/c_p$, P is the

pressure, and $\pi = \left[c_p \left(P/P_0 \right)^\kappa \right]$ is the Exner function, which serves as the vertical

coordinate. The boundary conditions used in this method are Dirichlet conditions for

ψ and Φ on the lateral boundaries and Neumann conditions $\dfrac{\partial \Phi}{\partial \pi} = f_0 \dfrac{\partial \psi}{\partial \pi} = -\theta$ on

horizontal boundaries.

The PV fields are calculated from the model's wind and temperature fields at

all vertical levels over grid 1. The potential temperature at 975 hPa and 75 hPa

(linearly interpolated between 1000 and 950 hPa and 50 and 100 hPa, respectively)

provides the Neumann boundary conditions on the horizontal boundaries. To insure

convergence of the iterative method used to invert the PV, negative values of PV are

set to a small positive constant value (0.01 PVU). Given these distributions of PV,

balance condition and boundary conditions, a full inversion is performed to solve for

the geopotential, Φ, and the nondivergent streamfunction, ψ, associated with the

total PV fields. Details of the numerical methods and boundary conditions appear in

DE.

A piecewise PV inversion method is also presented in DE in order to recover

the flow fields associated with discrete PV anomalies. The total PV fields are

partitioned into mean and discrete perturbation fields. The discrete portions of the

perturbation PV fields are inverted individually to determine the balanced

perturbation geopotential height and streamfunction associated with the discrete PV

anomalies.

For the Sea of Japan case in December 2003, the time mean field which is used to define the perturbation PV fields is computed from three-consecutive 42-h simulations; one initialized at 00 UTC 17 December 2003, the object run initialed at 18 UTC 18 December 2003, and another initialized at 12 UTC 20 December 2003. For the Nordic Sea case in January 2003, the time mean field which is used to define the perturbation PV fields is computed from three-consecutive 36-h simulations; one initialized at 18 UTC 14 January 2003, the object run initialized at 06 UTC 16 January 2003, and another initialized at 18 UTC 17 January 2003. The time mean is then subtracted from the instantaneous PV distribution at each discrete time in the object run to get the perturbation fields.

Although the partitioning of the PV fields is arbitrary, a minimum number of pieces of PV which are associated with the most important PV anomalies are necessary for the effective interpretation of partitioning. Most of the significant PV anomalies in the troposphere and lower stratosphere are included in two parts: the PV anomalies near the tropopause and boundary temperature anomalies near the surface. Except the PV anomalies which are associated with diabatic processes, the PV anomalies are generally small and nonsystematic within the middle and lower troposphere and the lower stratosphere (Morgan and Nielsen-Gammon, 1998).

As in the studies of Korner and Martin (2000), Martin and Marsili (2002), and Martin and Otkin (2004), a conventional three-way partitioning is used here. The total perturbation PV field is partitioned into an upper layer, an interior layer, and a surface layer. The upper layer extends from 650 hPa to 50 hPa and is designed to isolate PV

anomalies near the tropopause. As stratospheric air is likely to be quite dry, the positive perturbation PV in this layer is set to 0.0 PVU whenever the relative humidity is greater than 70%. The interior layer extends from 950 hPa to 400 hPa and is intended to isolate mid-troposphere PV anomalies associated with LHR. Since such LHR will occur in an environment at or near saturation, the PV in this layer is set to 0.0 PVU whenever the relative humidity is less than 70%. This guards against the scheme mistaking extruded stratospheric perturbation PV for perturbation PV contributed by LHR. The surface layer extends from 950 to 900 hPa and also includes the 975-hPa potential temperature. This layer is designed to isolate the boundary potential temperature anomalies that are equivalent to PV anomalies just above the surface (Bretherton, 1966). The surface layer, however, also includes perturbation PV in the 950-900-hPa layer. To ensure against redundancy with the interior layer, surface layer perturbation PV from 950 hPa to 900 hPa is set to 0.0 PVU whenever the relative humidity is greater than 70%.

The combination of these three layers and their respective relative humidity criteria excludes only two parts of the total perturbation PV distribution from being inverted; namely, 1) positive perturbation PV in air with relative humidity greater than 70% in the 350-50-hPa layer, and 2) perturbation PV in air with relative humidity less than 70% in the 850-600-hPa layer. Careful scrutiny of the data, however, revealed that these portions of the total perturbation PV distributions were very small in the present cases. For the remainder of the paper, U_{pert} will refer to the PV perturbations associated with the upper layer, M_{pert} to perturbations associated with the interior layer,

and L_{pert} to perturbations associated with the surface layer.

6.2 Evaluation of inversion results

Once the inversion is performed, the effect of each of the three pieces of the perturbation PV on the lower-tropospheric height changes during the lifecycle of the polar low is considered. Since the lowest available isobaric surface in the inversion output was 950 hPa, subsequent analysis will concentrate on the evolution of geopotential height at that level.

Figure 26 compares the 950-hPa geopotential height between the simulation and full inversion field at 00 UTC 20 December. The full inversion field (Fig. 26b) captures a geopotential height pattern similar to that produced in the simulation field (Fig. 26a), with three low centers shown in both the model and full inversion fields. Figure 26c shows the difference in the geopotential heights between the full inversion and model height fields. The difference is small in most of the region, including where the polar low is located (Fig. 26c). As expected, relatively large differences are shown in the vicinity of the upper-level trough axis where the balanced condition is most likely to be violated. Figure 27 is a time series of geopotential heights at the center of the polar low. Note that the full inversion height agrees well with the model heights at most of the forecast times. Additionally, the full inversion and the sum of the partitioned PV pieces are fairly close to one another, indicating that the piecewise partitioning scheme accounts for most parts of the total perturbation PV and associated perturbation heights. Given these similarities, we confidently employ the

results of the piecewise PV inversion to diagnose the development of the polar low.
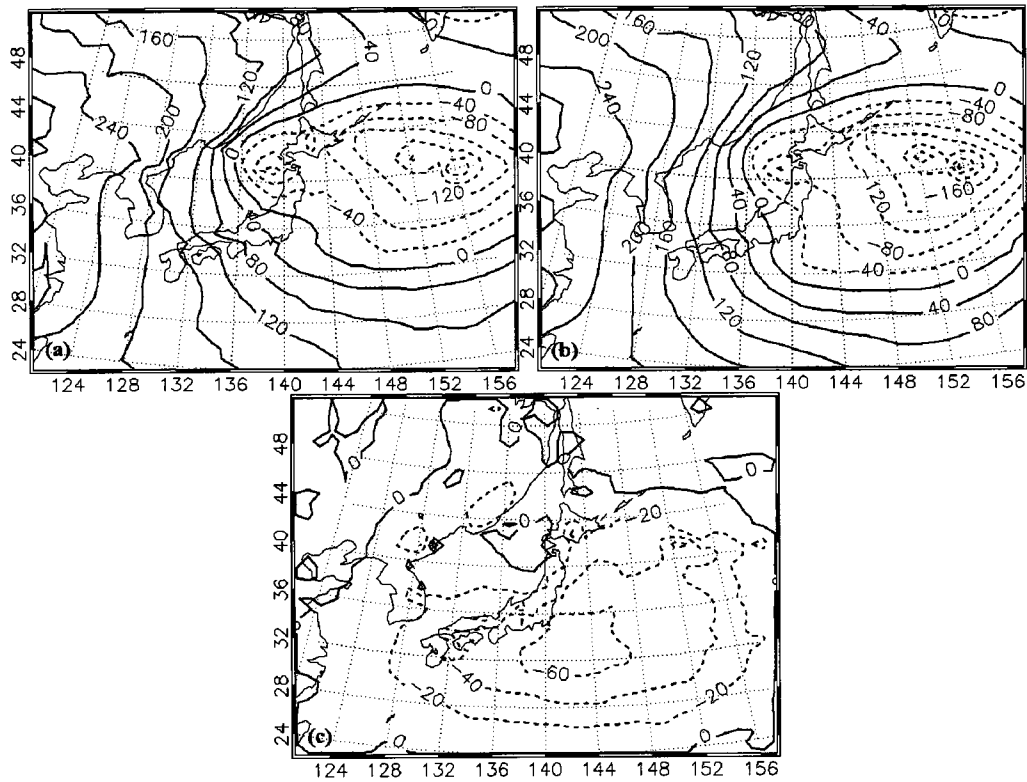
FIG. 26 (a) The WRF 950-hPa geopotential height contoured every 40 m. (b) The full inverted geopotential height contoured every 40 m. (c) The difference between the WRF field and full inverted field contoured every 20 m. All the fields are validated at 00 UTC 20 December 2003.
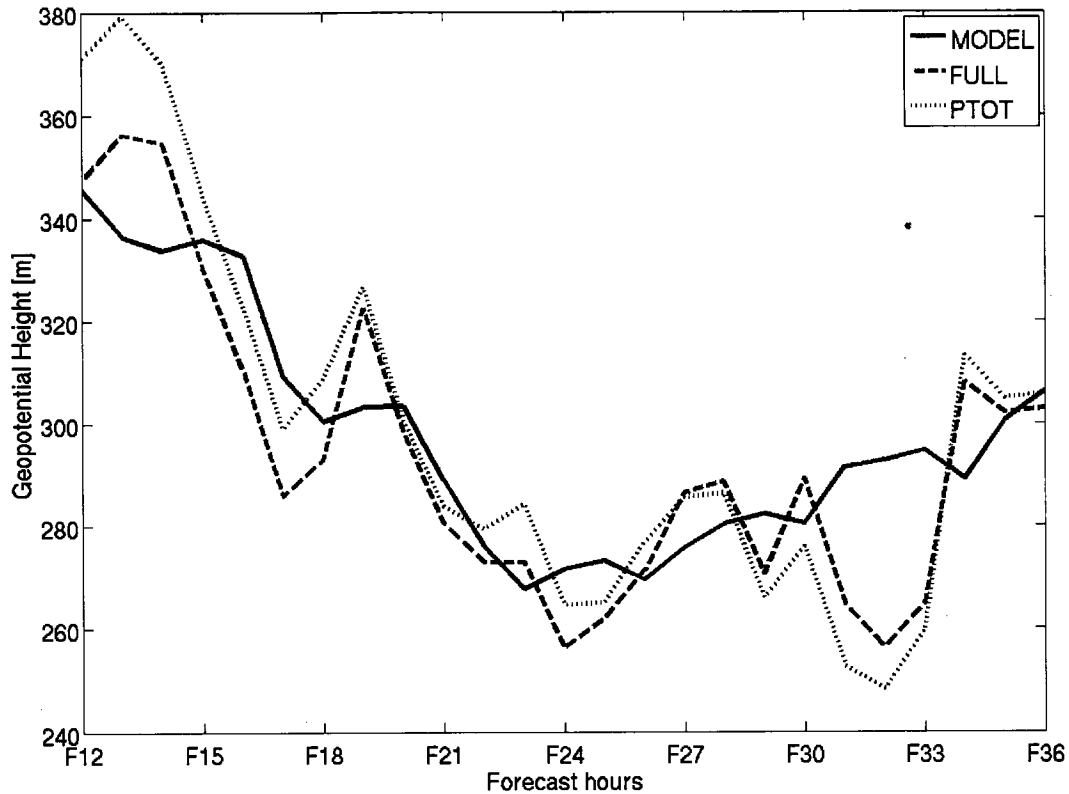
FIG. 27 Time series of geopotential heights at the center of the polar low: WRF simulation (solid line), full inversion (dash line) and summation of piecewise PV inversion (dotted line).

6.3   A case study over the Sea of Japan

6.3.1   Partitioned height changes

Figure 28 shows the 950-hPa height perturbation associated with the U_{pert} PV anomaly at 12-h intervals from 18 UTC 18 December to 06 UTC 20 December. The position of the 950-hPa polar low center from the full inversion is indicated by the star symbol for times at which the polar low center is clearly identified. At 18 UTC 18 December (Fig. 28a), the center of the U_{pert} PV anomaly was located over the Eurasian continent with a minimum height perturbation of −119 m at 950 hPa. A

negative height perturbation (of about −40 m) contributed by the U_{pert} PV anomaly was seen over the northern Sea of Japan, where the polar low later developed. At 06 UTC 19 December (Fig. 28b), the minimum height perturbation associated with the U_{pert} PV anomaly was just moving off the Eurasian continent. A significant deepening of its associated height perturbation was seen during the 12-h period as the minimum height perturbation deepened by 99 meters. The polar low center was located to the northeast of the minimum height perturbation associated with the U_{pert} PV anomaly. In the next 12-h period (Fig. 28c), the height perturbation continued to deepen. The polar low center was just north of, and closer to, the minimum height perturbation associated with the U_{pert} PV anomaly. By 06 UTC 20 December (Fig. 28d), the height perturbation associated with the U_{pert} PV anomaly had weakened while moving to southeast of the polar low center.

FIG. 28 The 950-hPa geopotential height perturbation associated with the Upert PV anomaly. Negative (positive) geopotential height perturbations are indicated by dashed (solid) lines labeled in m and contoured every 40 m. The star indicates the location of the polar low center at each time. Valid at (a) 18 UTC 18 December; (b) 06 UTC 19 December; (c) 18 UTC 19 December; (d) 06 UTC 20 December.

Weak positive height perturbations associated with the M_{pert} PV anomaly were seen over the Sea of Japan at 18 UTC 18 December (Fig. 29a). At the same time, a weak negative height perturbation, presumably associated with the cloud shield of extratropical cyclone A shown in Fig. 3a, was seen to the east of the Japan. During the next 12 hours, the positive height anomaly over the Sea of Japan strengthened and weak negative height perturbations associated with the cloud head of developing cyclone B (shown in Fig. 7) were evident (Fig. 29b). Although the polar low was characterized by positive M_{pert} height perturbations, a narrow trough of low M_{pert} heights can be seen extending northward from cyclone B across Hokkaido and into

the vicinity of the polar low. The center of the M_{pert} positive height perturbation had weakened by 18 UTC 19 December as it slid southward across the Sea of Japan (Fig. 29c). Simultaneously, the negative M_{pert} height perturbation associated with the cloud head of cyclone B intensified substantially while an axis of weak negative M_{pert} height perturbation extended over the polar low region. In the next several hours, the negative M_{pert} height perturbation continued to intensify. As the polar low moved over land, moderate precipitation occurred near the western coast of Japan (Fig. 30). The negative height perturbation contributed by LHR reached its minimum of -73 meters over the polar low center at 02 UTC 20 December (not shown), after which time the effect of LHR associated with the polar low started to weaken. By 06 UTC 20 December (Fig. 29d), negative height anomalies were still apparent in the vicinity of the polar low while continued intensification of cyclone B was evident in the even more substantial negative M_{pert} heights along its developing warm front at this time.
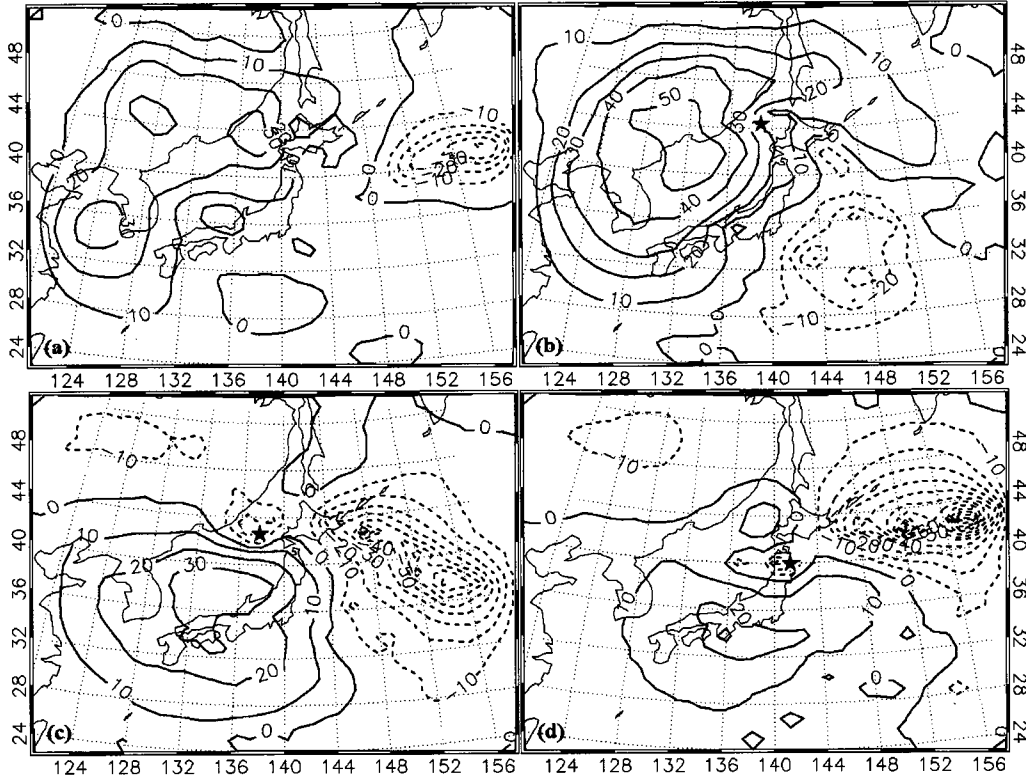
FIG. 29 The 950-hPa geopotential height perturbation associated with the M_{pert} PV anomaly. Negative (positive) geopotential height perturbations are indicated by dashed (solid) lines labeled in m and contoured every 10 m. The star indicates the location of the polar low center at each time. Valid at (a) 18 UTC 18 December; (b) 06 UTC 19 December; (c) 18 UTC 19 December; (d) 06 UTC 20 December.
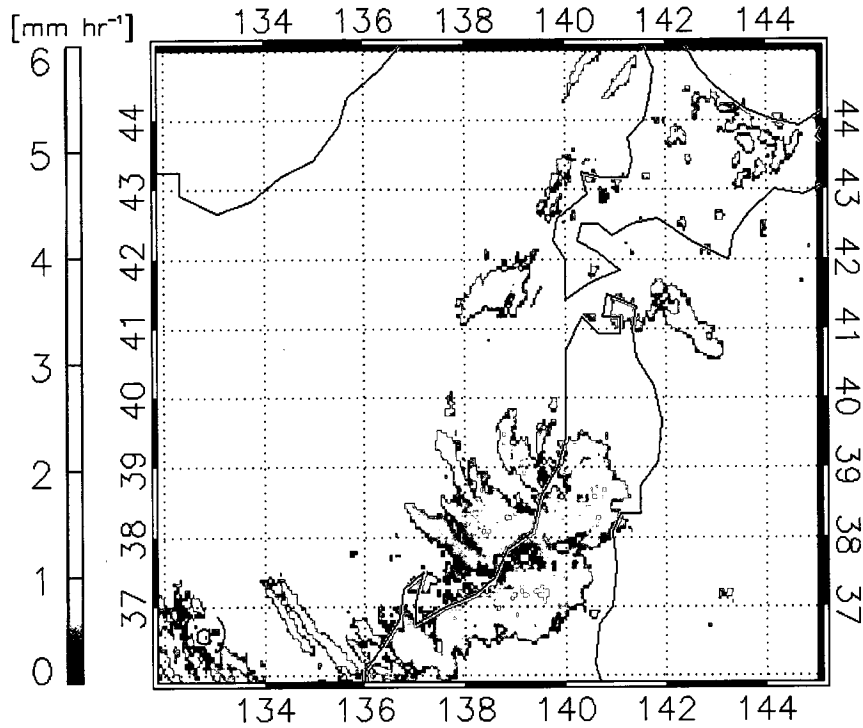
FIG. 30 The precipitation rate from AMeDAS radar product shows the polar low brought extensive precipitation over Japan. Valid at 0350 UTC 20 Dec 2003.

For height perturbations associated with the L_{pert} PV anomaly (Fig. 31), positive (negative) height perturbations are associated with negative (positive) temperature anomalies. Throughout the entire analysis period, positive (negative) height perturbations dominated the western (eastern) part of the domain. Though the positive height perturbations steadily weakened over time, the negative height perturbations steadily strengthened. Also a counterclockwise rotation of the dipole of positive and negative height perturbations can be seen throughout this time period. At 18 UTC 18 December (Fig. 31a), most of the Sea of Japan was dominated by a cold anomaly though a weak negative height anomaly is hinted at over Hokkaido. By 06 UTC 19 December (Fig. 31b), a modest negative height perturbation can be seen in the vicinity of the polar low with a strong L_{pert} height gradient to the west and

southwest. During the next 12 hours, though the gradient of the L_{pert} height perturbations around the polar low continued increasing, the center of the polar low moved toward positive height perturbations (Fig. 31c). The polar low region was totally covered by positive L_{pert} height perturbations by 06 UTC 20 December (Fig. 31d) while the gradient of the height perturbations around the polar low had also weakened significantly.
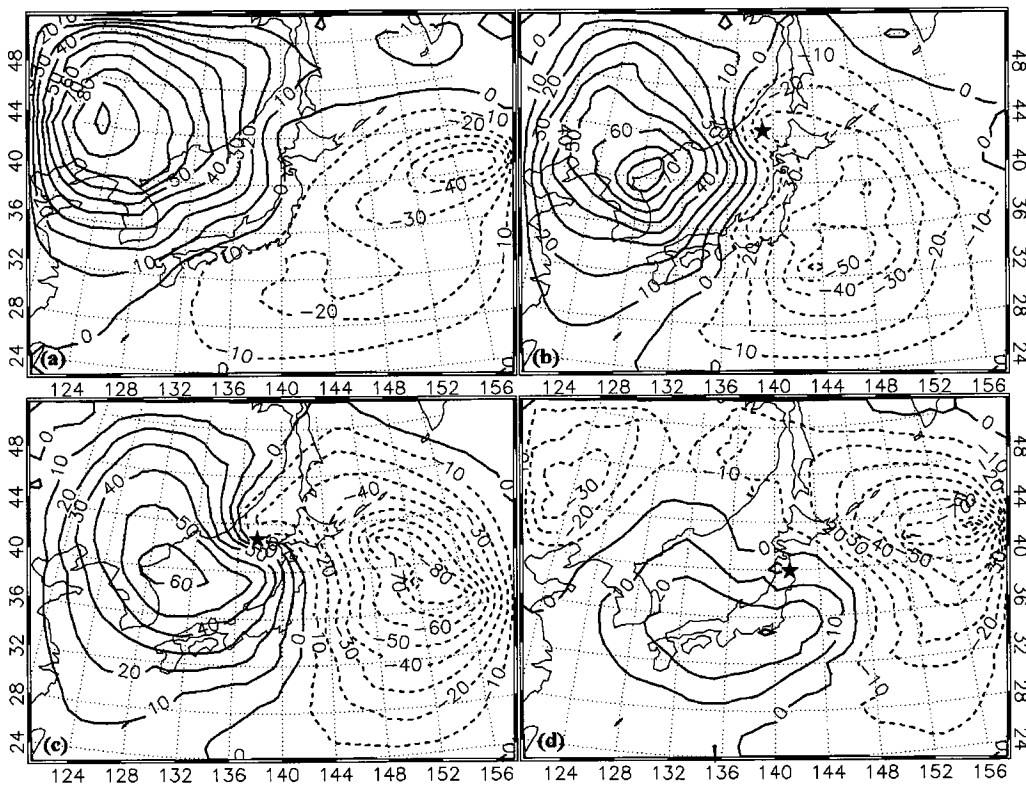
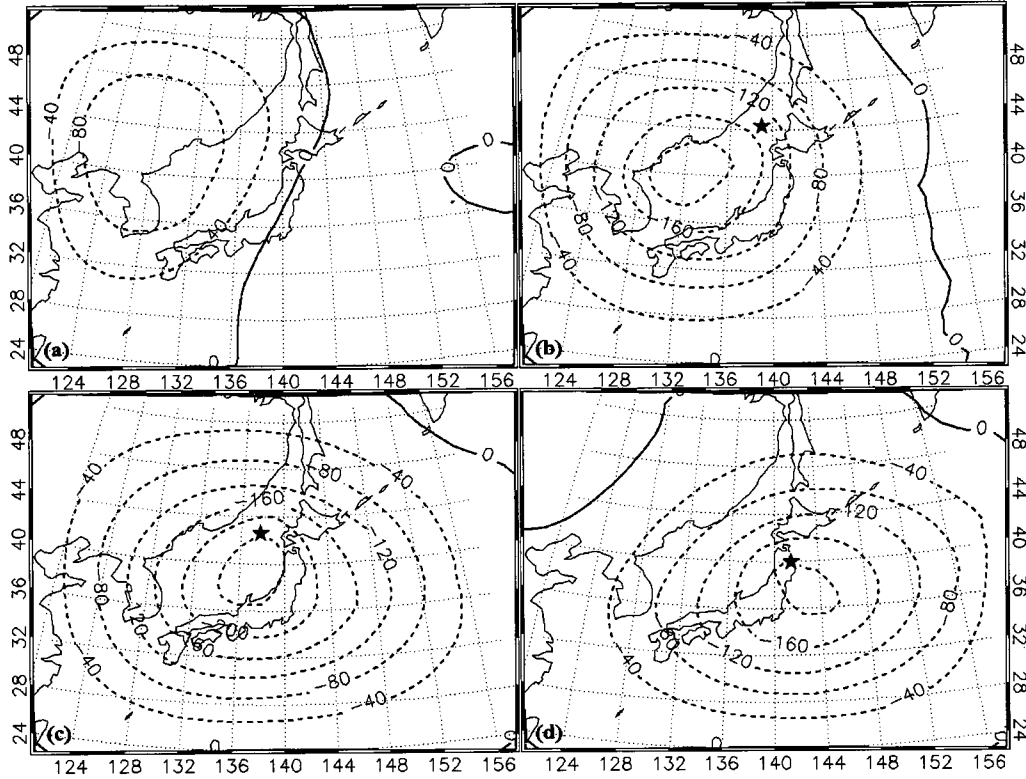
FIG. 31 The 950-hPa geopotential height perturbation associated with the Lpert PV anomaly. Negative (positive) geopotential height perturbations are indicated by dashed (solid) lines labeled in m and contoured every 10 m. The star indicates the location of the polar low center at each time. Valid at (a) 18 UTC 18 December; (b) 06 UTC 19 December; (c) 18 UTC 19 December; (d) 06 UTC 20 December.

Figure 32 shows the 3-hourly evolution of the 950-hPa geopotential height change at the polar low center during the development phase of the polar low. The tendency and magnitude of the full inversion height changes agree well with the model data at most times except the forecast time period F30-33 (Fig. 32a).

As shown in Fig. 32b, the U_{pert} PV anomaly contributed substantially to the 950-hPa height tendency at the polar low center throughout the entire lifecycle. From F15 to F18, the upper-level PV anomaly was the primary contributor to the development of the polar low (Fig. 32b). The positive near-surface temperature anomaly contributed secondarily while a positive height change was associated with the M_{pert} PV anomaly. From F18 to F24, the upper-level PV anomaly and the M_{pert} PV anomaly associated with LHR contributed nearly equally; counteracting positive height changes contributed by the L_{pert} PV anomaly from F18 to F21. From F24 to F27, there were no significant height changes contributed by the U_{pert} and L_{pert} PV anomalies while positive height perturbations were contributed by the M_{pert} PV anomaly. In the 6 hours between F27 and F33, the M_{pert} PV anomaly contributed to deepening the polar low, while the U_{pert} and L_{pert} PV anomalies contributed modest weakening. This trend was continued through F33-F36 during which time the U_{pert} PV anomaly made the primary contribution to decay of the polar low while the M_{pert} PV anomaly contributed secondarily.

3-h Total Perturbation Height Changes vs Model Height Changes

3-h Total Perturbation Height Changes and
Discrete Perturbation Height Changes
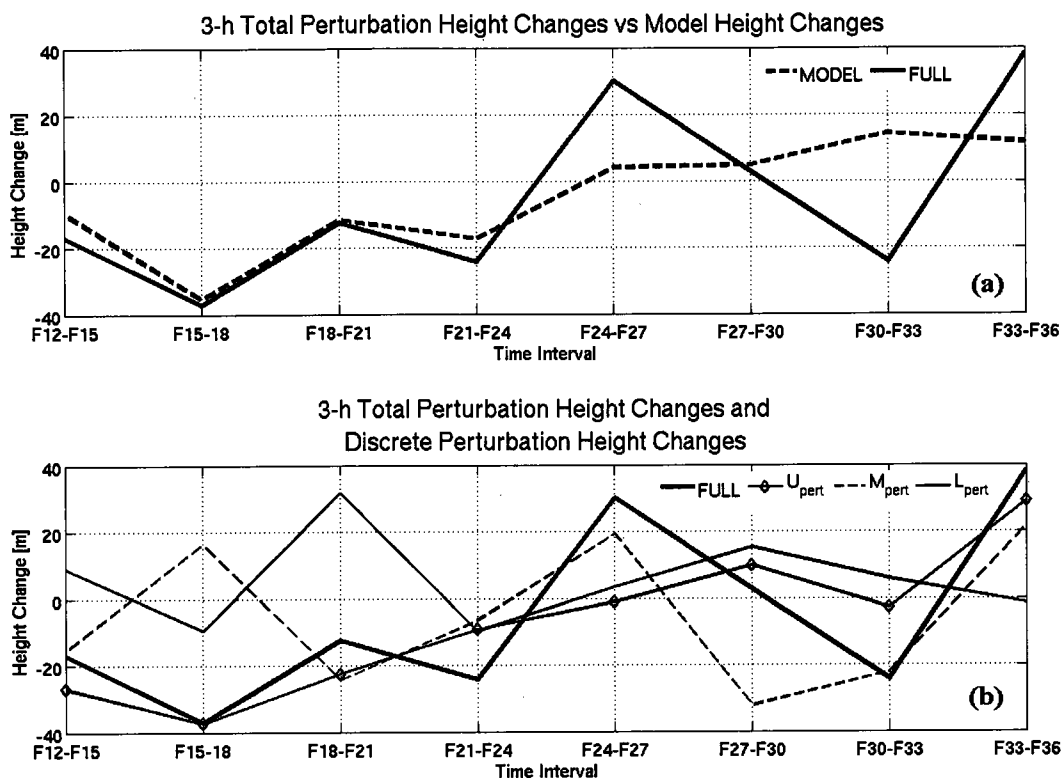
FIG. 32 (a) The 3-hourly height changes at the 950-hPa center of polar low from the WRF outputs (dash line) and the full inversions (solid line). (b) The 3-hourly height changes at the 950-hPa center of polar low from the full inversions (thick solid line) and the perturbation heights associated with the U_{pert} (thin solid line with diamond), M_{pert} (thin dash line) and L_{pert} (thin solid line) PV anomalies. Valid for the case over the Sea of Japan in December 2003.

6.3.2 Physical factors influencing the U_{pert} and M_{pert} PV anomalies

As shown in the preceding section, the U_{pert} PV anomaly contributed most substantially to the development of the polar low. The effect of a tropopause-level PV anomaly on lower-tropospheric heights is dependent on the scale, magnitude, and shape of the anomaly and is modulated by the intervening stratification (Hoskins et al. 1985). Figure 33 shows the PV at 350 hPa superimposed upon its associated 950-hPa U_{pert} height perturbation. The maximum PV values at 350 hPa are listed in Table 7. In

the first 12 hours, the maximum U_{pert} PV decreased slightly from 6.47 PVU to 6.38

PVU. Then it increased to 6.91 PVU by 18 UTC 19 December. By 06 UTC 20

December, the maximum U_{pert} PV had, again, decreased slightly to 6.74 PVU.
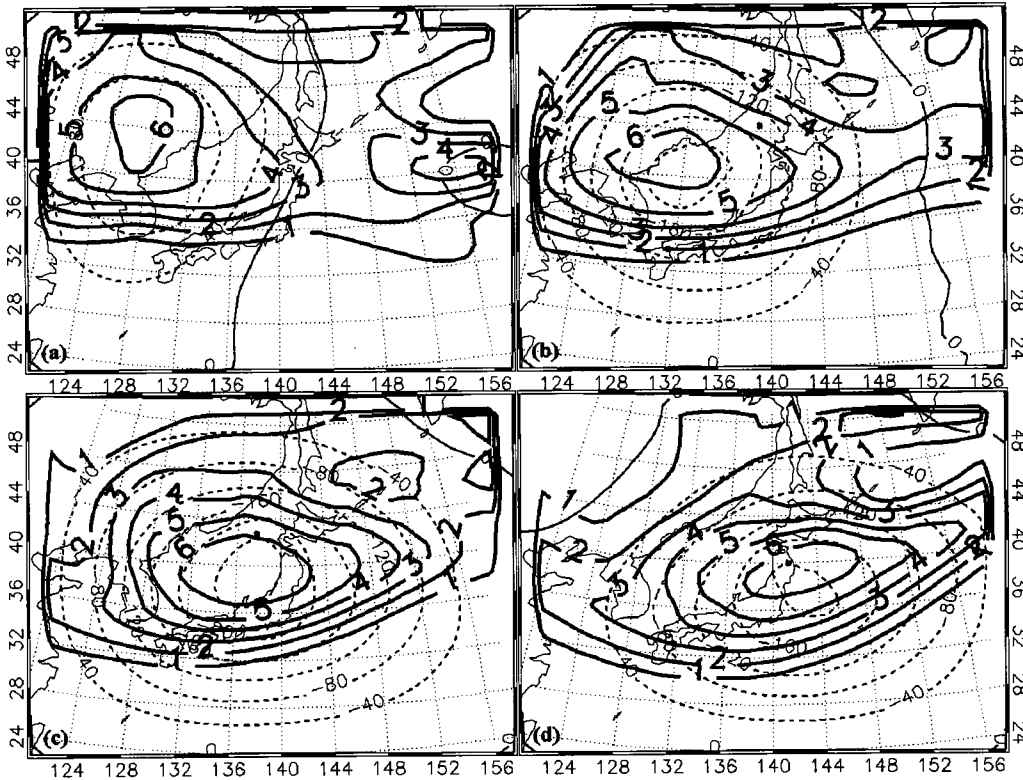
FIG. 33 As for Fig. 28 but with 350 hPa perturbation PV superimposed. Valid at (a) 18
UTC 18 December; (b) 06 UTC 19 December; (c) 18 UTC 19 December; (d) 06 UTC
20 December.

Table 7 The maximum EPV at 350 hPa; the 950-hPa and 350-hPa perturbation height
associated with U_{pert}, their ratio and the Brunt-Väisällä frequency (BVF) at the
950-hPa perturbation height minimum column at each time.

Time	Max EPV at 350 hPa (PVU)	950 hPa [m]	350 hPa [m]	Ratio	BVF [10^{-4} s^{-1}]
18/18Z	6.47	−119	−185	0.64	3.73
19/06Z	6.38	−218	−315	0.69	3.34
19/18Z	6.91	−265	−355	0.75	3.50
20/06Z	6.74	−208	−254	0.81	3.77

When a PV anomaly is more isotropic (anisotropic), the perturbation heights associated with it are more intense (weaker) (Morgan and Nielsen-Gammon, 1998; Martin and Marsili, 2002). A thinning and elongation of the U_{pert} PV was seen from 18 UTC 19 December to 06 UTC 20 December (Fig. 33c and Fig. 33d), which contributed to the tendency for weakening of the perturbation heights associated with the U_{pert} PV anomaly.

The largest perturbation geopotential height contributed by the U_{pert} PV anomaly was, at each time, found at 350 hPa. Thus, the ratio of the 950 to 350-hPa perturbation height in the column containing the 950-hPa perturbation height minimum can be used to assess the changes in the penetration depth of the U_{pert} PV anomaly. From Table 7, the ratio increased steadily from 0.64 at 18 UTC 18 December to 0.81 at 06 UTC 20 December. Coincident with these changes, the Brunt-Väisällä frequency (N) at this column decreased significantly (from 3.73×10^{-4} s^{-1} to 3.34×10^{-4} s^{-1}) at the first 12 h and increased modestly (3.50×10^{-4} s^{-1}) in the subsequent 12 h. By 06 UTC 20 December, the Brunt-Väisällä frequency (N) increased substantially to 3.77×10^{-4} s^{-1}.

Thus, the rapid 950-hPa U_{pert} height falls in the first 12 hours were primarily due to the migration of U_{pert} PV anomaly over the ocean, where the penetration depth was increased via a reduction in the lower tropospheric static stability. At 06 UTC 20 December, the decrease of the U_{pert} perturbation height at 950 hPa resulted from both the weakening and the thinning and elongation of the U_{pert} PV perturbation.

As is the case in extratropical cyclones, LHR further enhanced the

development of the polar low in two ways. First, LHR reduced the effective static stability. The Brunt-Väisällä frequency (N) at the polar low center gradually decreased from 3.66×10^{-4} s^{-1} at 06 UTC 19 December to 3.59×10^{-4} s^{-1} at 18 UTC 19 December, and further to 3.43×10^{-4} s^{-1} at 06 UTC 20 December. Second, as shown in Fig. 29, the diabatically generated PV anomaly was associated with a negative geopotential height perturbation in the lower troposphere, which directly contributed to the intensification of the surface cyclone.

Based on the preceding analysis, the development processes of the polar low can be summarized as follows. Prior to the development of the polar low, the positive PV anomaly near the tropopause was over the Eurasian continent, moving southeastward toward the central Sea of Japan. Near the surface, a weak positive temperature anomaly over the northern Sea of Japan (near Hokkaido) was generated by warm air advection forced by the winds associated with the U_{pert} PV anomaly. When the U_{pert} PV anomaly moved over the Sea of Japan, where the static stability was considerably lower, the negative height perturbation associated with the U_{pert} PV anomaly intensified substantially which, in turn, assisted in the intensification of the surface temperature anomaly. The combined effects of the height perturbation associated with the U_{pert} and L_{pert} PV anomalies instigated development of the polar low. This development was characterized by an outbreak of convection near the low center. The M_{pert} PV anomaly contributed by LHR initially enhanced the development of the polar low by superposing an additional negative height perturbation in the lower troposphere. The development process of this polar low agrees well with the

two stage development proposed by Montgomery and Farrell (1992). Additional insights shown from this case include: 1) the U_{pert} PV anomaly contributed significantly throughout the polar low lifecycle, including developing and decaying stages; 2) the dissipation of the polar low was primarily forced by the weakening of the contribution from the U_{pert} PV anomaly.

6.4   One case over the Nordic Sea

For the case over the Nordic Sea in January 2003, Figure 34 shows the 950-hPa height perturbation associated with the U_{pert} PV anomaly at 6-h intervals from 12 UTC 16 January to 06 UTC 17 January. At 12 UTC 16 January (Fig. 34a), weak negative height perturbations associated with the U_{pert} PV anomaly covered the Scandinavian Peninsula. To the west of the Norwegian coast, a negative height perturbation center associate with the U_{pert} PV anomaly was seen near the ridge of 1000-500 hPa thickness in Fig. 11a. In the next 6 hours, the negative height perturbations contributed by the U_{pert} PV anomaly moved slightly southeastward with a reduction in its magnitude (Fig. 34b). The negative height perturbations over the ocean significantly weakened although the polar low center was first indicated on the map. The weakening of the negative height perturbations associated with the U_{pert} PV anomaly continued during the next 6 hours with the polar low center shown near the border of the negative height perturbations (Fig. 34c). By 06 UTC 17 January, the polar low region was entirely covered by positive height perturbations associated with

U_{pert} PV anomaly (Fig. 34d).
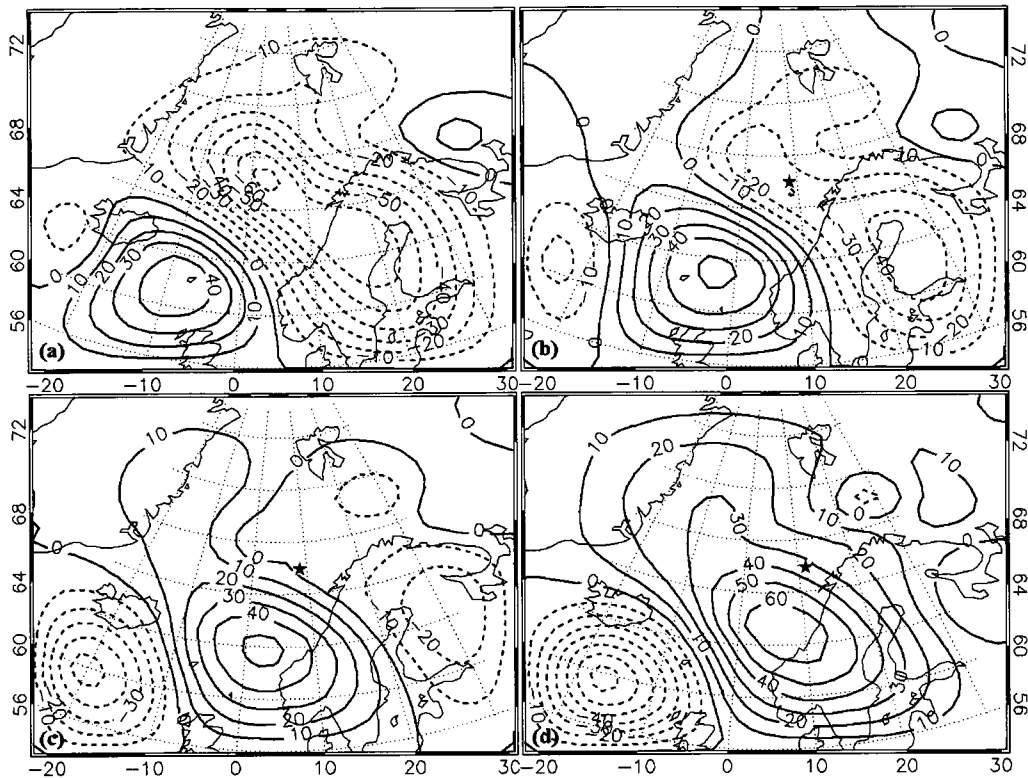
Fig. 34 The 950-hPa geopotential height perturbation associated with the U_{pert} PV anomaly. Negative (positive) geopotential height perturbations are indicated by dashed (solid) lines labeled in m and contoured every 10 m. The star indicates the location of the polar low center at each time. Valid at (a) 12 UTC 16 January; (b) 18 UTC 16 January; (c) 00 UTC 17 January; (d) 06 UTC 17 January.

At 12 UTC 16 January, although the Norwegian Sea was mostly covered by positive height perturbations associated with the M_{pert} PV anomaly, a local minimum can be seen over the region where polar low was developed later (Fig. 35a). In the next 6 hours, the positive height perturbation associated with the M_{pert} PV anomaly moved southeastward while the local minimum contributed by the LHR-generated PV anomaly slightly intensified (Fig. 35b). By 00 UTC 17 January, most of the positive height perturbations associated with the M_{pert} PV anomaly moved over land while the negative height perturbations contributed by the LHR-generated PV anomaly were

seen in the vicinity of the polar low (Fig. 35c). At 06 UTC 17 January, the polar low

has merged with cyclone B labeled in Fig. 14. Intense negative height perturbations

contributed by the LHR-generated PV anomaly were associated with cyclone B (Fig.

35d).
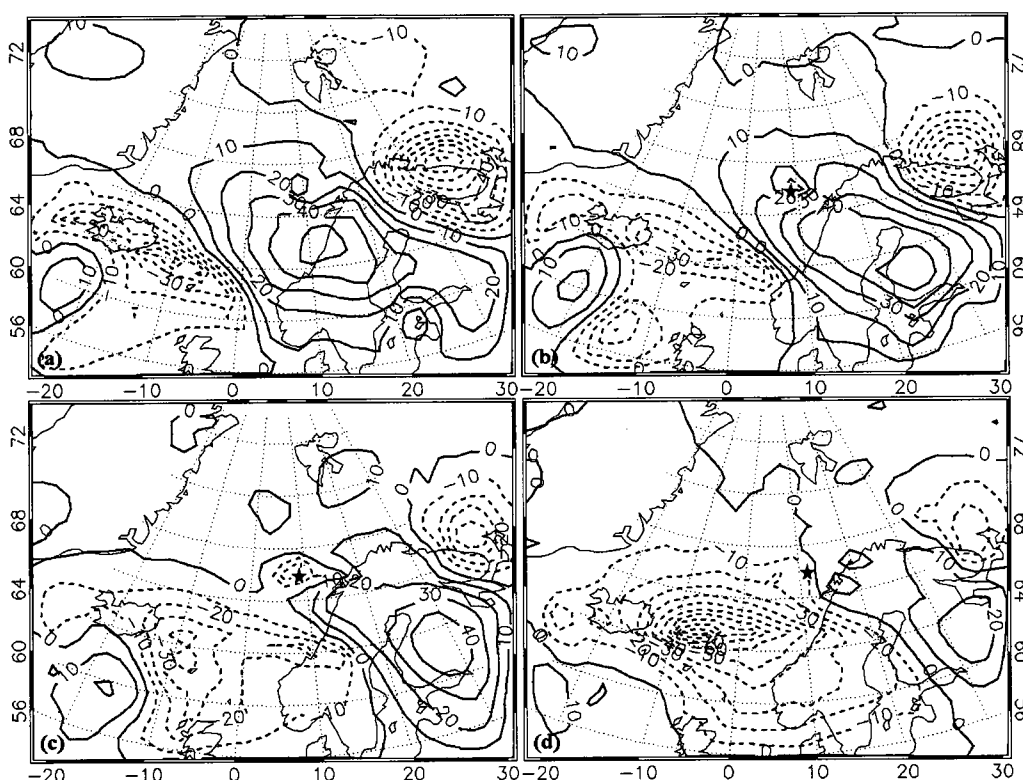
FIG. 35 The 950-hPa geopotential height perturbation associated with the M_{pert} PV anomaly. Negative (positive) geopotential height perturbations are indicated by dashed (solid) lines labeled in m and contoured every 10 m. The star indicates the location of the polar low center at each time. Valid at (a) 12 UTC 16 January; (b) 18 UTC 16 January; (c) 00 UTC 17 January; (d) 06 UTC 17 January.

Although positive height perturbations contributed by a low-level cold

anomaly dominated the Norwegian Sea at 12 UTC 16 January, weak negative height

perturbations were seen near 72°N 10°E (Fig. 36a). Negative height perturbations

associated with the L_{pert} PV anomaly were also seen over the North Atlantic, Barents

Sea and the Scandinavia Peninsula. The center of the polar low was seen in the

positive height perturbations associated with the L$_{pert}$ PV anomaly at 18 UTC 16

January. Over time, positive height perturbations gradually moved southeastward and

weakened while the vicinity of the polar low was covered by negative height

perturbations (Fig. 36c and Fig. 36d). By 06 UTC 17 January, all the regions over

ocean were fully covered by negative height perturbations associated with the L$_{pert}$ PV

anomaly (Fig. 36d).
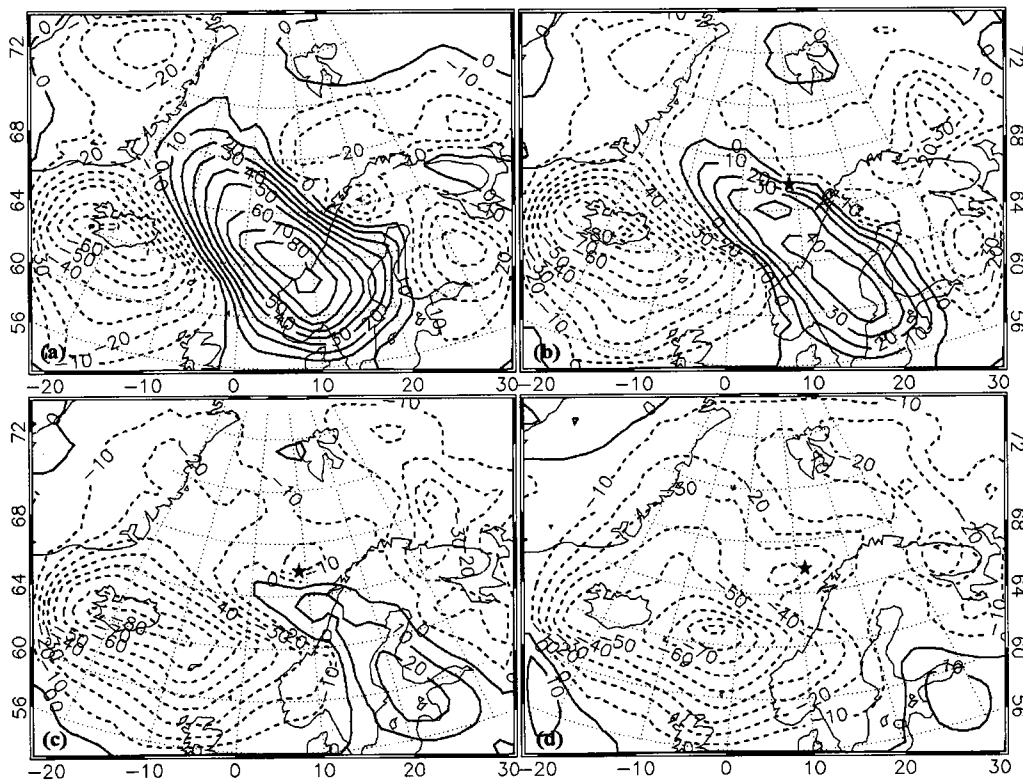
FIG. 36 The 950-hPa geopotential height perturbation associated with the L$_{pert}$ PV
anomaly. Negative (positive) geopotential height perturbations are indicated by
dashed (solid) lines labeled in m and contoured every 10 m. The star indicates the
location of the polar low center at each time. Valid at (a) 12 UTC 16 January; (b) 18
UTC 16 January; (c) 00 UTC 17 January; (d) 06 UTC 17 January.

Figure 37 shows the 3-hourly evolution of the 950-hPa geopotential height

changes at the polar low center during the development of the polar low. In sharp

contrast to the case over the Sea of Japan, the main developmental processes of the

polar low over the Nordic Sea were contributed by the L$_{pert}$ PV anomaly while the

U$_{pert}$ PV anomaly contributed positive height changes for the whole time periods (Fig.

37b). The M$_{pert}$ PV anomaly contributed primarily in the F15-F18 time period. Similar

to the case over the Sea of Japan, the decay of the polar low was primarily forced by

the U$_{pert}$ PV anomaly.
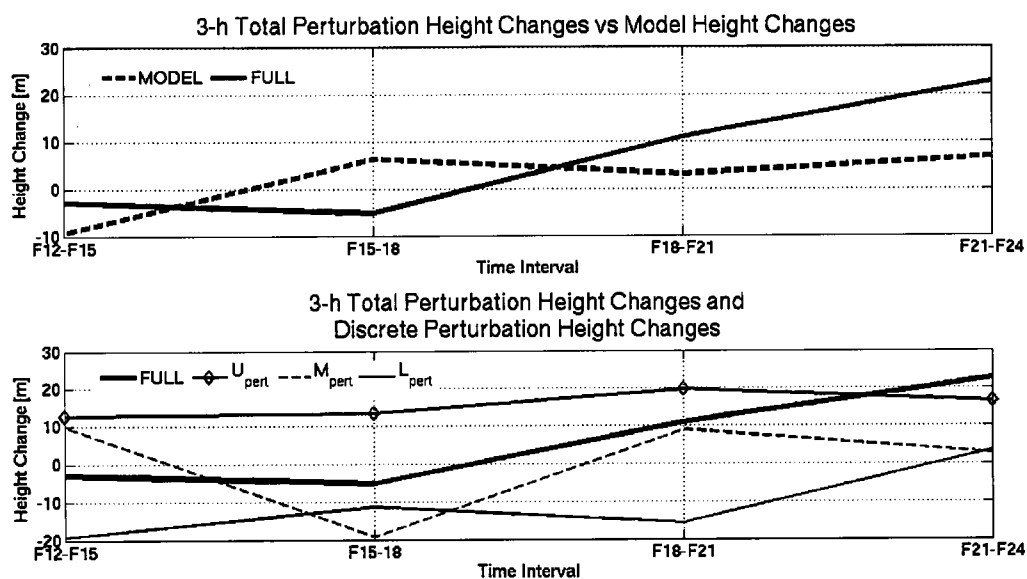
FIG. 37 (a) The 3-hourly height changes at the 950-hPa center of polar low from the
WRF outputs (dash line) and the full inversions (solid line). (b) The 3-hourly height
changes at the 950-hPa center of polar low from the full inversions (thick solid line)
and the perturbation heights associated with the U$_{pert}$ (thin solid line with diamond),
M$_{pert}$ (thin dash line) and L$_{pert}$ (thin solid line) PV anomalies. Valid for the case over
Nordic Sea in January 2003.

The preceding analysis suggested that the polar low was stimulated when the

upper-level PV anomaly approached the surface warm anomaly region. The

development of the polar low was mainly contributed by the L$_{pert}$ PV anomaly which

was forced by strong low-level warming due to intense air-sea interactions over the

warm tongue of sea surface. In the first couple of hours, the development of the polar

low was enhanced by the LHR-generated PV anomaly associated with cloud and

precipitation processes. The elongation of the upper-level PV anomaly persistently weakened its effect on the lower troposphere, which in turn led to the rapid decay of the polar low.

6.5   Summary and discussion

The piecewise PV inversion method of Davis and Emanuel (1991) was used in this chapter to diagnose the development processes of two polar lows, one over the Sea of Japan and one over the Nordic Sea. It was shown that the PV inversion method successfully accounts for the synoptic development of polar lows. The total perturbation PV field was partitioned into three layers designed to isolate PV anomalies at the tropopause (U_{pert}), those associated with LHR (M_{pert}), and those associated with lower boundary temperature anomalies (L_{pert}), respectively. The piecewise PV inversion results clearly demonstrated the effect and relative importance of these discrete PV anomalies on the development of the two polar lows.

For the case over the Sea of Japan, the effect of the upper-level positive PV anomaly on the circulation in the lower troposphere intensified when the positive PV anomaly near the tropopause moved southeastward toward the Sea of Japan, where the lower troposphere was less stably stratified. A weak positive temperature anomaly was generated over the northern Sea of Japan as surface cyclogenesis and associated warm air advection began to the east of Japan. As the U_{pert} PV anomaly moved over the Sea of Japan and closer to the surface positive temperature anomaly, the effect of

the U_{pert} PV anomaly on lower tropospheric heights intensified significantly primarily due to a reduction of the lower tropospheric static stability. Thus, the interaction of the U_{pert} PV anomaly and the surface warm anomaly induced the development of the polar low over the Sea of Japan.

During the development of the polar low, LHR associated with cloud and precipitation processes reduced the effective static stability and superposed a negative height perturbation in the lower troposphere. At the same time, the effect of the U_{pert} PV anomaly made a contribution equal to that produced by LHR.

When the polar low moved toward land, extensive precipitation developed over the western coast of Japan. LHR associated with the precipitation contributed to further deepening of the polar low. Subsequently, the combined effect of the weakening and the thinning and elongation of the U_{pert} PV anomaly decreased the effect of the U_{pert} PV on the lower tropospheric geopotential heights. As a consequence, the polar low quickly dissipated.

For the case over the Nordic Sea, an upper-level PV anomaly was also seen during the development of the polar low. The formation of the polar low was stimulated by the approach of the upper-level PV anomaly to the surface positive temperature anomaly. Similar to the case over the Sea of Japan, the development of the polar low was enhanced by the LHR-generated PV anomaly. However, in sharp contrast to the case over the Sea of Japan, the development of the polar low was mainly a result of the L_{pert} PV anomaly contributed by the strong air-sea interaction over the warm tongue of sea surface. In the meanwhile, the U_{pert} PV anomaly

persistently weakened the polar low.

Similar to other studies, the two polar lows were initiated when an upper-level PV anomaly approached a surface positive temperature anomaly. The LHR-generated PV anomaly intensified the development of the polar lows at the developing stage.

Thus, for the case over the Sea of Japan, the development (decay) of the polar low was accompanied with the intensification (weakening) of the U_{pert} effect on the lower troposphere. However, for the case over the Nordic Sea, the effect of the U_{pert} PV anomaly on the lower troposphere weakened gradually during the entire development of the polar low. In association with the weakening of the U_{pert} PV anomaly, the polar low also quickly dissipated. It is suggested that the U_{pert} PV anomaly is a necessary condition to support the further development of polar lows. The shorter lifecycle of the case over the Nordic Sea may be an artifact of the U_{pert} PV anomalies inability to support its further development. Furthermore, the air-sea interaction which leads to the boundary temperature anomaly is more important for the polar low case over the Nordic Sea while its effect is smaller in the case over the Sea of Japan.

Chapter 7 Conclusions and Future Perspectives

Lack of data has always been the major problem of polar low studies in the high latitude regions. The new high resolution numerical models with good parameterizations of physical processes have proved to be very effective for simulating the structure and development of mesoscale systems, such as polar lows in data sparse regions. With the unprecedented availability over the past decade of high-resolution satellite infrared and passive microwave observations of surface wind, precipitation, and other variables, it is now feasible to directly observe the evolution and structure of polar lows and to assess the realism of model simulations of these storms. New insights into polar low development can be obtained from the combined observational/modeling study. A state-of-the-art mesoscale weather prediction system, known as the WRF model, was used in this study to investigate the development process of polar lows. The satellite, radar and in situ observations were used to assess the realism of model simulations of these storms.

In this study, we first investigated the influence of five mixed-phase BMSs on simulations of four spiraliform polar lows. The purpose was to identify the BMS that is likely to be most suitable for subsequent model-based investigations of the role of moist processes in the dynamics of polar low development.

It was found that the choice of BMS did not have much effect on the location of the polar low development. However, the simulated CTT and precipitation fields

were quite different. It is our assessment that the Lin and New Thompson schemes did not yield cloud fields that were qualitatively consistent with the observed CTT.

The primary hydrometeor in the Lin scheme was graupel while snow was the predominant component in the other BMSs. Consistent with a local ship weather report as well as in situ field observations of convective snow clouds over the Sea of Japan (Murakami et al., 1994, 2003), mixed snow and graupel with small amount of super cooled water were predicted in the WSM6, GCE and Morrison 2-moment schemes. Based on the maximum correlation between the modeled and observed precipitation rates, all simulations were deemed to produce fairly reasonable spatial patterns of precipitation, though the details clearly differed from one scheme to the next. Overall, the WSM6 scheme yielded the best overall spatial/temporal correlation with the observed precipitation fields.

The domain-averaged precipitation rates were computed around the regions of polar lows. It was shown that the Lin scheme consistently had the largest average precipitation rate. The WSM6 scheme was the second-largest in most of the cases while other BMSs produced lighter precipitation. The observed precipitation over the Sea of Japan was an order of magnitude higher than those over the Nordic Sea. Over the Sea of Japan, the WRF model produced precipitation intensities comparable to the observations. However, over the Nordic Sea, much higher precipitation rates were modeled than were estimated via satellite, especially at the time that only very light precipitation was observed. While it was known that microwave retrievals can have difficulty detecting high latitude precipitation, the UWPA product was notable for

slightly overestimating monthly surface gauge totals at the same latitude throughout most of the three-year period 2003-2005 (Fig. 2).

The difference in apparent model performance between the Sea of Japan and Nordic Sea could be due to three reasons. First, the UWPA product is likely to overlook the lightest precipitation. Over the Nordic Sea, it is colder and less moist than over the Sea of Japan. Also the two cases over Nordic Sea are shallower than the cases over Sea of Japan. Most of the precipitation intensity is smaller than 2 mm hr^{-1} which may be below the detection threshold of the UWPA algorithm when precipitation reaches the surface as snow. If very little precipitation occurred at higher rates, then the UWPA would not detect the majority of the total precipitation that fell. Second, the initialization data over the Nordic Sea may be less reliable on account of the sparseness of surface data. The third reason may be that the BMSs simply do not simulate this kind of cold shallow precipitation well at high latitudes.

The WSM6 scheme showed reasonable results for CTT, maximum precipitation and spatial correlation. It also produced plausible combinations of cloud water, cloud ice, snow and graupel. But there might be some question concerning its production of widespread cloud ice in the lower layers. Notwithstanding the unavoidable ambiguities, our assessment based on both subjective and objective criteria is that the WSM6 scheme is marginally superior to the others in reproducing cloud and precipitation processes overall. High quality surface and in situ aircraft cloud physical measurements would be required in order to give greater confidence to this finding. Unfortunately, such data are not readily available over the regions where

most polar lows form.

After the performance of different BMSs was evaluated, the development processes of two polar lows, one over the Sea of Japan and one over the Nordic Sea, were diagnosed with the piecewise PV inversion method. The PV inversion method successfully accounted for the synoptic development of polar lows. The total perturbation PV field was partitioned into three layers designed to isolate PV anomalies at the tropopause (U_{pert}), those associated with LHR (M_{pert}), and those associated with lower boundary temperature anomalies (L_{pert}), respectively. The piecewise PV inversion results clearly demonstrated the effect and relative importance of these discrete PV anomalies on the development of the two polar lows.

It was shown that, antecedent to the development of the polar low over the Sea of Japan in December 2003, a positive lower-tropospheric temperature anomaly was induced by the approach of a positive tropopause-level PV anomaly over the northern Sea of Japan. The analysis suggested that the polar low was initiated as a result of the combined effect of the positive PV anomaly near the tropopause and the near-surface positive temperature anomaly. The rapid height falls in the lower troposphere were primarily contributed by the upper tropospheric PV anomaly. Further intensification of the polar low was contributed by LHR associated with cloud and precipitation processes. After the polar low moved over northern Honshu, quick dissipation was primarily rendered by the combined effects of the weakening and the thinning and elongation of the upper level PV anomaly that led to a rapid reduction of lower troposphere height perturbations associated with the upper level PV anomaly.

For the case over the Nordic Sea, an upper-level PV anomaly was also seen during the development of the polar low. The formation of the polar low was stimulated by the approach of the upper-level PV anomaly to the surface positive temperature anomaly. Similar to the case over the Sea of Japan, the development of the polar low was enhanced by the LHR-generated PV anomaly. However, in sharp contrast to the case over the Sea of Japan, the development of the polar low was mainly a result of the L_{pert} PV anomaly contributed by the strong air-sea interaction over the warm tongue of sea surface. In the meanwhile, the U_{pert} PV anomaly persistently weakened the polar low.

Similar to other studies, the two polar lows were initiated when an upper-level PV anomaly approached a surface positive temperature anomaly. The LHR-generated PV anomaly intensified the development of the polar lows at the developing stage.

Thus, for the case over the Sea of Japan, the development (decay) of the polar low was accompanied with the intensification (weakening) of the U_{pert} effect on the lower troposphere. However, for the case over the Nordic Sea, the effect of the U_{pert} PV anomaly on the lower troposphere weakened gradually during the entire development of the polar low. In association with the weakening of the U_{pert} PV anomaly, the polar low also quickly dissipated. It is suggested that the U_{pert} PV anomaly is a necessary condition to support the further development of polar lows. The shorter lifecycle of the case over the Nordic Sea may be an artifact of the U_{pert} PV anomalies inability to support its further development. Furthermore, the air-sea interaction which leads to the boundary temperature anomaly is more important for

the polar low case over the Nordic Sea while its effect is smaller in the case over the Sea of Japan.

This study confirms that piecewise PV inversion is a useful tool for examining the dynamics of polar low formation. With this method, new insights into the effect of discrete PV anomalies on the development of polar lows can be obtained. The relative importance of discrete PV anomalies on the development of polar lows is clearly demonstrated from the piecewise PV inversion method. As shown in other studies (eg., Davis et al., 1993; Stoelinga, 1996; Posselt and Martin, 2004), the direct and indirect effect of discrete PV anomalies (contributed by LHR, surface friction, etc.) on the development of polar lows can also be inferred. More polar low cases, with different synoptic environments, will be investigated with the piecewise PV inversion method. It is hoped that the results of these analyses will add important detail to the conceptual and physical model of the development of polar lows.

As a source of cloud condensation nuclei (CCN), aerosol pollutants have a considerable impact on cloud microphysics and precipitation processes (Lohmann and Feicheter, 2005). Although there is still great uncertainty, two likely indirect effects of aerosols have been proposed for the low-level liquid clouds. The first indirect effect is that the load of aerosol will increase the cloud droplet number concentration and decrease the average cloud droplet size for a fixed liquid water content (Twomey, 1977). The second one is that the raindrop development will be suppressed by loaded aerosols since the collision efficiency is weaker for smaller droplets. A decrease in precipitation efficiency and extension of the cloud lifetime will be rendered by this

effect (Albrecht, 1989; Ramanathan et al., 2001). While most research was focused on the effect of aerosols on liquid clouds, the relationship between aerosols and ice clouds is still largely unknown (Penner et al., 2001). In the future, I will investigate the effect of aerosols on the cloud and precipitation processes of polar lows. Further influence on the development of polar lows will also be studied.

References

Adler, R. F., C. Kidd, G. Petty, M. Morissey, and H. M. Goodman, 2001: Intercomparison of Global Precipitation Products: The Third Precipitation Intercomparison Project (PIP–3). Bull. Amer. Meteor. Soc., 82, 1377–1396.

Albrecht, B. A., 1989: Aerosols, cloud microphysics, and fractional cloudiness, Science, 245, 1227–1230.

Baum, B. A. and S. Platnick, 2006: Introduction to MODIS cloud products. Earth Science Satellite Remote Sensing, Vol. 1: Science and instruments. J. J. Qu, W. Gao, M. Kafatos, R. E. Murphy, and V. V. Salomonson, Eds, Co-published by Tsinghua University Press and Springer-Verlag, 74-91.

Bond, N. A. and Shapiro, M. A., 1991: Polar Lows over the Gulf of Alaska in Conditions of Reverse Shear. Mon. Wea. Rev. 119, 551-572.

Bracegirdle, T. J. and S. L. Gray, 2009: The dynamics of a polar low assessed using potential vorticity inversion. Quart. J. Roy. Meteorol. Soc., 135, 880-893.

Bresch, J. F., R. J. Reed, and M. D. Albright, 1997: A Polar-Low Development over the Bering Sea: Analysis, Numerical Simulation, and Sensitivity Experiments. Mon. Wea. Rev., 125, 3109–3130.

Bretherton F. P., 1966: Baroclinic instability and the shortwave cutoff in terms of potential vorticity. Quart. J. Roy. Meteor. Soc., 92, 335–345.

Bromwich, D. H., K. M. Hines, and L.-S. Bai, 2009: Development and Testing of Polar Weather Research and Forecasting Model: 2. Arctic Ocean. J. Geophys. Res., 114, D08122, doi:10.1029/2008JD010300.

Carlton, A.M. and Song, Y.D., 2000: Satellite Passive Sensing of the Marine Atmosphere Associated With Cold-Air Mesoscale Cyclones. Professional Geographer, 52(2), 289-306.

Charney J., 1955: The use of the primitive and balance equations. Tellus, 7, 22–26.

Chen, S.-H., and W.-Y. Sun, 2002: A one-dimensional time dependent cloud model. J. Meteor. Soc. Japan, 80, 99–118.

Claud C., N. M. Mognard, K. B. Katsaros, A. Chedin, and N. A. Scott, 1993: Satellite observations of a polar low over the Norwegian Sea by SSM/I, Geosat and TOVS. J. Geophys. Res., 98, 14487-14506.

Davis, C. A. and K. A. Emanuel, 1991: Potential vorticity diagnostics of cyclogenesis. Mon. Wea. Rev., 119, 1929–1953.

Davis, C. A., M. T. Stoelinga, and Y.-H. Kuo, 1993: The integrated effect of condensation in numerical simulations of extratropical cyclogenesis. Mon. Wea. Rev., 121, 2309–2330.

Douglas, M.W., L. Fedor, and M. Shapiro, 1991: Polar Low Structure over the Northern Gulf of Alaska Based on Research Aircraft Observations. Mon. Wea. Rev., 119, 32–54.

Douglas, M.W., M. Shapiro, L. Fedor, and L. Saukkonen, 1995: Research Aircraft Observations of a Polar Low at the East Greenland Ice Edge. Mon. Wea. Rev., 123, 5-15.

Dudhia, J., 1989: Numerical study of convection observed during the winter monsoon experiment using a mesoscale two-dimensional model. J. Atmos. Sci., 46, 3077–3107.

Dudhia, J., S.-Y. Hong, and K.-S. Lim, 2008: A new method for representing mixed-phase particle fall speeds in bulk microphysics parameterizations. J. Meteor. Soc. Japan, 86A, 33-44.

Emanuel, K. A. and R. Rotunno, 1989: Polar lows as arctic hurricanes. Tellus, 41A, 1–17.

Ertel H., 1942: Ein Neuer hydrodynamischer Wirbelsatz. Meteor. Z., 59, 271–281.

Espy, J. P., 1841: *The Philosophy of Storms*. Little-Brown, 552 pp.

Forsythe J. M., and T. H. Vonder Haar, 1996: A warm core in a polar low observed with a satellite microwave sounding unit. Tellus, 48A, 193-208.

Gallus Jr., W. A. and Pfeifer, M., 2008: Intercomparison of simulations using 5 WRF microphysical schemes with dual-Polarization data for a German squall line. Adv. Geosci., 16, 109–116.

Grønås, S., A. Foss, and M. Lystad, 1987: Numerical simulations of polar lows over the Norwegian Sea. Tellus, 39A, 334-353.

Grønås, S., and N. G. Kvamstø, 1995: Numerical simulations of the synoptic conditions and development of Arctic outbreak polar lows. Tellus, 47A, 797–814.

Guo, J. T., G. Fu, Z. L. Li, L. M. Shao, Y. H. Duan and J. G. Wang, 2007: Analyses and numerical modeling of a polar low over the Japan Sea on 19 December 2003. Atmos. Res., 85(3-4), 395-412.

Haralick, R. M., and L. G. Shapiro, 1992: Computer and Robot Vision. Vol. II, Addison-Wesley, 316–317.

Harrold T. W., and K. A. Browning, 1969: The polar low as a baroclinic disturbance. Quart. J. Roy. Meteor. Soc, 95, 710–723.

Hong, S.-Y., J. Dudhia, and S.-H. Chen, 2004: A Revised Approach to Ice Microphysical Processes for the Bulk Parameterization of Clouds and Precipitation, Mon. Wea. Rev., 132, 103–120.

Hong, S.-Y. and J.-O. J. Lim, 2006: The WRF Single-Moment 6-Class Microphysics Scheme (WSM6), J. Korean Meteor. Soc., 42, 129–151.

Hong. S.-Y., Y. Noh, and J. Dudhia, 2006: A new vertical diffusion package with an explicit treatment of entrainment processes. Mon. Wea. Rev., 134, 2318–2341.

Hoskins B. J., I. Draghici, and H. C. Davies, 1978: A new look at the ω-equation. Quart. J. Roy. Meteor. Soc., 104, 31–38.

Kain, J. S., and J. M. Fritsch, 1990: A one-dimensional entraining/detraining plume model and its application in convective parameterization. J. Atmos. Sci., 47, 2784–2802.

Kain, J. S., and J. M. Fritsch, 1993: Convective parameterization for mesoscale models: The Kain–Fritsch scheme. The Representation of Cumulus Convection in Numerical Models, Meteor. Monogr., No. 46, Amer. Meteor. Soc., 165–170.

Kessler, E., 1969: On the Distribution and Continuity of Water Substance in Atmospheric Circulations. Meteor. Monogr., No. 32, Amer. Meteor. Soc., 84 pp.

Korner S., and J. E. Martin, 2000: Piecewise frontogenesis from a potential vorticity perspective: Methodology and a case study. Mon. Wea. Rev., 128, 1266–1288.

Lohmann, U., and J. Feichter, 2005: Global indirect aerosol effects: A review. Atmos. Chem. Phys., 4, 7561– 7614.

Lewis, J. P. , cited 2003: Fast Normalized Cross-Correlation. [Aailable online at

http://www.idiom.com/~zilla/Papers/nvisionInterface/nip.html]

Lin, Y.-L., R. D. Farley, and H. D. Orville, 1983: Bulk parameterization of the snow field in a cloud model. J. Climate Appl. Meteor., 22, 1065–1092.

Makihara, Y., N. Uekiyo, A. Tabata, and Y. Abe, 1996: Accuracy of Radar-AMeDAS precipitation. IEICE Trans. Commun., E79-B, 751–762.

Mansfield, D. A., 1974: Polar lows: The development of baroclinic disturbances in cold air outbreaks. Quart. J. Roy. Meteor. Soc., 100, 541–554.

Martin J. E., and N. Marsili, 2002: Surface cyclolysis in the North Pacific Ocean. Part II: Piecewise potential vorticity diagnosis of a rapid cyclolysis event. Mon. Wea. Rev., 130, 1264–1281.

Martin J. E., and J. A. Otkin, 2004: The Rapid Growth and Decay of an Extratropical Cyclone over the Central Pacific Ocean. Wea. Forecasting, 19, 358–376.

Martin, R. and G. W. Moore, 2006: Transition of a synoptic system to a polar low via interaction with the orography of Greenland. Tellus A, 58(2), 236–253.

Meyers, M. P., R. L. Walko, J. Y. Harrington, and W. R. Cotton, 1997: New RAMS cloud microphysics parameterization. Part II: The two-moment scheme. Atmos. Res., 45, 3-39.

Mlawer, E. J., S. J. Taubman, P. D. Brown, M. J. Iacono, and S. A. Clough, 1997: Radiative transfer for inhomogeneous atmosphere: RRTM, a validated correlated-k model for the longwave. J. Geophys. Res., 102 (D14), 16663–16682.

Montgomery, M. T., and B. F. Farrell, 1992: Polar low dynamics. J. Atmos. Sci., 49, 2484–2505.

Moore, R.W., and T.H. Vonder Haar, 2003: Diagnosis of a Polar Low Warm Core Utilizing the Advanced Microwave Sounding Unit. Weather Forecast, 18, 700–711.

Morgan M. C., and J. Nielsen-Gammon, 1998: Using tropopause maps to diagnose midlatitude weather systems. Mon. Wea. Rev., 126, 2555–2579.

Morrison H., J. A. Curry, and V. I. Khvorostyanov, 2005: A new double-moment microphysics parameterization for application in cloud and climate models. Part I: Description. J. Atmos. Sci., 62, 1665–1677.

Morrison H., and J. O. Pinto, 2006: Intercomparison of Bulk Cloud Microphysics

Schemes in Mesoscale Simulations of Springtime Arctic Mixed-Phase Stratiform Clouds. Mon. Wea. Rev., 134, 1880–1900.

Morrison H., G. Thompson, and V. Tatarskii, 2009: Impact of Cloud Microphysics on the Development of Trailing Stratiform Precipitation in a Simulated Squall Line: Comparison of One- and Two-Moment Schemes. Mon. Wea. Rev., 137, 991–1007.

Murakami, M., T. Matsuc, H. Mizuno and Y. Yamada, 1994: Mesoscale and microscale structures of snow clouds over the Sea of Japan. Part I: Evolution of microphysical structures in short-lived convective snow clouds. J. Met. Soc. Japan, 72, 671–694.

Murakami, M., Y. Yamada, T. Matsuo, K. Iwanami, J. D. Marwitz and G. Gordon, 2003: The Precipitation Process in Convective Cells Embedded in Deep Snow Bands over the Sea of Japan. J. Met. Soc. Japan, 81, 515-531.

Nielsen, N., 1997: An early-autumn polar low formation over the Norwegian Sea. J. Geophys. Res., 102, 13955–13973.

Nordeng, T. E., 1987: The effect of vertical and slantwise convection on the simulation of polar lows. Tellus, 39A, 354-375.

Nordeng, T. E., 1990: A model-based diagnostic study of the development and maintenance mechanism of two polar lows. Tellus, 42A, 92–108.

Nordeng, T. E., and E. A. Rasmussen, 1992: A most beautiful polar low. A case study of a polar low development in the Bear Island region. Tellus, 44A, 81–99.

Penner, J. E., et al., 2001: Aerosols, their direct and indirect effects, in Climate Change 2001: The Scientific Basis. Contribution of Working Group I to the Third Assessment Report of the Intergovernmental Panel on Climate Change, edited by J. T. Houghton et al., pp. 289–348, Cambridge Univ. Press, New York.

Petty, G. W., 1994: Physical retrievals of over-ocean rain rate from multichannel microwave imagery. Part I: Theoretical characteristics of normalized polarization and scattering indices. Meteorol. Atmos. Phys., 54, 79–100.

Petty, G. W., 1997: An intercomparison of oceanic precipitation frequencies from 10 SSM/I rain rate algorithms and shipboard present-weather reports. J. Geophys. Res., 102, 1757-1777.

Posselt D. J., and J. E. Martin, 2004: The effect of latent heat release on the evolution of a warm occluded thermal structure. Mon. Wea. Rev., 132, 578–599.

Ramanathan, V., et al., 2001:, Aerosols, climate, and the hydrological cycle, Science, 294, 2119– 2124.

Rasmussen E. A., 1979: Polar low as an extratropical CISK disturbance. Quart. J. Roy. Meteor. Soc., 105, 531–549.

Rasmussen E. A., T. S. Pedersen, L. F. Pedersen, and J. Turner, 1992: Polar lows and arctic instability lows in the Bear Island region. Tellus, 44A, 133–154.

Rasmussen E. A. and J. Turner, 2003: Polar lows: Mesoscale Weather Systems in the Polar Regions. Cambridge University Press, 612 pp.

Reisner, J. R., R. M. Rasmussen, and R. T. Bruintjes, 1998: Explicit forecasting of supercooled liquid water in winter storms using the MM5 mesoscale model. Quart. J. Roy. Meteor. Soc., 124, 1071–1107.

Rossby C. G., 1940: Planetary flow patterns in the atmosphere. Quart. J. Roy. Meteor. Soc., 66, 68–87.

Rutledge, S. A., and P. V. Hobbs, 1983: The Mesoscale and Microscale Structure and Organization of Clouds and Precipitation in Midlatitude Cyclones. VIII: A Model for the "Seeder-Feeder" Process in Warm-Frontal Rainbands. J. Atmos. Sci., 40, 1185–1206.

Rutledge, S. A. and P. V. Hobbs, 1984: The mesoscale and microscale structure and organization of clouds and precipitation in midlatitude cyclones. XII: A diagnostic modeling study of precipitation development in narrow cloud-frontal rainbands. J.Atmos. Sci., 20, 2949–2972.

Sardie, J. M., and T. T. Warner, 1983: On the mechanism for the development of polar lows. J. Atmos. Sci., 40, 869–881.

Sardie, J.M. and Warner, T., 1985: A numerical study of the development mechanisms of polar lows, Tellus, 37A, 460-477.

Shapiro, M. A., L. S. Fedor, and T. Hampel, 1987: Research aircraft measurements of a polar low over the Norwegian Sea. Tellus, 39a, 272-306.

Skamarock, W. C., J. B. Klemp, J. Dudhia, D. O. Gill, D. M. Barker, M. G. Duda, X. Y. Huang, W. Wang, and J. G. Powers, 2008: A description of the advanced research WRF version 3. NCAR/TN-468+STR, 126 pp.

Stoelinga, M. T., 1996: A potential vorticity-based study of the role of diabatic heating and friction in a numerically simulated baroclinic cyclone. Mon. Wea. Rev., 124,

849–874.

Sutcliffe, R., 1947: A contribution to the problem of development. Quart. J. Roy. Meteor. Soc., 73, 370–383.

Tao, W.-K., and J. Simpson, 1993: The Goddard cumulus ensemble model. Part I: Model description. Terr. Atmos. Oceanic Sci., 4, 35–72.

Tao, W.-K., J. Simpson, D. Baker, S. Braun, M.-D. Chou, B. Ferrier, D. Johnson, A. Khain, S. Lang, B. Lynn, C.-L. Shie, D. Starr, C.-H. Sui, Y. Wang, and P. Wetzel, 2003: Microphysics, radiation and surface processes in the Goddard Cumulus Ensemble (GCE) model. Meteor. and Atmos. Phys., 82, 97–137.

Tao, W.-K., J. Simpson, and M. McCumber 1989: An ice-water saturation adjustment, Mon.Wea. Rev., 117, 231–235.

Thompson, G., R.M. Rasmussen, and K. Manning, 2004: Explicit Forecasts of Winter Precipitation Using an Improved Bulk Microphysics Scheme. Part I: Description and Sensitivity Analysis. Mon. Wea. Rev., 132, 519–542.

Thompson, G., P.R. Field, R.M. Rasmussen, and W.D. Hall, 2008: Explicit Forecasts of Winter Precipitation Using an Improved Bulk Microphysics Scheme. Part II: Implementation of a New Snow Parameterization. Mon. Wea. Rev., 136, 5095–5115.

Trenberth, K. E., 1978: On the interpretation of the diagnostic quasi-geostrophic omega equation. Mon. Wea. Rev., 106, 131–137.

Twomey, S., 1977: Atmospheric Aerosols, 302 pp., Elsevier Sci., Amsterdam.

Wentz, F. J., and T. Meissner, 2007: Algorithm Theoretical Basis Document: AMSR-E Ocean Algorithms Supplement 1. Santa Rosa, California, USA: Remote Sensing Systems.

Wu, L. T. and G. W. Petty, 2009: Intercomparison of Bulk Microphysics Schemes in Model Simulations of Polar Lows. Submitted to Mon. Wea. Rev.

Yanase, W., G. Fu, H. Niino, and T. Kato, 2004: A Polar Low over the Japan Sea on 21 January 1997. Part II: A Numerical Study. Mon. Wea. Rev., 132, 1552–1574.

Ziegler, C.L., 1985: Retrieval of Thermal and Microphysical Variables in Observed Convective Storms. Part 1: Model Development and Preliminary Testing. J. Atmos. Sci., 42, 1487–1509.